

**Design and fabrication of 3D-extruded scaffolds for  
osteocondral tissue engineering: optimization of  
geometry, curvature, and electroconductivity**

**Pedro Miguel Alves Marcelino**

Thesis to obtain the Master of Science Degree in

**Biological Engineering**

Supervisors: Doctor João Carlos Fernandes da Silva, PhD

Professor Frederico Castelo Alves Ferreira, PhD

**Examination Committee**

Chairperson: Professor Cláudia Alexandra Martins Lobato da Silva, PhD

Supervisor: Doctor João Carlos Fernandes da Silva, PhD

Member of the Committee: Professor Paula Cristina Rodrigues Pascoal Faria, PhD

**December 2021**

## Declaration

I declare that this document is an original work of my own authorship and that it fulfills all the requirements of the Code of Conduct and Good Practices of the Universidade de Lisboa.

# Preface

The work presented in this thesis was performed at the Stem Cell Engineering Research Group (SCERG) at iBB – Institute for Biosciences and Bioengineering of the Instituto Superior Técnico – Universidade de Lisboa (Lisboa, Portugal), during the period February-October 2021, under the supervision of Prof. Frederico Ferreira and Dr. João Carlos Silva.

The results of this work were selected for an oral presentation on the “7th edition of the Symposium on Computational Tools for Direct Digital Manufacturing (CT4DDM)” of the 19<sup>th</sup> International Conference of numerical Analysis and Applied Mathematics (ICNAAM) 2021, which took place virtually on September 24<sup>th</sup>, 2021.





## Acknowledgements

I would first like to express my gratitude to my supervisors, Professor Frederico Ferreira and Doctor João Carlos Silva, for welcoming me as their master's student and giving me the opportunity to develop this work in the fascinating field of tissue engineering. I would like to thank Professor Frederico for all the ideas and insights that contributed to the progress of this project, and to João for the exceptional guidance, kindness, availability, and tirelessness during its execution. A deep gratitude is also due to Doctor Fábio Garrudo, who at times almost became a supervisor, for all the knowledge and dedication showed while teaching some laboratory techniques required for this work, and for all fruitful discussions.

In the past months, I had the opportunity to join a very dedicated and enthusiastic group of people. For their contributions at different stages of this work, I would especially like to thank Doctor Paola Alberte and Doctor Marta Carvalho for their assistance. To everyone in the lab, and to my master's colleagues in particular, I would like to thank for the great environment and for the constructive sharing of ideas. It did make a difference.

In the present work, I came to join an ongoing project of the Stem Cell Engineering and Regenerative Medicine Research Group (SCERG) in cooperation with the Centre for Rapid and Sustainable Product Development (CDRSP) of the Polytechnic Institute of Leiria. For embracing my participation, I would like to thank Professor Nuno Alves and Professor Paula Pascoal Faria, and for their invaluable assistance I would like to thank Doctor Carla Moura and PhD student João Meneses. Part of this work would not have been possible without their contribution.

Recognition is also due to the medical doctor Nuno Ribeiro, for kindly sharing his vast knowledge about the osteochondral tissue and its disorders.

On a more personal level, I would like to thank Pedro and Mário, for showing me a path a few years ago, in more challenging times. To my former colleagues, Diana, Paulo, Joana, Ricardo, Helena, Hélder, Catarina and Sara, for their support and encouragement when I took the decision of conducting this master's thesis work. To my family, who always supported me and believed in this decision. And first and foremost, to Cristina, for the outstanding support, wisdom, patience and caring during the last months. This is dedicated to you.

Finally, I would like to acknowledge the funding received from the FCT, through the projects Stimulli2Scaffolds (PTDC/EME-SIS/32554/2017) and OptiBioScaffold (PTDC/EME-SIS/4446/2020), and through the financing to the Research Unit iBB – Institute for Bioengineering and Biosciences (UIDB/04565/2020 and UIDP/04565/2020) and to the i4HB – Associate Laboratory Institute for Health and Bioeconomy (LA/P/0140/2020). I would also like to thank PARSUK – Portuguese Association of Researchers and Students in the UK for funding through Portugal-UK Bilateral Research Fund (BRF) 2021 Grant.



# Abstract

Osteochondral (OC) tissue is a highly complex tissue comprising articular cartilage (AC) and the underlying subchondral bone. Damage to OC tissue is associated with the risk of developing osteoarthritic degenerative problems due to the limited self-healing capacity of AC. Current therapeutic strategies still fail to generate repaired tissue able to mimic the native OC properties and thus, tissue engineering (TE) has emerged as a promising therapeutic alternative for OC repair. TE is an approach based on cells and engineered biomaterials, in which scaffolds are one essential component. For the manufacture of scaffolds, in recent years, additive manufacturing (AM) techniques have been presenting researchers with added options for a better control over scaffold geometry and for the development of patient tailored designs. In this thesis, fused deposition modeling (FDM), a form of AM, was used to manufacture the different types of scaffolds.

The effect of electrical stimulation (ES) in the development of OC tissue is still poorly understood. Therefore, the development of novel electroconductive scaffolds is critical to address this knowledge gap. In this thesis, methods for coating AM-based poly( $\epsilon$ -caprolactone) (PCL) scaffolds with poly(3,4-ethylenedioxythiophene) doped with poly(styrene sulfonic acid) (PEDOT:PSS) were developed. Good coating stability and conductivities in the range 3.0-26 S/cm were obtained in protocols using (3-glycidyloxypropyl) trimethoxysilane (GOPS) and divinyl sulfone (DVS) as dopants, without significant differences between both.

The optimization of scaffold structure and architecture was performed through parametric design. A new method allowing a faster scaffold design was also developed. Scaffolds with an orthogonal grid-like pattern, layer rotations, varying pore dimensions, and with curved surfaces were developed. Considering the curved scaffolds, a mathematical approach was used to determine a radius of 17.064 mm as the smallest that could be manufactured by FDM with a 2 cm x 2 cm top projected dimension.

Keywords: Osteochondral tissue engineering, PEDOT:PSS, Electroconductive scaffolds, Fused deposition modeling, Curved scaffolds, Mathematical modeling.



## Resumo

O tecido osteocondral (OC) é um tecido altamente complexo constituído pela cartilagem articular (AC) e pelo osso subcondral. Danos no tecido OC estão associados a um risco de desenvolver problemas osteoartríticos degenerativos devido às limitações de regeneração da AC. As estratégias terapêuticas actuais ainda não têm a capacidade de criar um tecido que reproduza as propriedades nativas do tecido OC e, por esse motivo, a engenharia de tecidos (TE) apresenta-se como uma alternativa terapêutica para reparar o tecido OC. A TE é uma abordagem baseada células e em biomateriais, em que os suportes são um componente essencial. Para o fabrico dos suportes, nos últimos anos, as técnicas de manufatura aditiva (AM) têm vindo a fornecer aos investigadores alternativas para um melhor controle da geometria e para o desenvolvimento de estruturas direccionadas para cada paciente. Nesta tese, a modelagem por deposição fundida (FDM), uma variedade de AM, foi usada para fabricar os diferentes tipos de suportes.

O efeito da estimulação elétrica (ES) no desenvolvimento do tecido OC ainda é pouco compreendido e, portanto, o desenvolvimento de novos suportes electrocondutores é fundamental para reduzir essa lacuna no conhecimento. Nesta tese foram desenvolvidos método para revestimento de suportes à base de poli( $\epsilon$ -caprolactona) (PCL) com poli (3,4 etilenodioxitiofeno) dopado com poli(ácido estireno sulfónico) (PEDOT: PSS). Uma boa estabilidade do revestimento e condutividades na faixa de 3,0-26 S/cm foram obtidas usando (3-glicidiloxipropil) trimetoxisilano (GOPS) e divinilsulfona (DVS) como dopantes, sem diferença significativa entre ambos.

A optimização da estrutura e arquitectura de suportes foi realizada através de design paramétrico. Um novo método que permite um desenho de suportes mais rápido foi também desenvolvido. Foram criados suportes com um padrão em grelha ortogonal, com rotações das camadas, com variação das dimensões dos poros e com superfícies curvas. Considerando os suportes curvos, uma abordagem matemática foi usada para determinar um raio de 17,064 mm como o menor que poderia ser fabricado por FDM com uma dimensão, vista do topo, de 2 cm x 2 cm.

Palavras-chave: Engenharia de tecidos osteocondrais, PEDOT:PSS, Suportes electrocondutores, Modelagem por deposição fundida, Suportes curvos, Modelação matemática.



# Table of contents

<b>PREFACE</b> .....	<b>III</b>
<b>ACKNOWLEDGEMENTS</b> .....	<b>V</b>
<b>ABSTRACT</b> .....	<b>VII</b>
<b>RESUMO</b> .....	<b>IX</b>
<b>TABLE OF CONTENTS</b> .....	<b>XI</b>
<b>LIST OF FIGURES</b> .....	<b>XIII</b>
<b>LIST OF TABLES</b> .....	<b>XVIII</b>
<b>ABBREVIATIONS</b> .....	<b>XIX</b>
<b>1. AIM OF STUDIES</b> .....	<b>1</b>
<b>2. INTRODUCTION</b> .....	<b>2</b>
2.1. OSTEOCHONDRAL TISSUE .....	2
2.1.1. <i>Structure overview</i> .....	2
2.1.2. <i>Osteochondral injury and diseases</i> .....	5
2.1.3. <i>Current treatment strategies</i> .....	5
2.2. TISSUE ENGINEERING STRATEGIES FOR THE TREATMENT OF OSTEOCHONDRAL INJURIES .....	6
2.2.1. <i>Scaffolds</i> .....	7
2.2.2. <i>Cells</i> .....	13
2.2.3. <i>Biochemical and physical factors</i> .....	15
Electrical stimuli .....	16
2.3. ELECTRICALLY CONDUCTIVE POLYMERS IN TISSUE ENGINEERING .....	18
2.4. SCAFFOLD FABRICATION TECHNIQUES .....	20
2.4.1. <i>Conventional techniques</i> .....	21
2.4.2. <i>Additive manufacturing techniques</i> .....	23
2.5. COMPUTATIONAL MODELING IN TISSUE ENGINEERING.....	33
<b>3. MATERIALS AND METHODS</b> .....	<b>35</b>
3.1. MODELING SOFTWARE AND MANUFACTURING DEVICE .....	35
3.2. MODEL FABRICATION PROFILES .....	35
3.3. PEDOT:PSS COATED PCL FILMS MANUFACTURING AND CHARACTERIZATION .....	37
3.3.1. <i>PCL films manufacturing</i> .....	37
3.3.2. <i>Coating and crosslinking protocol</i> .....	37
3.3.3. <i>Coating stability assay</i> .....	38
3.3.3.1. Resistance measurement .....	38
3.3.3.2. Electroconductivity measurement: 4-point probe method .....	38
3.3.3.3. Attenuated total reflectance-Fourier-transform infrared (ATR-FTIR) spectroscopy.....	39
3.3.3.4. Contact angle.....	39

3.4.	SCAFFOLD FABRICATION AND CHARACTERIZATION .....	39
3.4.1.	<i>Scaffold manufacturing</i> .....	40
3.4.2.	<i>Coating and crosslinking protocol</i> .....	40
3.4.3.	<i>Compressive mechanical testing</i> .....	40
3.4.4.	<i>Micro-computed tomography analysis</i> .....	41
3.4.5.	<i>Computational simulation of compressive mechanical behavior</i> .....	41
3.5.	STATISTICAL ANALYSIS.....	41
<b>4.</b>	<b>RESULTS AND DISCUSSION .....</b>	<b>42</b>
4.1.	PROCEDURES FOR THE FABRICATION AND CHARACTERIZATION OF ELECTROCONDUCTIVE ORTHOGONAL SCAFFOLDS .....	42
4.1.1.	<i>Orthogonal scaffold design</i> .....	42
4.1.2.	<i>Manufactured electroconductive films and scaffolds</i> .....	43
4.1.3.	<i>Coating characterization</i> .....	44
4.1.4.	<i>PEDOT:PSS-coated PCL scaffold characterization</i> .....	49
4.2.	DESIGNS FOR OSTEOCHONDRAL TISSUE ENGINEERING APPLICATIONS .....	52
4.2.1.	<i>Processes for the quick design of scaffolds</i> .....	52
4.2.1.1.	Layer rotation.....	53
4.2.1.2.	Pore size variation .....	56
4.2.1.3.	Scaffolds with pore gradient along the layers .....	58
4.2.2.	<i>Manufacturing a scaffold mimicking the knee medial condyle surface</i> .....	59
4.2.3.	<i>Design of a double-chamber platform for the study of osteochondral tissue differentiation</i> 61	
4.3.	MATHEMATICAL APPROACH FOR A CURVED SCAFFOLD DESIGN .....	61
4.3.1.	<i>Model development</i> .....	63
4.3.2.	<i>Method to determine maximum curvature of FDM printable scaffolds</i> .....	66
4.3.3.	<i>Manufacturing of curved scaffolds</i> .....	72
4.3.4.	<i>Scaffolds micro-CT characterization</i> .....	73
4.3.5.	<i>Computational simulation of the compressive mechanical behavior of the scaffolds</i> .....	74
4.3.6.	<i>Example applications of curved scaffolds</i> .....	77
<b>5.</b>	<b>CONCLUSIONS AND FUTURE WORK.....</b>	<b>79</b>
	<b>REFERENCES .....</b>	<b>81</b>
	<b>ANNEXES</b>	
A.1.	STABILITY ASSAY ATR-FTIR SPECTRA	
A.2.	PICTURES OF THE MANUFACTURED CURVED SCAFFOLDS	
A.3.	PORE VARIATION SCRIPT FOR FUSION 360	
A.4.	DOUBLE CHAMBER DESIGN	
	TECHNICAL DRAWING	



## List of Figures

Figure 2.1 – Schematic representation of osteochondral tissue composition and organization.....	2
Figure 2.2 – Components of the articular cartilage extracellular matrix.....	3
Figure 2.3 – Repair strategies for chondral and osteochondral defects. ....	6
Figure 2.4 – Structure of poly( $\epsilon$ -caprolactone) (PCL).....	10
Figure 2.5 – Evolution of explored strategies for scaffold construction for osteochondral tissue engineering.....	10
Figure 2.6 – Basic forms of gradients in biological materials. Gradients are fundamentally associated with the changes in chemical compositions/constituents, and structural characteristics like arrangement, distribution, dimension and orientation.....	11
Figure 2.7 – Illustration of the relationship between pore morphology and interconnectivity. ....	12
Figure 2.8 – Stem cell-based strategies for bone and cartilage tissue engineering. ....	14
Figure 2.9 – Overview of cellular mechanisms and functions activated by electrical stimulation.....	17
Figure 2.10 – Chemical structure of commonly explored conducting polymers for biomedical applications: polypyrrole (PPy), polythiophene (PT), poly(3,4-ethylenedioxythiophene) (PEDOT), and polyaniline (PANI).....	19
Figure 2.11 – Chemical structure of PEDOT:PSS and cross-linkers GOPS and DVS used to increase its mechanical stability.....	19
Figure 2.12 – Schematic representation of commonly used techniques for scaffold production: a) Solvent casting/particle leaching; b) Freeze drying or lyophilization; c) Gas foaming; d) Phase separation; e) Electrospinning.....	21
Figure 2.13 – Historical overview of important landmarks and introduction of new technologies for additive manufacturing (AM) techniques in tissue engineering.....	24
Figure 2.14 –Schematic representation of the most commonly AM techniques employed in TE: a) Stereolithography (SLA); b) Selective laser sintering (SLS); c) 3D printing (3DP); d) Fused deposition modeling (FDM).....	25
Figure 2.15 – Schematic illustration of different types of extrusion: a) Filament-fed extruder; b) Screw extruder; c) Syringe extruders with either a mechanically driven plunger or pneumatic pressure plunger. ....	29
Figure 2.16 – Printing strategies with different filament positions and orientations: a) Changing filament orientation; b) Offsetting layers with the same orientation. ....	30
Figure 2.17 – Illustration of 3D bioprinting technologies based on the mechanism used to assist the deposition of the bioinks and its main components.....	31
Figure 3.1 – Start G-code of the printer profile created to allow printing at low temperatures with PCL filament. ....	36
Figure 3.2 – Detail of the sliced first layer of the 3D printed films. To increase the smoothness of this layer, the following parameters were changed in relation to the default profile: 0.15 mm extrusion width; 2 perimeters; 100 % infill/perimeter overlap; 1.2 extrusion multiplier.....	37

Figure 4.1 – Steps in the design of orthogonal scaffolds in Fusion 360: a) Sketch of an S shaped path along the x-axis; b) Creation of a scaffold fiber along that path; c) Repetition of sketch and fiber creation along the y-axis, on top of the previous fiber; d) Copy of the previous two scaffold fibers along the z-axis. .... 42

Figure 4.2 – Representative images of manufactured PCL films and scaffolds before and after coating with PEDOT:PSS dispersions: a) 2 mm × 1 mm × 0.5 mm films (left), and coated with PEDOT:PSS(GOPS) (right); b) 10.5 mm × 10.5 mm × 3 mm scaffolds (left), and coated with PEDOT:PSS(GOPS) (right). .... 43

Figure 4.3 – Measured resistance with a multimeter, over 7 days, on the surface of coated PCL films submerged in PBS and at 37°C. PCL films and alkaline treated PCL films (PCL(NaOH)) coated with PEDOT:PSS are not represented because the measured resistances were above the detection limit of the multimeter. Results are expressed as mean ± SD (n=4). (Resistance log scale). .... 44

Figure 4.4 – Calculated conductivity, with the four-point probe method, on the surface of coated PCL films. Results are expressed as mean ± SD (n=3). (Electroconductivity log scale). .... 45

Figure 4.5 – Calculated conductivity with the four-point probe method for the coating stability assay. Conductivity was measured on coated PCL films submerged in PBS at 37°C and 5% CO<sub>2</sub>. Films were collected to be analyzed on the days 0, 1, 7, 14, and 21 of the stability assay. Results are expressed as mean ± SD (n=3). (Electroconductivity log scale). .... 46

Figure 4.6 – ATR-FTIR spectra of samples of uncoated PCL films, samples of coating dispersions, and samples of coated PCL films collected at the day 0 of the stability assay. .... 47

Figure 4.7 – Representative pictures of water droplet contact angles on PCL films: a) Pristine PCL; b) PCL(NaOH); c) PCL coated with PEDOT:PSS(GOPS); d) PCL coated with PEDOT:PSS(DVS); e) PCL(NaOH) coated with PEDOT:PSS(GOPS); f) PCL(NaOH) coated with PEDOT:PSS(DVS). The corresponding angles are shown below each photograph. .... 48

Figure 4.8 – Contact angle on the surface of uncoated and coated PCL films determined by the sessile drop method. Coated films were collected to be analyzed on day 0 of the stability assay. Results are expressed as mean ± SD (n=7). .... 48

Figure 4.9 – Representative compressive stress-strain curves of uncoated and PEDOT:PSS-coated PCL scaffolds. .... 49

Figure 4.10 – Representative picture of the collapse of the coated PCL films during compressive mechanical testing. The collapse occurred in all samples with coating (PCL+PEDOT:PSS(GOPS) and PCL+PEDOT:PSS(DVS)) and did not occur in the uncoated control samples (PCL and PCL(NaOH)). .... 50

Figure 4.11 – Compressive Young's modulus of uncoated and PEDOT:PSS-coated PCL scaffolds. Results are expressed as mean ± SD (n=5). .... 50

Figure 4.12 Estimated maximum stresses of uncoated and coated PCL scaffolds. Results are expressed as mean ± SD (n=5). .... 51

Figure 4.13 – Micro-CT imaging reconstructions: a) Representative pictures of coronal, transverse, and sagittal cuts of a PCL scaffold (PCL+PEDOT:PSS(GOPS) scaffold in the picture); b) Representative 3D

reconstruction, (with a cut section) of a PCL scaffold (PCL(NaOH)+PEDOT:PSS(DVS) scaffold in the picture).....	51
Figure 4.14 –Pore and fiber dimensions of uncoated and PEDOT:PSS-coated PCL scaffolds, estimated from measurements in transverse cuts obtained from micro-CT imaging. Results are expressed as mean $\pm$ SD (n=3). .....	52
Figure 4.15 – Steps to create the S shaped fiber paths with 0-90° orientation: a) Quadrilateral delimiting final scaffold size. Short vertical line is the reference for layer rotations; b) S shaped path rotated 0° in relation to the reference line; c) S shaped path rotated 90° in relation to the reference line. ....	54
Figure 4.16 – S shaped fiber paths for non-orthogonal scaffolds: a) Path for 30° rotations; b) Path for 45° rotations; c) Path for 60° rotations. ....	54
Figure 4.17 – Steps in the creation of a scaffold with 0-90° oriented fibers: a) 0° scaffold fiber; b) 90° scaffold fiber designed above the previous fiber; c) Scaffold model created by stacking copies of this fiber pair; d) Picture of FDM manufactured PCL scaffold.....	55
Figure 4.18 – Steps in the creation of a non-orthogonal scaffold (example with 0-30° oriented fibers): 0° scaffold fiber; b) 30° scaffold fiber designed above the previous fiber; c) Scaffold model created by stacking copies and rotations of copies of the previous two fibers. ....	55
Figure 4.19 – Models and manufactured scaffolds with non-orthogonally oriented fibers: a) Model with 0-30° oriented fibers; b) Model with 0-45° oriented fibers; c) Model with 0-60° oriented fibers; d) ) Picture of FDM manufactured PCL scaffolds with layer rotation of, from left to right, 0-30°, 0-45°, and 0-60°. ..	56
Figure 4.20 – Steps in the creation and manufacture of a scaffold with pore size variation: a) Paths of the first two layers of the scaffold; b) Creation of the scaffold fibers along those paths; c) Scaffold model created by stacking copies of this fiber pair; d) Scaffold model top view; e) Picture of FDM manufactured PCL scaffold with pore size variation. ....	57
Figure 4.21 – Model and manufactured scaffold with pore gradient along the layers: a) Scaffold model top view; b) Scaffold cross-section; c) Picture of FDM manufactured PCL scaffold with pore gradient along the layers. ....	58
Figure 4.22 – Section of the femur medial condyle to be mimicked by a scaffold a) 20 mm x 14 mm section of interest to be replicated; b) Close-up view of the section. ....	59
Figure 4.23 – Steps in the reconstruction of a section of a femur medial condyle to be manufactured by FDM: a) Representative layer cut with traced fiber path; b) Scaffold fiber created following the previous path; c-e) Designed scaffolds, replicating the process shown in a-b) for the entire section of the medial condyle, with fibers in successive layers perpendicular to each other. The connections between parallel segments in each layer: c) follow the cut in a); d) are straight segments; e) are not connected. ....	60
Figure 4.24 – FDM manufactured PCL scaffold mimicking a section of the femur medial condyle, corresponding to the model in Figure 4.23 e): a) Printed scaffold; b) Close-up view; c) Scaffold fitting the cut in the medial condyle and following the native curvature of the tissue. ....	60
Figure 4.25 – Experimental curved surface scaffold with an arbitrary curvature: a) Profile of the curved surfaces of the scaffold, with two axis of symmetry; b) Top and bottom views of the modeled scaffold. ....	62

Figure 4.26 – Pictures of an experimental curved scaffold, with arbitrary curvature, manufactured by FDM using conductive PLA filament: a) Top view; b) Bottom view. White arrow points to the height of separated filaments. .... 63

Figure 4.27 –Contour intended for the surface of curved scaffolds, represented by the bright area. The curvature is defined by the sphere radius. Projected square shape has a 20.1 mm side. .... 64

Figure 4.28 – Illustration of the steps in the design of a curved scaffold in Fusion 360, with constant radii surfaces tracing the path of curved fibers of the scaffold. .... 65

Figure 4.29 – Illustration of the steps in the design of a curved scaffold in Fusion 360, with concentric radii surfaces tracing the path of curved fibers of the scaffold. .... 65

Figure 4.30 – Design objective to determine the maximum curvature of an FDM printed scaffold. a) Cross-section, through the middle of the scaffold, observing decreased layer support closer to the base of the print; b) Minimum contact between adjacent layers when maximum curvature is reached. .... 66

Figure 4.31 – a) Wide view and b) Close-up of the base of the scaffold where the extreme minimum contact situation will occur. The light blue structures represent the first fibers being printed, on top of the printer bed. Since the scaffold is symmetric, only the bottom half is represented. R – radius of circular cross-section; L – vertical distance to the axis of symmetry of the scaffold (grey dashed line);  $\alpha$ ,  $\beta$  – angles measured from the axis of symmetry of the scaffold (grey dashed line). .... 67

Figure 4.32 – Calculation of the sphere radius (17.064 mm) defining scaffold surface curvature from the radius calculated to provide minimum support between scaffold fibers (13.7902 mm). .... 69

Figure 4.33 – Designed curved scaffolds with concentric radius surfaces. .... 70

Figure 4.34 – Designed curved scaffolds with constant radius surfaces. .... 71

Figure 4.35 – Representative pictures of imperfections in the curved scaffolds manufactured by FDM: a) pore occlusions seen in all curved scaffolds; b) detached fibers seen in scaffolds with radius of 14 mm and 12 mm; c) stringing, more noticeable in scaffolds of radius 17.064 mm and smaller. .... 73

Figure 4.36 – Curved scaffolds micro-CT imaging reconstructions. Scaffolds designed with concentric radius strategy. .... 74

Figure 4.37 – Curved scaffolds micro-CT imaging reconstructions. Scaffolds designed with constant radius strategy. .... 74

Figure 4.38 – Regions of interest for finite element analysis of the mechanical behavior in an illustrative curved scaffold: a) Concentric, 20 mm radius scaffold (light) and regions of interest (dark); b) Section through the center; c) Section on the corner; d) Slice next to the vertical axis of symmetry. .... 75

Figure 4.39 – Finite element analysis on the regions of interest from Figure 4.38, simulating the mechanical behavior to regions of interest of a PLA scaffold when 1 MPa load is applied on the front surface and the back is considered fixed: a) Side, front, and top views of the von Mises stress; b) Both sides, front, and top views of the von Mises stress; c) Side, front and opposite side views of the von Mises stress; d) Predicted displacement due to the applied load. (Scale bars truncated below the maximum to provide a better sense of the simulated behavior)..... 76

Figure 4.40 – Radius of spheres approximating the curvatures of osteochondral surfaces in a human femur..... 78

Figure 4.41 – Examples of patient-tailored curved structures produced by additive manufacturing: a) 3D bioprints of human ear and sheep meniscus; b) FDM prints of a breast; c) FDM print of rabbit proximal humeral joint. .... 78

Figure A.1 – ATR-FTIR spectra of samples of PCL and PCL(NaOH) films coated with PEDOT:PSS(GOPS) collected to be analyzed on days 0, 1, 7, 14, and 21 of the stability assay.

Figure A.2 – ATR-FTIR spectra of samples of PCL and PCL(NaOH) films coated with PEDOT:PSS(DVS) collected to be analyzed on days 0, 1, 7, 14, and 21 of the stability assay.

Figure A.3 – Top of FDM manufactured curved scaffolds with concentric radius surfaces.

Figure A.4 – Top of FDM manufactured curved scaffolds with constant radius surfaces.

Figure A.5 – Bottom of FDM manufactured curved scaffolds with concentric radius surfaces.

Figure A.6 – Bottom of FDM manufactured curved scaffolds with constant radius surfaces.

Figure A.7 – Two chamber vessel for promotion of chondrogenic and osteogenic differentiation on the opposing sides of a scaffold: a) See-through view; b) Slanted cross-section.

Figure A.8 – Evaluation of performance of the two chamber vessel: a) With water in only one chamber at room temperature, no leaks were observed until all water evaporated; b) With DMEM in only one chamber in an incubator at 37°, the fluid leaked and started permeating through the printed material layers.

## List of Tables

Table 2.1 – Overview of commonly used scaffold materials for osteochondral tissue engineering. ....	8
Table 2.2 – Morphologic parameters for porous scaffold characterization. ....	12
Table 2.3 – Comparison of common 3D bioprinting strategies. ....	33
Table 4.1 – Parameters chosen to determine the size and geometry of orthogonal scaffolds. ....	43
Table 4.2 – Parameters chosen to determine the size and geometry of scaffolds with layer rotations. ....	53
Table 4.3 – Parameters chosen to determine the size and geometry of scaffolds with pore size variation. ....	57
Table 4.4 – Solution to Equations in 4.1 that describe mathematically the problem formulated in Figure 4.31, calculating the most extreme curvature for a scaffold to be manufactured by FDM. ....	68
Table 4.5 – Summary of deducted curved scaffold dimensions that provide minimum support between scaffold fibers. ....	69
Table 4.6 – Assumptions in the deduction of curved scaffold dimensions that provide minimum support between scaffold fibers. ....	70
Table 4.7 – Pore size variation in the top layer of the 20 mm radius scaffolds created with the concentric and constant radius strategies. ....	72
Table 4.8 – Projected pore area at the center and edge of top and middle layers of the 20 mm radius scaffolds created with the concentric and constant radius strategies. ....	72

# Abbreviations

ABS – Acrylonitrile Butadiene Styrene  
AC – Articular Cartilage  
ASA – Acrylonitrile Styrene Acrylate  
ACI – Autologous Chondrocyte Implantation  
ADSC – Adipose-Derived Stem Cell  
AM – Additive Manufacturing  
ATR-FTIR – Attenuated Total Reflectance-Fourier-Transform Infrared  
BG – Bioactive Glass  
BMP – Bone Morphogenetic Protein  
BMSC – Bone Marrow-Derived MSC  
CAD – Computer Aided Design  
CP – Conductive Polymer  
CS – Chondroitin Sulfate  
CT – Computer Tomography  
DBSA – Dodecylbenzenesulfonic Acid  
DMEM – Dulbecco's Modified Eagle Medium  
DVS – Divinyl Sulfone  
ECM – Extracellular Matrix  
EG – Ethylene Glycol  
ES – Electrical Stimulation  
ESC – Embryonic Stem Cell  
FDM – Fused Deposition Modeling  
FFF – Fused Filament Fabrication  
FGF – Fibroblast Growth Factor  
FRESH - Freeform Reversible Embedding of Suspended Hydrogels  
GAG – Glycosaminoglycan  
GelMA – Gelatin Methacrylate  
GOPS – (3-glycidyloxypropyl) trimethoxysilane  
HA – Hyaluronic Acid  
HAp – Hydroxyapatite  
HIF-1 – Hypoxia-Inducible Factor 1  
iPSC – induced Pluripotent Stem Cell  
MACI – Matrix Assisted Chondrocyte Implantation  
Micro-CT – Micro-Computed Tomography  
MRI – Magnetic Resonance Imaging  
MSC – Mesenchymal Stem/Stromal Cell  
OC - Osteochondral  
PANI – Polyaniline

PBS – Phosphate-buffered saline  
PCL – Poly( $\epsilon$ -caprolactone)  
PDLLA – poly(D,L-lactide)  
PDMS – Poly(dimethylsiloxane)  
PEDOT:PSS – Poly(3,4 ethylenedioxythiophene) doped with Poly(styrene sulfonic acid)  
PEEK – Polyetheretherketone  
PEG – Poly(ethylene glycol)  
PEGDMA – Poly(ethylene glycol) dimethacrylate  
PEO – Poly(ethylene oxide)  
PHBV – Poly(hydroxybutyrate-co-hydroxyvalerate)  
PLA – Poly(lactic acid)  
PLGA – Poly(lactic acid-co-glycolic acid)  
PLLA – Poly(L-lactic acid)  
PNIPAAm – Poly(N-isopropyl acrylamide)  
PPF – Poly(propylene fumarate)  
PPy – Polypyrrole  
PT – Polythiophene  
PVA – Poly(vinyl alcohol)  
SEM – Scanning Electron Microscopy  
SMSC – Synovium-Derived MSC  
TCP – Tricalcium Phosphate  
TE – Tissue Engineering  
TGF- $\beta$  – Transforming Growth Factor- $\beta$   
TIPS – Thermally induced Phase Separation  
TMC – Trimethylene carbonate  
UV – Ultraviolet  
VEGF – Vascular Endothelial Growth Factor



# 1. Aim of studies

Defects in the OC tissue are a cause of joint malfunction and can lead to the development of degenerative diseases such as osteoarthritis. An estimate by the World Health Organization has determined that 9.6% of men and 18.0% of women over the age of sixty suffer from symptomatic osteoarthritis, and among them 80% have limitations in mobility and 25% are unable to perform major daily activities<sup>1</sup>. Due to the poor repair capabilities of AC, OC defects tend to aggravate with time, and clinical findings have shown that currently no existing medication can substantially promote the healing process.

Current treatment options for OC defects depend on the size and severity of the injury, however they fail to fully recapitulate native tissue properties and structure, compromising long-term clinical results. TE is regarded as a promising approach for OC tissue regeneration as it might be able to overcome the limitations associated with current therapies. TE goal is to regenerate or replace damaged tissue through an ideal combination of cells, support biomaterial scaffolds, chemical factors and dynamic mechanical signals.

Therefore, scaffolds are of major importance in TE, providing cells with an adequate structure to grow, differentiate and secrete new tissue. However, to this date, TE methods targeting OC defects with engineered scaffolds have not been fully successful, with structural and functional differences between the engineered tissues and native OC tissue still persisting.

The aim of this work is the development of new scaffold structures and materials for OC TE. Concerning the scaffold materials, novel electroconductive coatings for PCL scaffolds, based on PEDOT:PSS, are proposed and characterized. Regarding the scaffold structure, two main strategies are outlined. In the first, methods are proposed for the quick design and manufacture of 3D printed scaffolds, specifying the variation in pore geometry. In the second, the design and manufacture of two types of curved scaffolds is described. The first type concerns curved scaffolds mimicking the native curvature of OC tissue, propounding the creation of constructs for personalized therapies. The second type concerns scaffolds with a fully defined curvature and the computational determination of its mechanical properties.

## 2. Introduction

### 2.1. Osteochondral tissue

#### 2.1.1. Structure overview

The osteochondral (OC) tissue is a highly organized and complex structure located at the end of long bones, consisting of cartilage, calcified cartilage and subchondral bone<sup>2,3</sup>. Despite bone and cartilage presenting distinctive characteristics from the macroscale to the nanoscale, the tissue connecting them shows a gradual variation in terms of structural, mechanical, physicochemical, and biological properties. The existence of this fine interplay between OC components, makes them tightly interconnected under physiological conditions<sup>3</sup>. Figure 2.1 shows a schematic representation of OC tissue gradient features.

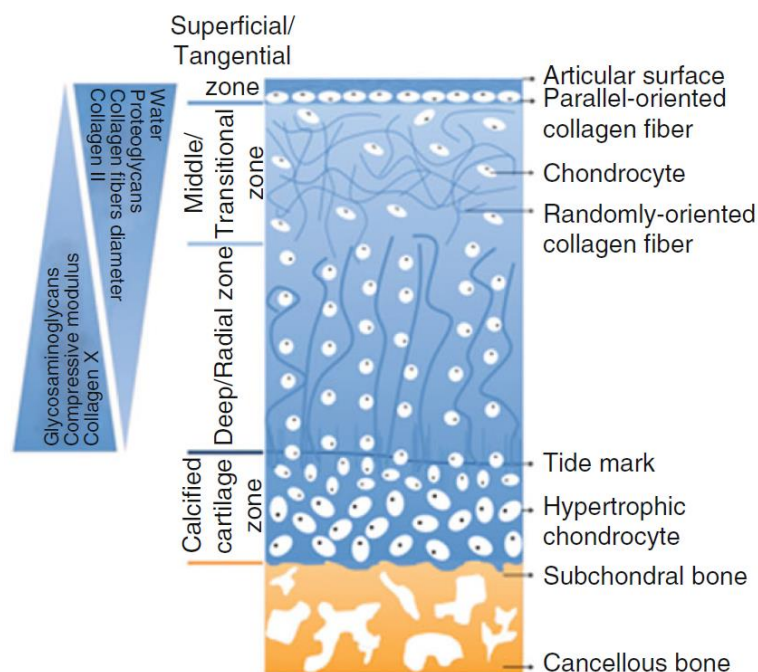


Figure 2.1 – Schematic representation of osteochondral tissue composition and organization (adapted from <sup>4</sup>).

Depending on its composition, particularly in regard to its fibers, cartilage in the human body can be classified into three main types, hyaline cartilage, elastic cartilage and fibrocartilage<sup>5</sup>. Fibrocartilage is found in intervertebral discs, tendon attachments to bones and in the junctions between the flat bones of the pelvis. Elastic cartilage is located in the auricle of the ear, the walls of the external auditory canal and eustachian tubes and in the epiglottis of the larynx. Hyaline cartilage is the most common type in the human body, being located on the surface of synovial joints and in the respiratory passages, acting as a support tissue. It also forms the growing plate in long bones in childhood<sup>6</sup>. The hyaline cartilage in the synovial joints, designated articular cartilage (AC), is the one relevant for this work.

As a tough, durable and flexible form of the supporting connective tissue, AC plays supportive and protective roles in the musculoskeletal system<sup>5</sup>. It is composed by a dense extracellular matrix (ECM)

and chondrocytes, the only resident cell type, and it is devoid of neural, vascular and lymphatic structures<sup>5</sup>. It provides a smooth, lubricated, low-friction surface, cushioning the articulation between adjacent bones and transmitting the load and shear forces to the underlying subchondral structures<sup>7</sup>. The synovial fluid, in contact with the cartilage surface also plays a role in the tissue biomechanical behavior. It contributes to the lubrication but also to the nutrition, being the major source of nutrients to the avascular cartilage<sup>7</sup>.

Visually, AC has a white, glassy appearance, and a thickness between 2 and 4 mm, depending on the location<sup>7,8</sup>. Chondrocytes are the specialized cells responsible for the synthesis, organization and homeostasis of all the ECM components and are sparsely spread within the matrix, making up between 1-5 % of the tissue volume<sup>9</sup>. Regarding the ECM, it consists mainly of water (65-80 % of the total wet weight, the fluid phase), with higher concentration in the superficial zone and decreasing towards the deep zones<sup>8,9</sup>. In the solid phase collagen is the main component (60-86 % dry weight)<sup>5</sup>. Type II collagen is the predominant (90-95 %), although some other types like IV, IX, X and XI are also present<sup>9</sup>, with distinct roles strengthening the fiber network<sup>8</sup>. These collagen molecules form fibrils that interweave and form a mesh, that provide tensile strength and physically entrap other macromolecules<sup>10</sup>. Proteoglycans are another major component of the AC ECM. Proteoglycans are composed by a protein core to which glycosaminoglycans (GAGs), long repetitive negatively charged carbohydrates with a repeating disaccharide unit, are covalently attached<sup>8</sup>. The most prevalent proteoglycan in AC is aggrecan, in which chondroitin sulphate and keratin sulphate are the main components. The high density of negative charges of the sulfated glycosaminoglycan chains of proteoglycans is responsible for attracting cations and facilitating interaction with water, resulting in high osmotic pressure, influencing the compressive behavior of cartilage<sup>11</sup>. Linked to GAGs via proteoglycan link proteins and thus creating an intricate structure, hyaluronic acid (HA) is another highly important GAG to the structure and function of AC<sup>5,8-10</sup>. Due to its viscoelastic behavior and moisture retention capacity, it provides the cartilage lubricant and shock absorbing capabilities<sup>12</sup>. A schematic representation of ECM structure and composition is shown in Figure 2.2.

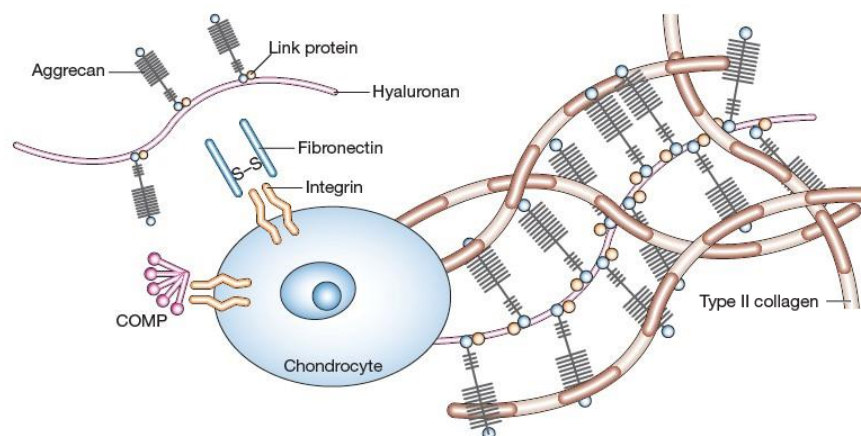


Figure 2.2 – Components of the articular cartilage extracellular matrix (adapted from <sup>11</sup>).

With a distinct variation along its perpendicular direction, in terms of structure and composition of the ECM matrix as well as chondrocyte morphology, four distinct zones can be identified in AC<sup>13</sup>. At the

top, farthest from the bone, the superficial/tangential zone is the thinnest, making up 10-20 % of its height<sup>5</sup>. An acellular sheet predominantly composed of collagen fibers covers the joint<sup>10</sup>. Below, there is a layer of flattened chondrocytes, with the long axis parallel to the surface. They synthesize more collagen and less proteoglycans relative to other zones and the water and fibronectin amounts are also higher. The fibrils are tightly packed and parallel to the surface. This combination imparts the greatest tensile and shear strength to this zone<sup>10</sup>. Immediately beneath is the middle/transitional zone, making up around 50 % of AC height<sup>8</sup>. Here, the collagen fibrils are thicker and randomly oriented, and the chondrocytes are rounder. There is more proteoglycan and less collagen and water than in the previous zone<sup>10</sup>. Below, the deep/radial zone makes up around 35 % of the AC height<sup>8</sup>. The collagen fibrils have the largest diameter and are bunched up oriented perpendicular to the surface. It has the higher proteoglycan and the lower water contents. Chondrocytes are spheroid in shape and stacked in columns perpendicular to the surface. The variation in composition gives this zone a higher compressive resistance<sup>5</sup>. The calcified cartilage layer is a thin layer below the deep zone, where the ECM contains a high concentration of calcium salts, and is located directly above the subchondral bone<sup>14</sup>. A thin wavy border, known as tidemark, which can be seen histologically due to its affinity for basic dyes, marks the border between the deep zone and the calcified cartilage<sup>9</sup>. Collagen fibers run continuously between these two zones, strengthening this connection. The calcified cartilage anchors the cartilaginous zone to the subchondral bone, serving as a transitional buffer to compensate the discontinuity of stiffness between cartilage and bone<sup>8</sup>. Chondrocytes in this zone express a hypertrophic phenotype and produce a network rich in type X collagen<sup>15</sup>. This layer, being permeable to small nutritional solutes of low molecular weight, plays an important role maintaining the distinct microenvironments of cartilage and bone<sup>5</sup>.

Subchondral bone does not belong to AC but, together, both form what is designated as an OC unit. A separation named cement line is identifiable between them. Unlike the tidemark, it has no continuous collagen fibers running through it, connecting the two regions, resulting in a region of relative weakness<sup>16</sup>. The connection is strengthened by the irregular surface of the subchondral bone connecting to the calcified cartilage, which also allows the transmission of mechanical loads to the bone<sup>5,16</sup>. Anatomically, the subchondral bone can be separated into the subchondral bone plate and the subchondral cancellous (or trabecular) bone. The former is a thin layer that lies below the calcified cartilage and has low porosity, limited blood supply and greater resistance. The latter is more porous, has randomly aligned supporting trabeculae, is highly vascularized and metabolically more active<sup>5</sup>. The main cell types responsible for its activity are osteoblasts (bone ECM formation), osteocytes (bone homeostasis), and osteoclasts (bone resorption)<sup>17</sup>. The bone matrix is composed by a mineral part (65-70 %) constituted mostly by hydroxyapatite (HAp) and an organic part (25-30 %), mainly of type I collagen, but also with proteoglycans, glycoproteins and sialoproteins<sup>17</sup>. The complex hierarchical association between the mineral and organic parts is ultimately responsible for the hardness and resistance of the bone tissue<sup>5</sup>.

### 2.1.2. Osteochondral injury and diseases

OC defects are defined as lesions disrupting both the integrity of AC and subchondral bone. Depending on the depth of the defect they can be given three distinct classifications. In partial thickness chondral defect, the damage is confined to the hyaline cartilage, without affecting the calcified cartilage. In full thickness chondral defect, the whole AC is affected, exposing the underlying subchondral bone, but not affecting it. In an OC defect the damage penetrates the subchondral bone<sup>5,7,10,18</sup>.

Having two tissues, AC and the subchondral bone, with very distinct intrinsic healing capacities creates an additional challenge to treat OC defects<sup>18</sup>. In a typical tissue, the response to injury usually follows the cascade of necrosis, inflammation, repair and remodelling<sup>9</sup>. The avascular nature of AC prevents the unfolding of this cascade, which seems to be the main reason for the extremely low self-repair capacity. In the event of an injury, there is a limited proliferation of chondrocytes and there is migration of a small number of synovial fibroblasts and other cells towards the injury, to fill it and produce new matrix<sup>19</sup>. However, this new matrix will be morphologically and mechanically inferior to the native tissue<sup>7</sup>. When the injury penetrates the subchondral bone, the defect is filled with a fibrin clot and the classic wound healing response ensues, with a large number of stem cells migrating to the injury site. However, these cells are unable to reconstitute tissue resembling the original hyaline cartilage, producing a fibrocartilaginous tissue mostly composed by type I collagen. The formed tissue is mechanically suboptimal and unable of durable structural bonding with the uninjured surrounding cartilage<sup>19</sup>. In any case, tissues will tend to further degenerate, progressing towards osteoarthritis. Consequently, treatment strategies will have to address both the subchondral bone and AC, to fully restore OC tissue structural integrity and function<sup>13,20</sup>.

### 2.1.3. Current treatment strategies

Considering the level of repair that clinical treatments provide to chondral or OC lesion sites, they can be classified into palliative treatments, reparative treatments, and regenerative/restorative treatments<sup>21</sup>.

The first group includes treatments like arthroscopic lavage, debridement, and chondroplasty. These treatments are used to remove damaged or loose tissue and to smooth the edges of cartilage and are considered the least invasive. As suggested by the name, they seek to alleviate symptoms like articular pain, although the removed injured tissue usually is not replaced<sup>5,19,21</sup>.

Reparative treatments include procedures like microfracture and the use of autografts and allografts. In microfracture (Figure 2.3a) the aim is to repair the defect area by puncturing the bone and inducing bleeding, promoting the formation of a blood clot, and leading ultimately to the formation of fibrocartilage tissue. However, the repaired tissue being richer in type I collagen is of inferior quality relatively to the native tissue, and despite a short-term improvement has a faster wear compromising long-term results<sup>5,21-23</sup>. Considering autografts (Figure 2.3b), cartilage-bone plugs are harvested from regions of the distal femur that bear low loads. Constrained to small defects due to limited graft availability, it allows a faster rehabilitation since these grafts can bear loads in the early post-operative period. Considering the allogenic approach (Figure 2.3c), it takes advantage of the immune privileged avascular nature of cartilage, though not without immunogenicity risks. There are no donor site

limitations, although there is a limitation in the availability of allograft tissue as well as difficulties matching donor site shape and the mechanical properties to the native tissue<sup>23</sup>.

The objective of regenerative treatments is to restore defective OC tissues. Considered a regenerative treatment, autologous chondrocyte implantation (ACI) has seen many improvements since its introduction more than 30 years ago. In this procedure, healthy autologous chondrocytes are isolated from a cartilage biopsy and then expanded in laboratory, followed by seeding in the affected area, protected by a membrane covering the treated defect<sup>5,19,21</sup>. In an improvement of the ACI method, designated matrix-assisted chondrocyte implantation (MACI) (Figure 2.3d), isolated autologous chondrocytes are combined with a synthetic matrix prior to expansion and implantation. In general, the limitations of ACI and MACI include the need for two surgeries and long recovery time, slow tissue maturation and the possibility of dedifferentiation of chondrocytes during the expansion, leading to fibrous tissue formation<sup>5,21,24,25</sup>.

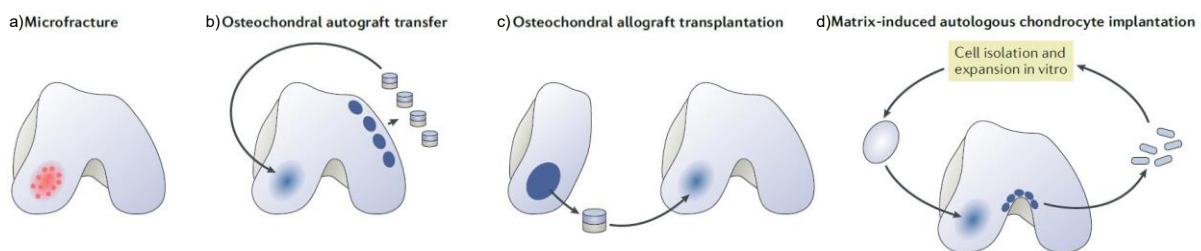


Figure 2.3 – Repair strategies for chondral and osteochondral defects (adapted from <sup>23</sup>).

Despite continuous progress in the last several years, few treatments have translated to medical products, with many struggling to get approval in the clinical trials by the regulatory agencies<sup>5</sup>. Comparing the number of available treatments, there are more options focusing solely on chondral defects in relation to treatments focusing on the OC unit. Among these available treatment options, cell-based therapies and tissue engineering (TE) products are contemplated.

In a review by Wei and Dai<sup>5</sup>, the products BioCartilage®, DeNovo®, Cartiform®, Chondrofix®, CarGel™, TruFit™, MaioRegen™, ChondroMimetic® and Agili-C™ are identified as commercial products already available for cartilage and OC repair. In the review, the authors provide information about the composition, applications, and clinical trials where these products were studied. Considering products only for cartilage repair, the review by Huang et.al.<sup>22</sup> presents a list of only tissue engineered products, describing the size, composition and implantation procedure (Biocart™II, Bioseed®-C, Cartipatch®, Chondrosphere®, Hyalograft® C, MACI, NeoCart®, NOVOCART® 3D, RevaFlex™, CaReS®, INSTRUCT). In another review by Kwon et.al.<sup>23</sup>, a longer list of products under development and their promising results in clinical trials is presented.

## 2.2. Tissue engineering strategies for the treatment of osteochondral injuries

Despite some latest progress, conventional techniques continue presenting several limitations, being unable to achieve functional OC regeneration. The emergence of TE has opened new horizons for the establishment of new treatments, combining the principles of engineering and life sciences towards the development of biological substitutes to restore, maintain or improve tissue function<sup>17,21,26</sup>.

In TE strategies three key components have been proposed, scaffolds, cells and the signaling (biochemical and biophysical) factors<sup>5,27</sup>, which will be discussed in the following subsections.

### 2.2.1. Scaffolds

In general terms, an ideal scaffold should emulate structurally and functionally the native OC tissue. Not intended, by design, to be a permanent structure, they should be biodegradable and provide the appropriate microenvironment to promote cell differentiation and ECM production<sup>5,28</sup>. Several requirements from different perspectives should be considered, which can be grouped in terms of composition, structure, functionality, and preparation<sup>5</sup>:

- Composition: the scaffold should be biocompatible to prevent immune rejection and minimize inflammation. It should also have stable physicochemical properties when implanted in the body. Considering biodegradability, when conducted by host enzymatic or biological processes, it should not generate toxic byproducts. The degradation rate should match to the rate of tissue growth, so that sufficient support could be maintained. It should also allow invasion by host cells, to produce new ECM<sup>5,28-30</sup>.

- Structure: the scaffold should possess a stratified construction, with adequate variation between layers. It should present interconnected pores, with pore size and porosity tailored to the target tissue and cells, to allow cell migration and diffusion of nutrients and waste. It should also provide a large surface area for cells to grow and migrate. In case of vascularized tissues (e.g., bone), it should allow the invasion of vasculature or have inbuilt vascular channels. The pore structure should not weaken the mechanical properties<sup>5,28,29</sup>.

- Functionality: the scaffold should have the ability to interact with host cells, to maintain morphological and phenotypical characteristics, and also allow the inclusion of biological cues and growth factors to promote cell attachment, proliferation or differentiation. Its biomechanical properties, such as compressive strength, tensile strength, and superficial lubrication, should be comparable to the host tissue to allow the maintenance of its structural integrity. It should also allow good integration with native cartilage and bone<sup>5,28,29</sup>.

- Fabrication method: the scaffold manufacturing process should be precise, reproducible and versatile to allow individualized patient-tailored designs<sup>5,28-31</sup>.

In the next paragraphs, an overview of the materials and scaffold architectures that have been employed in OC TE strategies will be presented.

#### *Composition*

A wide variety of materials have been used to fabricate scaffolds in OC TE strategies. They can be grouped in natural or synthetic polymers, inorganic materials, ECM-based materials, metals, and composites of the aforementioned materials. Table 2.1 provides an overview of those materials, highlighting some of their advantages and limitations<sup>5,13,25,28,30-35</sup>.

Table 2.1 – Overview of commonly used scaffold materials for osteochondral tissue engineering (adapted from <sup>5,28</sup>).

Material type	Advantages	Limitations	Examples
Natural polymers: Poly-saccharide	- Biomimicry with ECM (are a component of ECM or have similar structure) - Biocompatibility - Biodegradability	- Poor mechanical properties - Potential immunogenicity (in some cases) - Rapid degradation	Hyaluronic acid (HA) Chondroitin sulfate (CS) Alginate Agarose Chitosan
Protein based	- Little or none inflammatory response	- Batch-to-batch variability - Lower bioactivity from non-human polymers	Collagen Gelatin Silk fibroin
Synthetic polymers	- Consistent product characteristics - Good biocompatibility - Wide range of compositions and properties - Versatility Ease of modification - Low immunogenicity	- Low bioactivity or inert for cellular interaction - Possibility of undesirable or acidic degradation products	Poly(ethylene glycol) (PEG) Poly(ethylene oxide) (PEO) Polylactic acid (PLA) Poly(lactic acid-co-glycolic acid) (PLGA) Poly( $\epsilon$ -caprolactone) (PCL) Poly(vinyl alcohol) (PVA) Poly(L-glutamic acid) Poly(propylene fumarate) (PPF) Poly(N-isopropyl acrylamide) (PNIPAAm)
Bioceramics	- Biocompatibility - Bioactivity - Mechanical strength	- Brittleness - Mimic mostly bone	Hydroxyapatite (HAp) ( $\text{Ca}_5(\text{PO}_4)_3(\text{OH})$ ) Tricalcium phosphate (TCP) ( $\text{Ca}_3(\text{PO}_4)_2$ ) Calcium silicate Bioactive glass (BG)
Metals and their alloys	- Mechanical strength - Biocompatible	- Lack of biodegradability (in many cases) - Risk of stress shielding - Mimic mostly bone	Titanium Magnesium Zinc
ECM-based materials	- Similarity to the complex composition of ECM - Bioactivity and tissue specificity	- Poor reproducibility - Limited standards for decellularization	Decellularized ECM Pulverized ECM particles for composite fabrication

Natural polymers acquired widespread use in OC TE due to their biocompatibility, biodegradability and structural similarity to native biomolecules. However, some limitations like a poor mechanical behavior, a biological performance depending on the production batch, a quick degradation and some



purification difficulties that could lead to immunological responses still need to be addressed<sup>25,31</sup>. Polymers like hyaluronic acid (HA), chondroitin sulphate (CS), collagen, which are constituents of the ECM, show higher bioactivity than polymers not present in the ECM like alginate, agarose, and chitosan<sup>5,25</sup>. One polymer gaining particular attention is silk, due to its improved mechanical strength, good biocompatibility, slow degradability, and for being easily processed<sup>31,32</sup>.

Also very widely used, synthetic polymers allow higher reproducibility and control over chemical features, like molecular weight or degradation rate. Nevertheless, they usually show impaired bioactivity, owing to the lack of bio-adhesive motifs and to a more hydrophobic character when compared to natural polymers<sup>13,30,33</sup>. A range of molecular alterations facilitate tailoring some of its properties<sup>32</sup>. In terms of mechanical properties, synthetic polymers show a superior behavior in comparison to natural polymers<sup>5,25</sup>.

As the most acknowledged materials for the reconstruction and replacement of damaged bone, bioceramics have been widely combined with natural or synthetic polymers to create composite scaffolds for bone regeneration. Considering the poor elasticity and high stiffness of bioceramics, the combination with polymers gives them the improved properties that complement their biocompatibility and bioactivity<sup>28,32</sup>. Included in this group of bioceramics are HAp, the major component of natural bone tissue; tricalcium phosphate (TCP), a calcium phosphate like HAp but with a slightly different structure; calcium silicate, a material that allows a prolonged release of incorporated bioactive ions with important roles in bone regeneration; and bioglasses (BG), which have a very high interaction with bone, accelerating the rate of bone regeneration<sup>5,28,32</sup>.

Metals have been used mainly for bone TE, due to their high mechanical strength and biocompatibility, which has led to investigations where metals are employed as the bony phase in OC regeneration<sup>5,13</sup>. Material wise, titanium alloys are not biodegradable and may need to be surgically removed after serving their supportive regeneration role; on the other hand, materials made of magnesium are biodegradable by corrosion and could therefore be amenable to be used in distinct bone TE strategies<sup>28,32</sup>.

ECM has a highly complex structure and, for that reason, hardly any of the previous materials will fully mimic the tissue's microenvironment. Thus, tissue or cell decellularization and removal of all genetic material emerged as a suitable alternative material with the physical and biochemical characteristics that could support a variety of microenvironments for cell survival, organization and differentiation<sup>13,25,30</sup>. Even when used in pulverized form in combination with other materials, the various molecules from ECM still display a bioactive role in OC regeneration. However, some issues remain concerning reproducibility due to variable ECM origin and limited standards for decellularization protocols<sup>5,13,25</sup>.

Consisting of a combination of two or more materials, composites constitute an increasingly significant class of biomaterials, owing to the ability of outperforming their individual constituents<sup>32</sup>. Given the composite nature of OC tissue and its complex gradient structure, composite biomaterials have been offering new solutions for replicating the native tissue, many examples of which can be found in the literature<sup>5,25,28,31-33</sup>.

The main material utilized in the present thesis project, poly( $\epsilon$ -caprolactone) (PCL) (Figure 2.4) is a synthetic polymer that has been widely used in OC TE strategies, which was previously approved by

the FDA for therapeutic use<sup>28,32</sup>. Among its particular characteristics are its good mechanical strength and slow hydrolytic degradation *in vivo*<sup>32</sup>. However, being hydrophobic, it often leads to suboptimal cellular outcomes<sup>36</sup>. Because of that, strategies like coating with other materials and the creation of PCL-based composites have been widely used to increase hydrophilicity<sup>5,32</sup>.

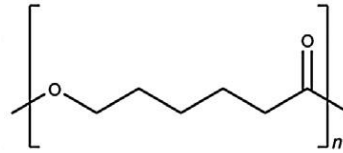


Figure 2.4 – Structure of poly(ε-caprolactone) (PCL) (adapted from<sup>37</sup>).

### Architecture

In the manufacturing of a scaffold able to regenerate OC defects, architecture is a critical factor to consider. AC and subchondral bone have a very distinct composition, structure, and biomechanical, and biological features. Ideally, the manufactured scaffold should be able to replicate this complex structure, and also be able to fully integrate with the surrounding native tissue<sup>30,38</sup>. The improved understanding of OC biology and the advance in the fabrication technologies has led to progress in scaffold design, creating more complex and dissimilar structures, represented in Figure 2.5. The hierarchical organization of scaffolds has allowed the creation of tissue specific environments, by variation of chemical, structural and mechanical properties, in order to match three important distinct layers, i.e., AC, subchondral bone and the interface between them, the calcified cartilage<sup>39</sup>.

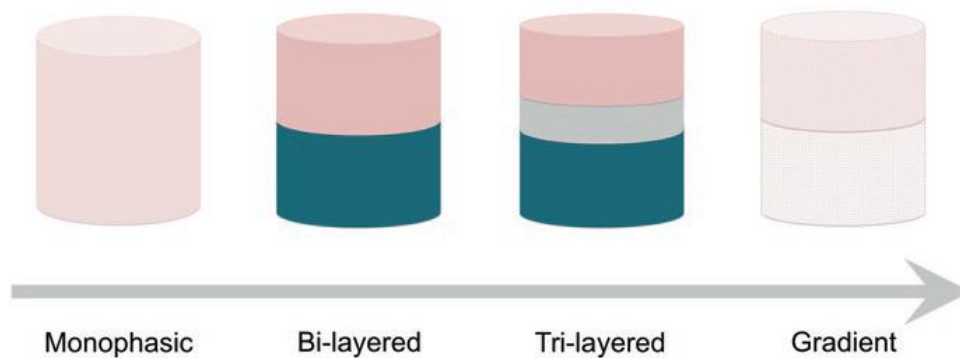


Figure 2.5 – Evolution of explored strategies for scaffold construction for osteochondral tissue engineering (adapted from<sup>39</sup>).

Monophasic scaffolds, for their simplicity, were among the first explored strategies<sup>5,39</sup>. They are composed by a single biomaterial or composite with no spatiotemporal variation, either biological or physical. There are still some recent studies that report concurrent regeneration of cartilage and subchondral bone with this type of scaffolds, however it is acknowledged that they don't fulfil all requirements, in terms of mimicking the native structure, for effective regeneration of OC lesions<sup>5</sup>.

The bilayer scaffold strategy inspired by the anatomical architecture aims to mimic both AC and subchondral bone features. Usually, the manufacture of this type of scaffolds is accomplished by the production of the two independent layers which are then combined into one by means of suturing, glue

or press fitting<sup>40</sup>. Alternatively, it can also be composed of a single material, but with the architecture varying between the two phases, or composed by two materials united by a binder that integrates the whole structure<sup>5,38,39</sup>. Of great importance in these scaffolds is the interface integration between the two layers, since a poor integration may lead to delamination and total layer separation, resulting in failure of tissue regeneration<sup>5,39</sup>.

Realizing the significance of the calcified zone, with a distinct cellular population and ECM composition, working as a linkage between cartilage and bone, researchers have been making considerable efforts to create scaffolds with a closer resemblance to native tissue<sup>25</sup>, and therefore several tri-layered scaffold designs have been described<sup>5,39,40</sup>.

Native OC tissue displays a much more intricate gradient heterogeneity instead of the stratification into three distinct regions. To replicate this reality, scaffolds have been built that exhibit multiphasic discrete gradients (more than three layers) or a continuous variation throughout the whole scaffold or within a limited section<sup>5,39</sup>. This type of construction usually performs better than monophasic or biphasic constructs<sup>5</sup>. The gradient variation in these scaffolds may relate to many of the scaffold's characteristics: chemical composition, and structural characteristics like arrangement, distribution, dimension and orientation (Figure 2.6)<sup>41</sup>.

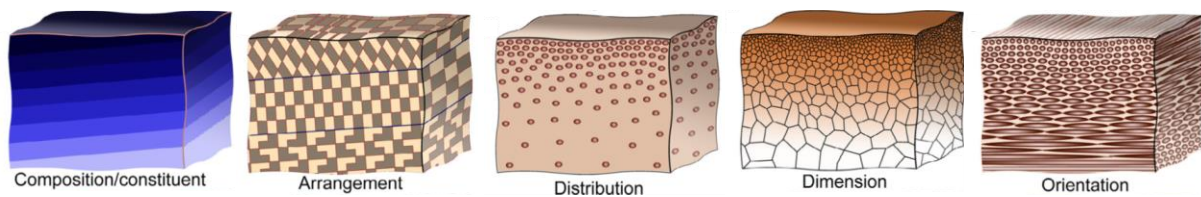


Figure 2.6 – Basic forms of gradients in biological materials. Gradients are fundamentally associated with the changes in chemical compositions/constituents, and structural characteristics like arrangement, distribution, dimension and orientation (adapted from <sup>41</sup>).

### *Pore morphology*

A key requirement for a scaffold in OC TE is that it provides mechanical support, especially in load-bearing areas. However, the size and structure of the pores within the scaffold must also be considered to allow cell and tissue infiltration, vascularization (in the case of bone) and to elicit the appropriate biological response<sup>34</sup>. Pore size and porosity are two of the most important scaffold parameters, with cell proliferation and differentiation directly affected by them. For example, for the case of bone, larger pore sizes (greater than 300  $\mu\text{m}$ ) are recommended for bone ingrowth and vascularization<sup>42</sup>, while for chondrocytes, pores between 250 and 500  $\mu\text{m}$  were preferential for cell proliferation and ECM production, but pores smaller than 200  $\mu\text{m}$  lead to dedifferentiation<sup>43</sup>. There is, however, an effect on the scaffold mechanical properties. Higher porosity may provide more volume for cell infiltration and ECM production, but conversely decrease mechanical properties, and a compromise must be met so that the scaffold has comparable strength to native tissue and can maintain integrity until new tissue is formed<sup>42,43</sup>. Finally, porosity can also affect cell behavior by altering fluid shear forces exerted on cells<sup>34</sup>.

Interconnectivity, represented in Figure 2.7, is another significant factor. Pores should be connected to support cell proliferation and migration throughout the whole scaffold. High interconnectivity can even

be more critical than pore size, providing molecular diffusion within the whole scaffold and allowing an homogenous tissue growth<sup>42</sup>.

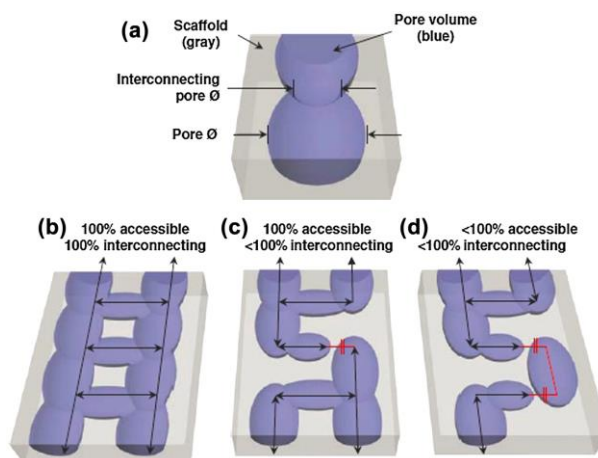


Figure 2.7 – Illustration of the relationship between pore morphology and interconnectivity (adapted from <sup>42</sup>).

Thus, as scaffolds become more sophisticated, multiple parameters can be used to characterize them, and the ones morphologically more relevant are summarized in Table 2.2. It is important to do this characterization as thoroughly as possible, to have the possibility to do accurate comparisons between different studies<sup>34,42,44</sup>.

Table 2.2 – Morphologic parameters for porous scaffold characterization (adapted from <sup>34,44</sup>).

Property	Definition	Biological response
Total porosity	Percentage of total void space	Affects cell recruitment, attachment, and vascularization. Also affects mechanical strength of the scaffold.
Open porosity	Percentage of pores that are interconnected	Determines geometry of resulting tissue. Affects cell permeability and tissue infiltration, as well as molecular diffusion.
Pore size	Diameter of largest sphere that fits within pore channel	Affects cell infiltration, migration, proliferation, distribution, ECM deposition and distribution, nutrient, and oxygen exchange.
Pore gradient	Difference in pore diameter, total porosity, or other porosity parameter. This is not standardized and can be expressed in multiple ways	Localized and gradient porosity have been proposed to increase tissue specific growth during the regeneration process. This allows nutrient transport throughout the scaffold based on the scaffold and tissue architecture.

Property	Definition	Biological response
Tortuosity	Quantification of twists and turns expressed as the length of the entire channel divided by the shortest distance between starting and ending points	Affects surface area, cell migration, delivery of nutrients and removal of waste.
Surface area to volume ratio	Ratio of total scaffold surface area to total scaffold volume	Should be considered when defining cell seeding density and concentration of functionalization factors on scaffolds.
Swelling ratio	The ratio of wet mass or volume to dry mass or volume of a hydrogel	Swelling can affect delivery of growth factors or oxygen diffusion, leading to changes in cell response. Rate of swelling may also affect cell attachment and proliferation.

### 2.2.2. Cells

Currently, many TE strategies involve the use of cells for the creation of the OC tissue substitutes<sup>21</sup>. Influencing the way the surrounding host tissue interacts with the scaffold, the cellular components are considered to improve the outcome of tissue regeneration<sup>5</sup>. Ideally, the selected cells should be easily expandable, non-immunogenic and express a protein pattern similar to the host tissue<sup>17</sup>. However, there are few cell types to choose from, and there are limitations in the available cell populations<sup>45</sup>. Cell sources usually fit into one of two groups, either progenitor cells or tissue specific cells<sup>4,18,21</sup>. The most common choices of tissue specific cells used in OC TE strategies are chondrocytes, in the case of AC, and osteoblasts, in the case of bone. Chondrocytes are mainly isolated from the non-load bearing region of AC, but alternative sources like the nasal septum and auricle have also been reported<sup>5,26</sup>. Owing to the small number of chondrocytes found in the body and the difficulties isolating them from the matrix, chondrocytes need to be expanded *in vitro*<sup>21</sup>. This is a risk, since chondrocytes can easily lose their phenotype during *in vitro* culture and therefore lose therapeutic value<sup>45</sup>. Several different approaches were developed to prevent chondrocyte dedifferentiation, including the use of growth factors, mechanical stimulation (e.g., hydrostatic pressure), limiting the levels of oxygen (hypoxia) in the environment<sup>45</sup> and also providing an adequate 3D scaffold architecture<sup>5</sup>. However, chondrocytes expand slowly in culture, and the longer it takes, the greater is the chance of losing their phenotype<sup>45</sup>. The use of allogeneic chondrocytes is an alternative, although drawbacks as immunological intolerance and the possibility of disease transmission need to be considered<sup>45</sup>. Considering osteoblasts, they would need to be isolated from biopsies and expanded *in vitro*. However, this methodology is time consuming since there are relatively few cells available, and the expansion rate is low. The immunogenicity of osteoblasts and the possibility of transmitting infectious agents has also refrained the use of allogeneic sources<sup>45</sup>.

To overcome the limited supply of primary cells, stem cells have been widely used in OC TE, owing to their availability and capacity of *in vitro* expansion (Figure 2.8)<sup>26,45</sup>. Various cell sources have been studied and employed, including embryonic stem cells (ESCs), induced pluripotent stem cells (iPSCs) and mesenchymal stem/stromal cells (MSCs)<sup>5,20,45</sup>. Concerning MSCs, they have been isolated from a range of different tissues, such as bone marrow, adipose tissue, synovium, periosteum, muscle, dental pulp, infrapatellar fat pad, dermis, blood, or the umbilical cord<sup>20,45,46</sup>. Ideally, MSCs should allow easy accessibility, minimally invasive harvesting and yield usable number of cells, however, each MSC source presents its particular set of advantages and disadvantages. Bone marrow-derived MSCs (BMSCs) are the most widely studied source in OC TE<sup>46</sup>. They have the ability to differentiate into chondrogenic or osteogenic lineages, however their isolation procedure is painful and the yield of stem cells is very low<sup>20</sup>, requiring considerable expansion which may result in reduced differentiation capacity and therapeutic efficiency<sup>46</sup>. Another limitation is the number of available cells, which decreases with age and is a critical problem since OC diseases tend to manifest later in life<sup>46</sup>. Adipose derived stem cells (ADSCs) have been increasingly used as a cell source since they can be harvested in generous amounts through a relatively simple procedure. They are present in high amounts in adipose tissue and allow a much higher yield in isolation compared to BMSCs<sup>20,45,46</sup>. They have shown potential for chondrogenic and osteogenic differentiation, although a tendency to adipogenic differentiation has also been observed<sup>5,46</sup>. Considering only chondrogenic differentiation, many studies indicate a greater potential from BMSCs than ADSCs. Another MSC source for chondrogenesis, synovium derived MSCs (SMSCs) have demonstrated a greater potential compared to bone marrow, periosteum, muscle, and adipose sources. They share some characteristics with chondrocytes, including similar gene expression profiles (e.g., superficial zone protein, type II collagen, aggrecan). They are able to form hyaline cartilage cultured *in vitro*, which is of great value for OC regeneration. They can also be harvested from the synovial fluid, however the yield is relatively low<sup>45</sup>.

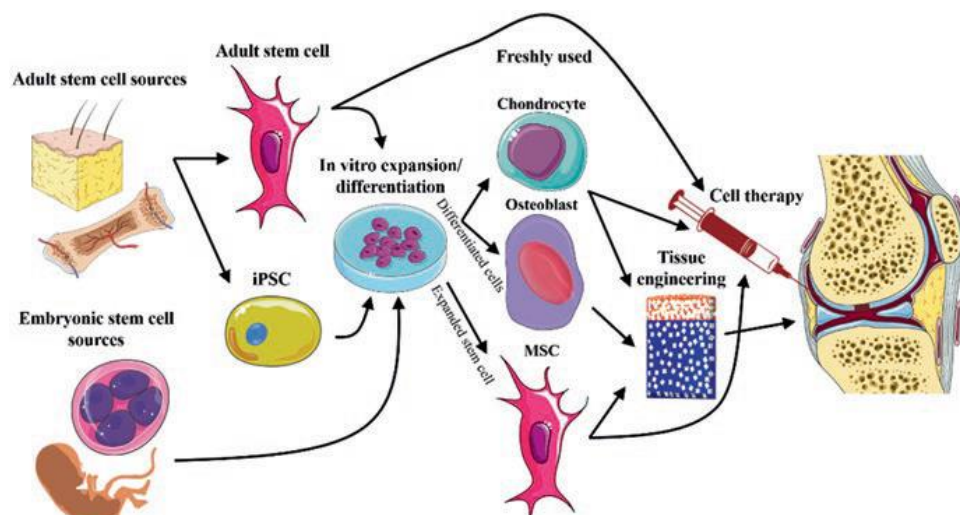


Figure 2.8 – Stem cell-based strategies for bone and cartilage tissue engineering (adapted from <sup>46</sup>).

ESCs have also gathered some attention, due to its proliferative potential and differentiation capacity<sup>17</sup>. However, ethical constrains and tumorigenic risk have limited their clinical use<sup>46</sup>. Avoiding this limitation, iPSCs have also been studied as a potential source for restoring cartilage and bone

defects<sup>5</sup>. Still, there are some concerns about the safety of these cells, namely the optimal practices for isolation, purification and differentiation, undesired genetic modifications from reprogramming protocols, and the potential for *in vivo* tissue malformations<sup>27</sup>.

### 2.2.3. Biochemical and physical factors

Signaling factors play a significant role in OC TE, regulating critical processes such as cell growth, differentiation, or tissue homeostasis. These factors can be biochemical, physicochemical or physical in nature and modulate cell behavior by the activation of relevant pathways and expression of particular proteins<sup>5,26,40</sup>. In the following paragraphs, the role of the most relevant biochemical/physical factors for OC regeneration will be briefly described.

Regarding biochemical factors, members of the transforming growth factor- $\beta$  (TGF- $\beta$ ) superfamily (that include bone morphogenetic proteins (BMPs)), the insulin growth factor-1 (IGF-1), and the fibroblast growth factors (FGFs), are among the most widely used for cartilage and bone TE strategies<sup>5,26,47</sup>. Within the TGF- $\beta$  family, isoforms 1, 2, and 3 have largely been described as promoters of MSCs proliferation and differentiation into chondrocytes and osteocytes, and also of the synthesis of proteoglycans and collagen type II by chondrocytes<sup>26,47</sup>. However, results from studies where intra-articular injections were performed have shown that adverse effects from longer exposures (over 3 weeks) to these factors may occur, indicating that a tightly coordinated control is necessary<sup>48</sup>. BMPs constitute a sub-class of 20 polypeptides in the TGF- $\beta$  superfamily. They play important roles in cartilage and bone formation during skeletal development, and are also involved in the activation of regenerative processes after injury<sup>5,49</sup>. Numerous studies have been made with BMPs, used alone or combined with other molecules, and they demonstrated to have great potential for cartilage and bone regeneration, both *in vitro* and *in vivo*<sup>49</sup>. Still, many challenges need to be tackled before therapeutic use, namely, an efficient delivery system, how to address the fast degradation, determining in which cell types BMPs are more effective, and the best combination with other factors to potentiate BMPs action<sup>49</sup>. IGF-1 belongs to a family named for its similarity to the sequence of insulin, and is constituted by two polypeptide ligands, IGF-1 and IGF-2. Since many types of cells can express them, they have a relevant influence in a variety of tissues, and their role in the regulation of proliferation, differentiation, and apoptosis has been shown. While IGF-2 has a role mainly during embryonic and fetal development, IGF-1 has been found to be more relevant for cartilage regeneration, taking part in the regulation of proteoglycan synthesis and breakdown and supporting chondrocyte survival and proliferation<sup>5,26,50</sup>. Furthermore, it has also been reported to promote both chondrogenesis and osteogenesis from MSCs<sup>51</sup>. In mammals, the FGF family contains 18 signaling proteins that can bind and activate one of the four receptor tyrosine kinase molecules (FGF receptors). They are differently expressed in most tissues of the developing embryo, where they regulate many developmental and organogenesis processes<sup>52,53</sup>. They are also expressed in postnatal and adult tissues, functioning as regulating factors in tissue maintenance, repair, and regeneration<sup>52</sup>. Among them, FGF-2 and FGF-18 have been described as having greater influence in skeletal development and chondrogenesis<sup>5,53</sup>. Studies have been conducted to test their effect, however reporting mixed results, with FGF-2 being described to promote bone healing and promoting chondrocyte proliferation<sup>5</sup>, while other studies indicating FGF-2 role in antagonizing the proteoglycan

synthesis and resulting in inflammation and osteophyte formation<sup>50</sup>. Mixed results have also been reported for FGF-18, promoting chondrocyte proliferation in monolayer culture and being used for bone defect repair<sup>5</sup>, but also being associated with chondrocyte formation<sup>50</sup>.

These results underline the importance of having tight control over the duration of growth factor exposure, as it is also appreciated from native chondrogenesis and osteogenesis, in which the time-dependent involvement of different growth and differentiation factors is crucial for normal tissue formation<sup>26,47,54</sup>.

Considering other signaling factors, physicochemical factors (e.g., oxygen tension) and physical factors (e.g., mechanical stimuli), also have a significant effect on OC cell and tissue behavior<sup>5,47</sup>. Since early embryonic development chemical gradients are established due to nutrients and oxygen being supplied by diffusion. In particular, in endochondral ossification, as fetal growth plate develops and becomes more hypoxic, chondrocytes go through a well-coordinated process of proliferation, differentiation and apoptosis, leading to bone growth<sup>47,55</sup>. As such, chondrocytes are a cell type that has developed an adaptation to low oxygen concentrations, which range from about 7% in the superficial layer, supplied by the synovial fluid, to about 1% in the deep zone, closer to the subchondral bone<sup>56</sup>. Evidence suggests that the transcription factor hypoxia-inducible factor 1 (HIF-1) is one of the major regulators of the hypoxic response that mediates a cascade response to low oxygen conditions<sup>47,55</sup>. Vascularization, in deep cartilage closer to bone, can be mediated by vascular endothelial growth factor (VEGF), which is a target of the HIF pathway, further highlighting the role oxygen tension can have<sup>47,55,56</sup>. Experimental results showed that hypoxic culture conditions can lead to increased matrix formation by chondrocytes and improved chondrogenic differentiation of MSCs<sup>5,47,56</sup>.

Mechanical stimuli are sensed by cells through mechanotransduction. It is a process through which the stimuli set off chemical signaling cascades inside the cells eliciting specific responses<sup>57</sup>. It has been described that this physiological stimulation is a preeminent factor for chondrogenic differentiation of MSCs and that it is essential for physiological maintenance of cartilage integrity<sup>26</sup>. Further, in native tissue, cyclic loads are responsible for the mass transfer of oxygen, nutrients and waste, due to fluid flowing in and out of the ECM, in reaction to deformations caused by the stimuli<sup>58,59</sup>. These mechanical forces can be transmitted through several media, namely liquid (hydrostatic pressure, fluid shear stress), solid (compression and in combination with shear stress), and other noncontact (electromagnetic forces, microgravity, ultrasounds, etc.)<sup>58</sup>. Experimentally, it has already been verified that *in vitro* mechanical stimulation in bioreactors does improve cartilage production as well as its properties<sup>5,58</sup>.

### *Electrical stimuli*

The importance of bioelectricity for cells, beyond nerve and muscle tissues, has been identified for some time and established that it plays a key role in regulating several biological processes including embryonic development, wound healing, tissue repair and remodeling. Bioelectricity is also considered essential to maintain cellular homeostasis and is invoked in many biological events<sup>60,61</sup>. Native electric properties like resting membrane potential, ionic current flow, resistance, capacitance, permittivity and conductivity will vary according to tissue type, health, age, and stage of development<sup>62</sup>.



From a TE perspective, a greater control over many cellular processes could be gained through the application of external electrical stimuli. With a closer approximation to *in vivo* environment, the quality of tissue engineered constructs could be significantly improved<sup>63</sup>. As examples of the use of electrical stimulation (ES) in TE strategies, it has been explored to improve the contractile and conductive properties of cardiac constructs, to promote the proliferation and differentiation of stem cells, cellular alignment, and to increase the length of neurite outgrowth<sup>63</sup>. ES has also been used in clinical settings to relieve pain, increase blood circulation, decrease muscle tension, and to stimulate reabsorption of edema and joint fluid<sup>64</sup>.

Although favorable biochemical and physiological responses can be triggered by ES, the mechanisms through which it interacts with biological systems are not totally understood, with its effect possibly being exerted directly on the cell or indirectly through alterations in the extracellular environment<sup>60</sup>. Additionally, the fact that ES has its own characteristic dynamics is also relevant, working at the same time as biochemical signals. The situation may occur in which there is a conflict in the response to those two types of signals and, in that case, electrical signals tend to be dominant<sup>61</sup>. ES also does not reduce to molecular genetic profiling. Due to posttranslational channel and pump regulation, cells with the same profiles can be in different bioelectrical states, or cells expressing different channels and pumps can be in the same state<sup>61</sup>.

Cells are the main source of *in vivo* electricity, due to the voltage gradient they establish across their membrane<sup>61,63</sup>. Changes in that gradient caused by ES influence the movement and concentration profiles of charged cytoplasmic molecules, interfering with the transmembrane potential that can elicit membrane changes, causing an accumulation of molecules along the membrane or modulating conformational states of membrane proteins, which in turn will trigger different cellular responses<sup>60</sup>. In Figure 2.9 some cellular processes influenced by electrical stimuli are represented as well as a summary of the mechanisms by which ES exerts its effect at the cellular level.

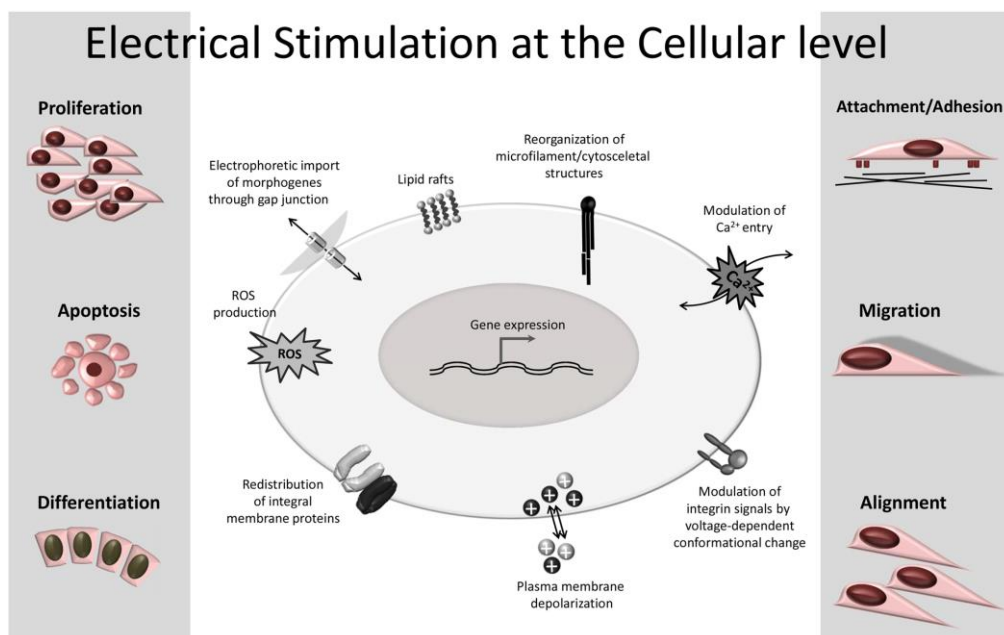


Figure 2.9 – Overview of cellular mechanisms and functions activated by electrical stimulation (adapted from <sup>65</sup>).

Several studies have been conducted revealing the effects of ES in cell behavior. In terms of proliferation, electrical stimuli appears to promote cell growth, however a decrease or effect absence has also been observed<sup>60</sup>. The effect on apoptosis is not noticeably clear, but studies suggest that it is heavily dependent on the cell type and stimulation regimen<sup>65</sup>. In many studies, ES is also referred as an approach to induce stem cell differentiation<sup>60,65</sup>. In tissue development, cell alignment and migration play critical roles, and ES has also been explored to modulate such cellular processes. However, depending on cell type and nature of stimulation, cells have been observed to align parallel or perpendicular to the electric field, and to migrate towards or against the field. Overall, ES has the potential to modulate many cellular behaviors relevant for TE strategies, but a more profound knowledge is still required to better understand the underlying mechanisms by which the electrical stimuli regulate cell behavior as well as which type of stimulation is best suitable for a specific cell type and the time dependence of stimulation<sup>60,64,65</sup>.

Many mechanisms have been described mediating the cellular response to ES, which will be briefly mentioned: i) through signal transduction pathways, cells sense electrical signals and convert them into biochemical cues, leading to the activation of different pathways and modulating gene expression, eliciting variable biological responses; ii) increasing intracellular  $Ca^{2+}$ , which is an important mediator in many cellular processes; iii) by cytoskeletal reorganization and actin distribution, intervening on cellular processes regulated by the cytoskeleton; iv) by surface receptor redistribution, changing cellular responses by altering ligand-receptor interactions; v) altering ATP synthesis, usually increasing its rate; vi) upregulating the production of heat shock proteins, inducing particular stress responses; vii) increasing the generation of reactive oxygen species, which participation is important in different signaling pathways; viii) conducting to the formation of lipid rafts which in turn trigger intracellular signaling events. The observable cellular and tissue responses to ES may consist of all these mechanisms, working in a finely orchestrated network of signals and responses<sup>60,65</sup>.

### 2.3. Electrically conductive polymers in tissue engineering

Conducting polymers (CPs) are a group of organic materials that have electrical and optical properties close to those of metals and inorganic semiconductors, but which also display the desirable properties of ease of synthesis and flexibility in processing associated with conventional polymers<sup>66,67</sup>. Considering that tissues are responsive to ES, CPs became attractive to biological and medical applications, such as bioactuators, biosensors, neural implants, drug delivery systems, and TE scaffolds<sup>67,68</sup>. Their advantages include biocompatibility, ability to entrap and release in a controlled manner biological molecules, ability to transfer charge from a biochemical reaction, and their versatility, namely the possibility to change the electrical, chemical, physical, and other properties of the CPs to better suit the nature of the specific application<sup>67</sup>.

Polypyrrole (PPy), polyaniline (PANI), and polythiophene (PT) and its derivatives (e.g., PEDOT) are the most extensively studied CPs, and its structure is represented in Figure 2.10. Disadvantages of CPs include mechanical brittleness and poor processability, and for that reason composites based on CPs and biocompatible biodegradable polymers, natural or synthetic, have been developed exploiting positive aspects from both components<sup>66,68</sup>.

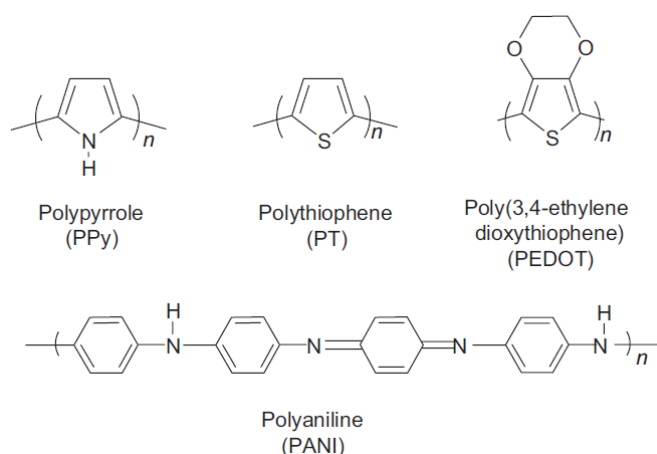


Figure 2.10 – Chemical structure of commonly explored conducting polymers for biomedical applications: polypyrrole (PPy), polythiophene (PT), poly(3,4-ethylenedioxythiophene) (PEDOT), and polyaniline (PANI) (adapted from <sup>67</sup>).

One particular PT derivative is PEDOT, which is obtained through the oxidative polymerization of 3,4-ethylenedioxythiophene (EDOT). PEDOT has a high conductivity and high stability in its oxidized state. It can be coupled with another polymer, poly(styrene sulfonate) (PSS), creating a water based stable colloidal suspension, which also has the effect of improving its conductivity by stabilizing the positively charged bipolaron of PEDOT with the negatively charged PSS anions<sup>69</sup>. Owing to its characteristics, PEDOT:PSS (Figure 2.11) became one of the most used and studied CP in TE, and strategies have been developed to enhance some of its properties, namely conductivity and adhesion. One method found to improve conductivity was the use of a co-solvent, with a proposed mechanism that involves the intercalation of the solvent molecules between the PEDOT and the PSS moieties, which leads to the stabilization of linear forms of the PEDOT chain as well as to the removal of excess PSS that causes a small loss of conductivity. Maintaining the adhesion is a requirement for long term biological applications, and the poor mechanical stability of PEDOT:PSS is a major drawback. To address this limitation, the addition of cross-linkers such as (3-glycidyloxypropyl) trimethoxysilane (GOPS) or divinyl sulfone (DVS) (Figure 2.11) is the most explored strategy. Although a decrease in conductivity may be seen, the adhesion can be greatly improved<sup>69</sup>.

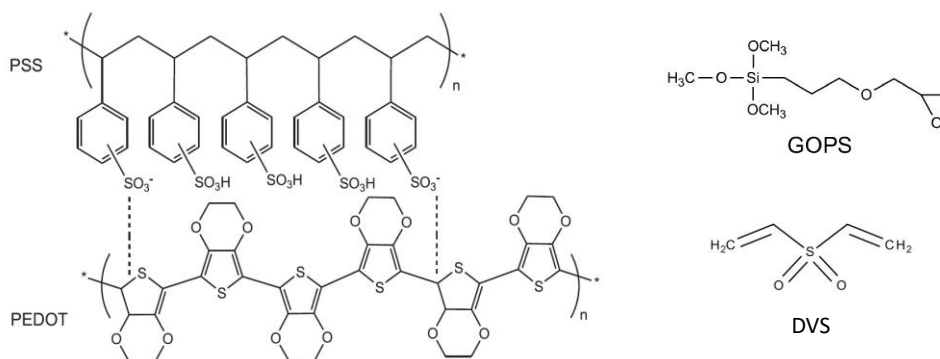


Figure 2.11 – Chemical structure of PEDOT:PSS and cross-linkers GOPS and DVS used to increase its mechanical stability (adapted from <sup>70-72</sup>).

## 2.4. Scaffold fabrication techniques

Many features of TE scaffolds are related to the properties of the materials used but also to scaffold geometry, which is closely related to the manufacturing technology<sup>25</sup>. Available 3D fabrication technologies can be divided into two main categories, conventional and additive manufacturing (AM), each producing scaffolds with different characteristics. Conventional techniques use subtractive methods, in which parts of a material are removed to obtain the final conformation, while in AM the final construction is obtained by successive deposition of overlying layers<sup>35</sup>.

Although conventional techniques are still often used, they have well known limitations for the fabrication of complex 3D constructs, which restrict their scope of applications<sup>32,35,73,74</sup>. Some of the more recognized limitations include:

- Conventional techniques rely on manual intervention and are poorly scalable. Many require multi-stage processing, and the final product may be contingent on the manufacturer's experience, with inconsistent results and poor reproducibility<sup>32,73</sup>;

- They offer limited ability to control shapes and geometries, therefore do not allow the creation of complex designs with well interconnected pores or curved channels in the internal architecture, and a predictable and variable geometry at the macro and micro level<sup>75</sup>. Fabricated scaffolds usually possess inconsistent pore sizes, morphologies, porosities and internal surface area<sup>73,74</sup>;

- The use of organic solvents and porogens, in the scaffold fabrication process. Their incomplete removal or entrapment inside closed pores might have adverse effects compromising cell viability and the biological performance of the scaffold<sup>35,73</sup>;

- The shape of the scaffolds is usually restricted by the shape of the mold or container where they are fabricated, limiting the possibility of creating patient specific geometries. Although some techniques may allow the creation of irregularly shaped scaffolds, the process would be tedious and time consuming<sup>73</sup>.

More recently, AM has been applied to overcome the abovementioned limitations, offering superior scalability and allowing the fabrication of constructs with improved control over their microstructure and composition<sup>32,35,74</sup>. AM can be defined as "the process of joining materials to make objects from three-dimensional (3D) model data, usually layer upon layer"<sup>76</sup>. This 3D model data can be derived from medical imaging techniques used for diagnostic purposes, such as magnetic resonance imaging (MRI) and computer tomography (CT). Based on the 3D models generated, the fabricated scaffold must mimic the structure and properties of the native tissue<sup>77</sup>. They are generally treated by computer-aided design (CAD) and manufactured via computer-aided manufacturing (CAM) software. Alternatively, a 3D model could be directly designed in CAD software or developed by means of mathematical equations or topological optimization<sup>76,78</sup>.

The production of a part usually follows a typical process chain. After obtaining the medical images or a design is created, the CAD software then converts the 3D model into a file containing the information of the object's 3D surface geometry. It is then sliced into layers, by means of specific slicer software, with information, for each layer, of how to control the motion of the build parts of the manufacturing device. It is then fabricated through the most suited AM technique, after which a final stage of post processing processes (e.g., finishing and cleaning) completes the production<sup>73,76</sup>.

In the following subsections the main characteristics of the most common conventional and AM fabrication techniques will be overviewed.

### 2.4.1. Conventional techniques

The most common conventional techniques, namely solvent casting/particle leaching, freeze-drying, gas foaming, phase separation, and electrospinning, are represented in Figure 2.12.

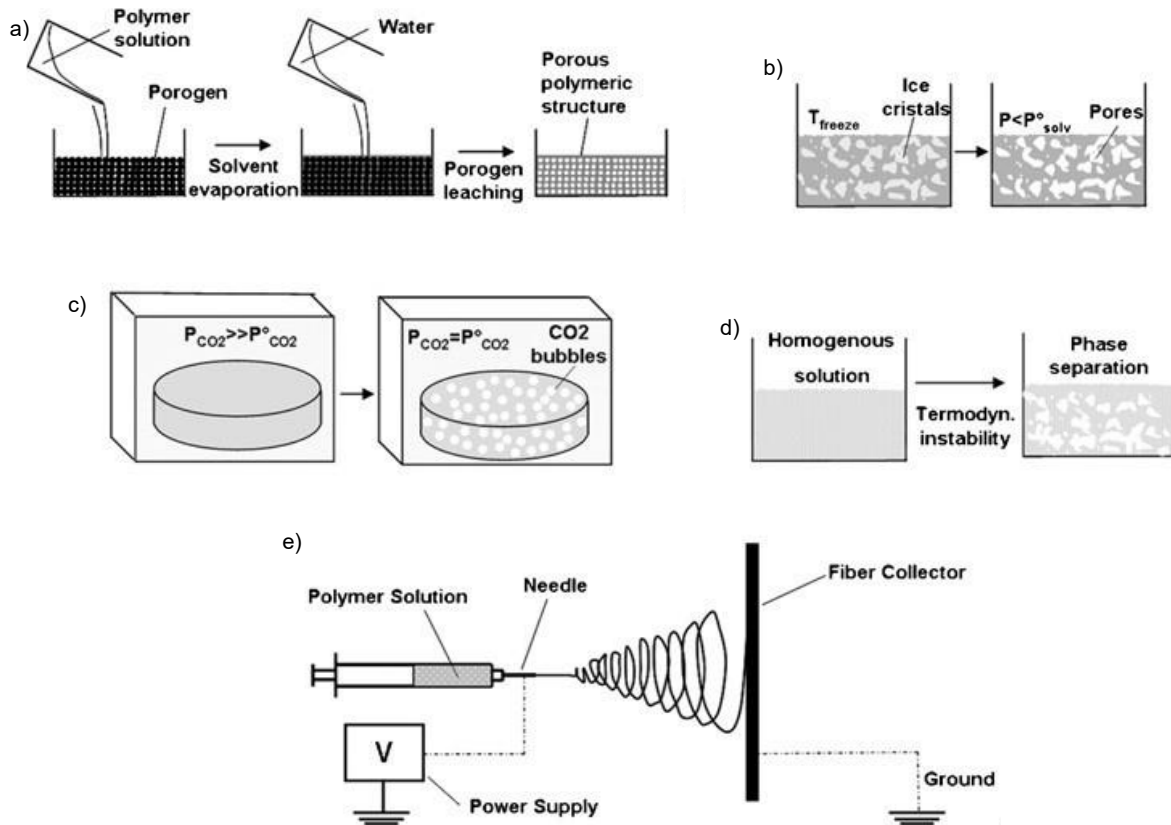


Figure 2.12 – Schematic representation of commonly used techniques for scaffold production: a) Solvent casting/particle leaching; b) Freeze drying or lyophilization; c) Gas foaming; d) Phase separation; e) Electrospinning (adapted from <sup>36</sup>).

Solvent casting/particle leaching (Figure 2.12a) is a method that allows the creation of a porous structure with regular porosity but with a limited thickness, up to 2 mm. It involves dissolving a polymer into an adequate solvent and casting the solution into a predefined mold filled with porogen particles. Porogens are substances like inorganic salts (e.g., sodium chloride), crystals of saccharose, gelatin or paraffin spheres, which can be dispersed into a molded structure and subsequently dissolved once the structure has set. Pore size and porosity of the final structure is directly affected by the porogen particle size and polymer to porogen ratio. Once the structure has set, the solvent is allowed to evaporate, leaving behind a polymer matrix with porogen particles embedded. Afterwards, the structure is immersed in a bath of water or suitable solvent to dissolve the porogen, thus generating a porous structure. The advantages of this method include the ease of fabrication, without the need for specialized equipment, and the ability to create a wide range of pore sizes. Among the disadvantages, there is some difficulty

in controlling pore shape and interconnectivity, the use of organic solvents which could be harmful to cell viability and the restriction to produce simple shapes like flat sheets and tubes<sup>28,35,36</sup>.

The freeze-drying or lyophilization process (Figure 2.12b) involves a solvent, usually water, being removed from a frozen sample by sublimation. In a first stage, a polymer solution or dispersion is cooled down below freezing, resulting in the formation of ice crystals, which are surrounded by polymer aggregates in the interstitial spaces. In a second stage the solvent is removed, by lowering the pressure via vacuum exposure, to a level lower than the equilibrium vapor pressure of the frozen solvent, causing it to sublimate. The sublimation of the ice crystals causes the formation of a highly porous structure, which final shape depends on process conditions like pH, freezing rate and partial pressure. An advantage of this method is the possibility to control the pore size with the cooling regime. However, it needs to be carefully controlled since a rapid uncontrolled freezing would result in non-uniform nucleation and scaffold morphological heterogeneity, while a constant cooling rate would lead to a more uniform porous structure. Among the disadvantages are the lengthy time scales, high energy consumption and the use of organic solvents<sup>28,35,36</sup>.

Another conventional method for scaffold fabrication is gas foaming (Figure 2.12c). This method was developed to avoid the use of toxic organic solvents by using relatively inert gas foaming agents like carbon dioxide and nitrogen, saturating with these gases pressurized molded biodegradable polymers. Then, the gas pressure is suddenly reduced, causing the nucleation and growth of gas bubbles and leading to the formation of pores. Among the disadvantages of this method are the difficulty in controlling pore size, the formation of closed, non-interconnected pore structures and a nonporous layer at the scaffold surface<sup>28,35,36</sup>.

In phase separation method (Figure 2.12d) a thermodynamically unstable condition is created in a multicomponent homogeneous polymer solution, leading to its spontaneous separation into two distinct phases. The most common method used to induce the instability is by a rapid change in temperature, usually cooling the solution, in a process named thermally-induced phase separation (TIPS). A polymer-rich phase and a solvent-rich phase are created. Depending on the process parameters, like polymer concentration, the presence of other solvents, quenching temperature and quenching rate, it is possible to control the macro and micro-structure of the two-phase mixture, which will determine the porosity and interconnectivity of the produced scaffold. The last step is the removal of the solvent-rich phase, usually done by freeze-drying. Hollowing the space occupied by the solvent-rich phase results in the formation of a porous polymer matrix. In terms of disadvantages, a limited range of pore size is generally attained and the use of organic solvents inhibits the use of bioactive molecules or cells<sup>28,35,36,79</sup>.

In the electrospinning technique (Figure 2.12e) a polymer solution, emulsion or melt are ejected from a spinneret under the application of a strong electric field, which results in the production of fine fibers deposited onto a collector, with diameters ranging from the small micrometer to nanometer scale<sup>35,80</sup>. The standard experimental set-up consists of four main components, namely, a syringe pump, a metallic or conductive needle of small diameter (spinneret), a high voltage power supply and a grounded collector<sup>75,80</sup>. To start the process, electric charges accumulate in a droplet at the tip of the needle, and when repulsion exceeds the surface tension a liquid jet is produced. This jet is accelerated towards the collector, with a characteristic whipping motion due to electrostatic repulsion, until the fibers

are deposited over the collector, forming a nonwoven fibrous mesh. During this process the solvent evaporates<sup>35,75,81</sup>. Through the adjustment of the method parameters related to the solution (e.g., polymer concentration, molecular weight, solvent used), process (e.g., flow rate, distance between nozzle and collector, voltage) and environmental (e.g., temperature, humidity), the fiber morphology and diameter can be tuned<sup>43,80,82</sup>. Modifications to the collector system and to the spinneret allow further tuning of the fibers. For example, a flat metal plate will lead to the deposition of random fibers, while deposition over a cylindrical mandrel rotating at high speed or using a collector composed by two parallel metal plates will result in aligned fibers. As for spinnerets, they can be designed to deliver more than one fluid, producing for example coaxial fibers, in which an inner solution (core) is enveloped by an outer solution (shell)<sup>42,80</sup>.

Several features of the electrospinning process make it very versatile and so it has consequently been extensively used in TE applications<sup>83</sup>. Considering its advantages, electrospinning is compatible with an extensive list of natural and synthetic polymers, allowing the formation of fiber meshes with a wide variety of chemical composition and properties. Another advantage is that by allowing the tuning of fiber diameter and orientation it enables the creation of structures that closely resemble the native tissue ECM while offering a high surface area that is favorable for cell attachment<sup>28,43</sup>. Another advantage is the possibility of postprocessing the surface of the fibers. Possible physical or chemical modification techniques include biological coating (e.g., coating with ECM elements), surface grafting and biomolecule immobilization (e.g. connecting cell adhesion molecules to the fibers), introduction of functional groups (e.g., changing the functional groups on the surface of the fibers, changing its properties) and functionalization with therapeutic agents (e.g., dispersing growth factors in the fibers)<sup>80</sup>. This wide variety of post processing options allows the modulation of cellular adhesion, proliferation and differentiation, granting many alternatives to adjust biological response and tissue repair<sup>80</sup>. However, some disadvantages of the electrospinning procedure can also be identified. There is poor control over scaffold architecture, with limitations in the incorporation of precise microarchitecture into constructs and in the construction of complex 3D structures<sup>75,83</sup>. Pore distribution is also non-homogenous and therefore cell penetration and migration as well as nutrient exchange and waste removal can also be hindered due to small pore sizes<sup>80</sup>. The weak mechanical properties are also a limitation, especially for load-bearing applications<sup>28,83</sup>. Lastly, the use of organic solvents may constitute a concern, namely by the presence of small remaining amounts in the scaffold, which might affect cells, compromising safety and approval by regulatory entities<sup>28,80</sup>.

#### 2.4.2. Additive manufacturing techniques

Offering the possibility of creating objects from computer generated files, AM has presented various approaches to overcome limitations of conventional techniques. Importantly, AM allows the process automation and high level of control over the fabricated constructs, guaranteeing its reproducibility and enabling scale-up and standardization. It also allows the flexibility of designing personalized constructs, important to meet patient individual needs. Moreover, together with the possibility of fine-tuning the porosity and architecture of the fabricated constructs incorporating cells and bioactive materials, AM

has become an appealing tool for TE strategies<sup>74,84,85</sup>. Figure 2.13 presents an historical overview of the development and application of AM techniques in TE.

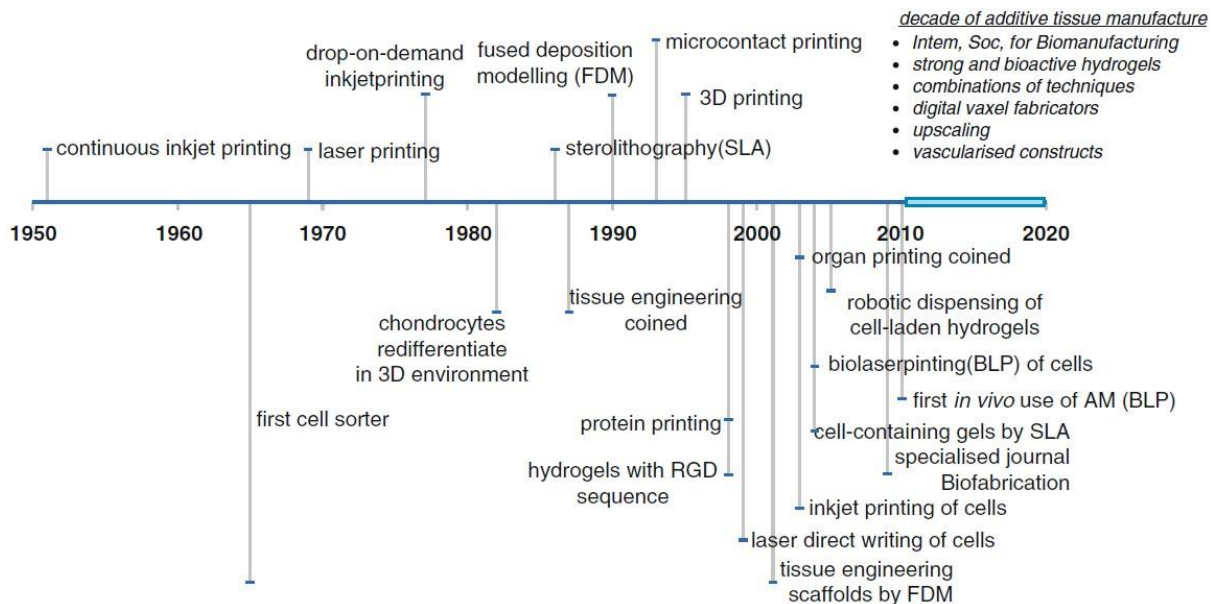


Figure 2.13 – Historical overview of important landmarks and introduction of new technologies for additive manufacturing (AM) techniques in tissue engineering (adapted from<sup>85</sup>).

Over the last decades many AM techniques have emerged, answering the needs in many research areas. Still, new practices and variations of the existing techniques are constantly under development to meet the requirements for novel scaffold fabrication in TE. This has led to some variability in denominations used by different authors and a debatable terminology to combine the different AM techniques<sup>76,86</sup>. So, there is no standardized classification<sup>86</sup> and there is an interchangeability in many designations. For example, AM can be found commonly referred to as rapid prototyping (RP) or solid free form fabrication (SFF)<sup>42,85</sup>. Nevertheless, throughout this thesis the AM terminology will be maintained.

The most commonly used AM methods used in TE strategies will be briefly described on the next subsections. It should be noted that these methods can have a broader use in the field of TE beyond OC regeneration, allowing the construction of scaffolds targeting other types of tissues<sup>74,87–89</sup>. The focus will first be in methods that allow the construction of scaffolds, onto which cells are seeded only after they have been produced, although some have also been adapted to create structures including cells. After that, the focus will be on a set of techniques that have been developed with the specific purpose of fabrication with biomaterials, cells and biomolecules, which are usually designated in the literature by 3D bioprinting<sup>82,90,91</sup>.

The main categories in which AM techniques can be grouped, excluding the specific 3D bioprinting techniques, are represented in Figure 2.14. Those categories are stereolithography (SLA), selective laser sintering (SLS), three-dimensional printing (3DP) and fused deposition modelling (FDM)<sup>35</sup>.



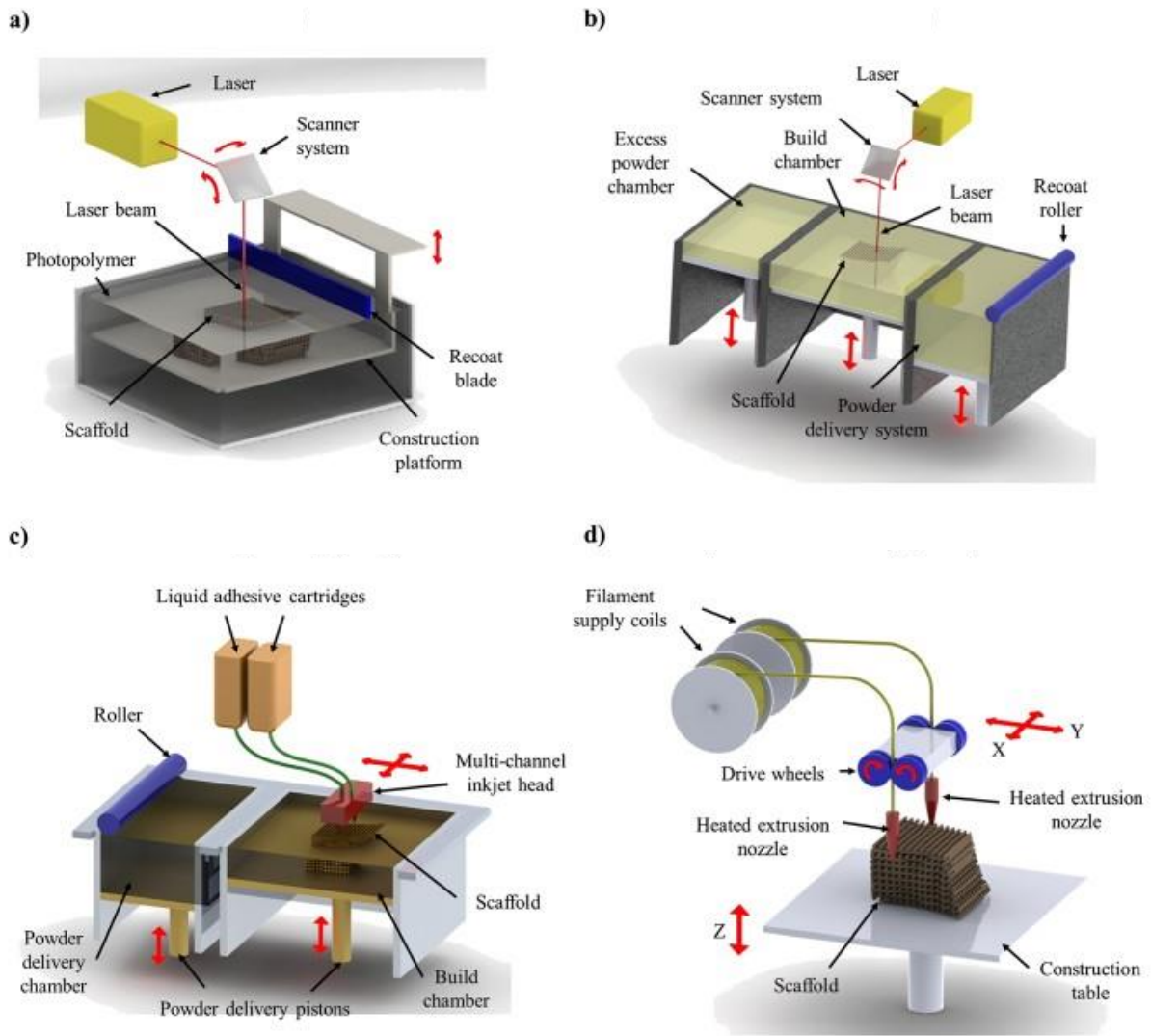


Figure 2.14 – Schematic representation of the most commonly AM techniques employed in TE: a) Stereolithography (SLA); b) Selective laser sintering (SLS); c) 3D printing (3DP); d) Fused deposition modeling (FDM) (adapted from <sup>76</sup>).

### Stereolithography

SLA is a technique that was first developed in 1986, and that uses an ultraviolet (UV) laser to selectively polymerize layers of a photosensitive polymer. This system consists of a tank of a liquid polymer, a moveable build platform, a UV laser and a scanner system<sup>76,83</sup>. There are two methods of irradiation usually employed. One uses a mask, through which a pattern is transferred to the liquid polymer by blocking or allowing the laser light to pass. The other one uses a focused beam to directly polymerize the polymer<sup>84</sup>. After the polymerization of each layer, the platform is moved a defined distance and a new layer is built on top of the previously built one, until the conclusion of construction. In order to guarantee contact between successive layers and prevent delamination, a small overlap is established between the layers. The final steps include the removal of non-polymerized material and post-curing to fully polymerize the object<sup>76,83</sup>.

The first polymers developed for SLA were resins based on low molecular weight polyacrylate and epoxy monomers, which generally required toxic solvents, and generated predominately rigid and brittle

materials<sup>76,83,92</sup>. This restricted its application in TE due to non-biocompatibility and non-biodegradability issues<sup>76,86</sup>. To overcome these issues, the first attempts used SLA to produce scaffolds in an indirect way. In one approach HAp powder was mixed with the resin before the curing process. Then, by a heating process, the resin was removed leaving behind a porous HAp structure. In another approach, an epoxy mold would be cast, and a suspension would fill the empty space. After a thermal treatment to remove the mold, a scaffold with the inverse shape would be formed<sup>76,83</sup>. More recently, new photocurable polymers with more suitable properties for scaffold production have been developed, being biocompatible and biodegradable, mostly due to the presence of ester or carbonate bonds on the polymer backbone, which enables hydrolysis and facilitates biodegradability. Commonly used polymers in SLA to create biodegradable structures include poly(propylene fumarate) (PPF), trimethylene carbonate (TMC), PCL, and poly(D,L-lactide) (PDLLA), which have been functionalized to allow the photopolymerization process<sup>76,83,93</sup>. Resulting in the fabrication of rigid structures, these resins are more applicable for engineering bone or other hard tissues<sup>93</sup>. To take advantage of its biocompatibility as a supporting structure for 3D cell culturing, photocrosslinkable hydrogels have also been created for fabrication through SLA. As examples, poly(ethylene oxide) (PEO), poly(ethylene glycol) dimethacrylate or gelatin methacrylate (GelMA) constitute some of the most used materials. Cells have also been incorporated in these hydrogels prior fabrication by SLA, and their viability shown in *in vitro* culture experiments<sup>76,83,94</sup>.

Comparing with other AM methods, SLA shows a remarkably high quality in prints, accuracy and reproducibility between prints as well as a higher resolution in relation to other AM methods. However, drawbacks like shrinkage of the constructed scaffold, the necessity of accessory support structures for the fabrication of complex geometries, the limitation of having the constructs made of a single material and the shortage in the available materials, are commonly referred<sup>76,83,84,93,94</sup>.

### *Selective laser sintering*

SLS is a technique that was developed and patented by Deckard et.al. in 1989 and is based on sintering, or fusing, of selected regions of a material powder, using a high intensity laser beam (commonly CO<sub>2</sub>). After the generation of a layer, the bed is lowered, and the next layer of material is deposited on top of the previous one by a mechanical roller. This process is then repeated until the full completion of the 3D object. In the case of SLS, temporary support structures are not needed, since the non-sintered material acts as support for subsequent layers<sup>76,83,95</sup>. By adjusting the process parameters, such as manufacturing direction, scan spacing, scan speed, layer thickness, laser intensity and size of particles, it is possible to control the morphology, mechanical properties and size accuracy of the scaffolds<sup>76,96,97</sup>. This effect can be understood by considering for how long and the intensity with which the material interacts with the laser. The greater the energy transferred, a greater fusion of the material would occur, resulting in denser and less porous constructs, greater adhesion and increased mechanical strength. Smaller layer thickness and overlapping between laser scans have the same effect, again due to increased interaction between the powder and the laser and stronger bonding between layers. Conversely, faster laser scans, lower intensity, smaller overlap between laser scans and greater layer heights can lead to more porous constructs with weaker mechanical properties<sup>86,96</sup>. Particle size is

usually in the range of 10–150  $\mu\text{m}$  and its choice affects pore size, resulting in a powdery rough surface finish of the scaffolds<sup>83,86,98</sup>.

SLS can be used to produce TE constructs from materials like metals, bioceramics, polymers and their composites, in particular very frequently from polymer/bioceramic composites<sup>83,86,98</sup>. Materials like PCL, PLLA, poly(hydroxybutyrate-co-hydroxyvalerate) (PHBV) and polyetheretherketone (PEEK) polymers, and the bioceramics HAp and TCP are among the most used ones in research studies<sup>86,98</sup>. Using these materials, the SLS technique has more generally aimed at the production of scaffolds for bone TE<sup>76</sup>.

One advantage of SLS over other AM techniques is that it is a solvent free process<sup>83</sup>. However, some disadvantages are identified compared with other fabrication techniques such as limitations in biomaterials availability in the form of fine powders suitable for SLS, the difficulty of removing entrapped material inside complex geometries, and the use of high temperatures, which make the incorporation of cells or biomolecules inaccessible<sup>76,83,98</sup>.

### *3D printing*

3DP was originally developed at the Massachusetts Institute of Technology in the beginning of the 1990s and is based on a selective deposition of droplets of a binder material over a powder bed, using an inkjet head, merging the particles together and forming a solid layer. After deposition, the build platform is lowered and a new layer of powder is placed over the previous one, and the entire process repeated until a 3D object is built. The powder that remains unbound functions as support for the material in the ensuing layers. The loose powder is separated in the end, revealing the formed object<sup>76,78,83,95</sup>. Sintering processes are sometimes used in a post processing stage, to improve the mechanical properties of the construct. In those situations construct shrinkage is mentioned limiting the use of incorporated biomolecules<sup>86</sup>.

Scaffold characteristics can be adjusted controlling process properties such as powder size, size distribution, roughness, shape, wettability as well as the chemical reactions between the powder and the binder. In the case of particles, a spherical shape and a size between 20 and 35  $\mu\text{m}$  are recommended. As for the binder, the amount of its penetration and spread will affect the mechanical properties and create a limitation in detail and tolerance in the design of the parts<sup>75,86</sup>. Therefore, resolutions under 50  $\mu\text{m}$  should not be attainable in 3DP<sup>81,83</sup>. Other characteristic aspects of 3DP, because it consists of binding particles, are the powdery rough finish of the parts and the difficulty in removing trapped material in complex geometries<sup>76,83</sup>. Another drawback is the lack of adhesion between layers, when compared to SLA, SLS and FDM<sup>83,99</sup>.

A wide range of materials and binders are available at low cost and suitable for processing with 3DP. However, requirements in biocompatibility, biodegradability, toxicity and mechanical strength have limited the actual number of materials used, with polymers, ceramics and composites being the most widely studied<sup>81,86</sup>. Among the most described materials are the bioceramics HAp and TCP and the biocompatible synthetic polymers PLLA and PLGA<sup>83,86</sup>. Natural polymers have also been tested (e.g., cornstarch, dextran and gelatin as powder and distilled water as a binder), but showed poor structural integrity and mechanical properties<sup>73,86</sup>. As this method does not require heat, it allows the incorporation

of bioactive molecules in the process<sup>83,86,95</sup>. In the situation when polymer powders are used with organic solvents as binders, biocompatibility issues need to be considered, as well as adapting the printhead to withstand these solvents<sup>86</sup>.

### *Fused deposition modeling*

FDM, also known as fused filament fabrication (FFF), is a technique originally developed in 1992 for the fabrication of prototypes for industry, and is based on the extrusion of a polymeric filament through a heated nozzle<sup>76,90</sup>. The filament is fed to the nozzle by drive wheels or gears, where it is melted and deposited over a construction platform. The nozzle moves in the xy plane, depositing the filament in a predetermined pattern. When the material leaves the nozzle, it cools and solidifies, bonding to the already laid structure. After the completion of each layer, the platform moves in the z direction and the deposition process is repeated, over the previous layer, until a 3D object is created<sup>76,83</sup>. If the object being printed has overhangs or island features, a temporary support structure is required, which can be removed after the print is finished. The support material can be the same or a different material than the one used for the constructed part and both can be fed through the same or through different nozzles, as is the case in more recent systems, which can have dedicated nozzles for each filament<sup>76,83,100,101</sup>.

Due to FDM fabrication characteristics, the range of available materials remains limited. These materials must possess attributes as being thermoplastic, having a suitable viscoelasticity, being able to melt and solidify while having the ability to be processed into filaments<sup>86</sup>. However, because of the heating needed for creating a molten phase and the shear forces in the nozzle, this technology is not suited for printing with biological materials<sup>78,81,90</sup>. Among the most commonly referred polymeric materials used in FDM are PCL, PLA, PLLA, PEG and PLGA<sup>81,90,102</sup>. Because of the process characteristics, however, this method cannot handle pure bioceramics, and so, to bypass this problem, these bioceramics (e.g., HAp and TCP) are incorporated with the polymer base, as composite materials<sup>35</sup>. In addition, when comparing FDM with other AM techniques, the rapid low-cost printing capacity without the use of organic solvents and the ability to produce constructs with mechanical resistance similar to OC tissues are important advantages. On the other hand, the relatively poor resolution, not inferior to 100  $\mu\text{m}$ , is often viewed as a disadvantage<sup>83,90</sup>.

There are presently three main material extrusion methods used in AM to fabricate scaffolds for TE, which are represented in Figure 2.15. The majority of commercially available printers use some of these technologies<sup>103</sup>. The filament-fed systems are the most common, due to the low hardware costs and to the possibility of setting the melt chamber in a wide range of melting temperatures. Nevertheless, it is limited to synthetic polymers that can be purchased in filament form, typically with diameters of 1.75 mm or 2.85 mm. The dimension of the extruded filament can be controlled by the nozzle size and by the software-controlled speeds at which the filament is fed and at which the nozzle is moving<sup>103</sup>. In screw assisted systems, the polymer material is fed into a heated barrel in the form of granules or, less commonly, in paste form. The rate of material extrusion through the nozzle is controlled by the screw rotation speed. The increase in hardware complexity makes it more costly when compared to filament systems<sup>103</sup>. In syringe-based systems, the material is placed inside a syringe and its deposition is

controlled by the speed at which a plunger extrudes a filament<sup>103</sup>. Typically, viscous materials like hydrogels are used with this system, although polymer granules may also be used if the syringe has a heating jacket<sup>84,91,103</sup>. Two main alternatives are present to control the plunger, which are applying pneumatic pressure or controlling the plunger speed with an electrical motor. The electrical motor allows a more precise control over the extrusion rate, while with pneumatic control the forces exerted on the materials are known, which is relevant when materials sensitive to shear forces are being used. In pneumatic systems, the control over extrusion rate is less precise, due to the interaction between needle geometry, material viscosity, actual applied pressure and possible obstructions<sup>103</sup>. It is possible, in any of these systems, to include more than one extruder so that by alternate material deposition, multiple materials can be combined to fabricate multi-material constructs with structural properties closer to the ones of native tissues<sup>84,103</sup>.

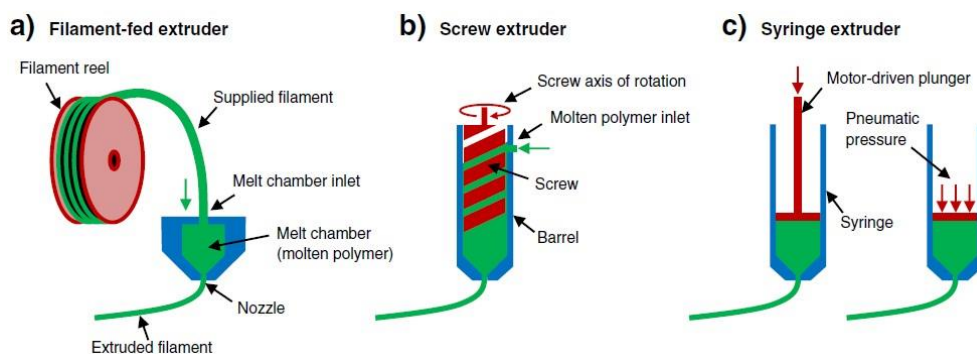


Figure 2.15 – Schematic illustration of different types of extrusion: a) Filament-fed extruder; b) Screw extruder; c) Syringe extruders with either a mechanically driven plunger or pneumatic pressure plunger (adapted from <sup>103</sup>).

In terms of software for AM technologies, a wide variety of different ones can be found. Filament-fed systems for general applications typically use software focused on achieving high quality covering a large variety of geometries and sizes. They provide options to control many printing parameters, generally aiming for faster prints, minimizing material usage but maintaining structural strength. However, control over individual filaments is not usually possible. Conversely, software supplied with bioprinters, due to requirements from clinical applications, can have a focus on micro-scale geometry and allow precise control over filament deposition<sup>103</sup>. For some specialized purposes, researchers may even develop custom software to generate print paths, and automatically obtain specific features, for example related to controlling filament orientations and multi-material printing<sup>104,105</sup>. Some limitations may however apply, depending on the acceptance of third party code by any particular system<sup>103</sup>.

The pattern with which the filaments are laid can also have a significant role in the properties and performance of the scaffolds. By changing the filament orientation in each layer, a wide range of distinct geometries can be constructed, as previously reported in the literature<sup>103</sup>. Figure 2.16 shows methods to obtain different geometries, either by changing the filament orientation in successive layers (Figure 2.16a) or by offsetting layers with the same orientation (Figure 2.16b). In terms of orientation, it is most common to have filaments aligned perpendicularly in successive layers. Alternatively, rotations creating regular patterns, like 45° or 60°, have also been described<sup>103</sup>. In terms of layer offset, usually the filaments are aligned directly above filaments with the same orientation in different layers. Alternatively, they can be found offset a distance corresponding to half the pore dimension between each successive

horizontal layers<sup>103,106</sup>. Layer can also be found repeated, when identical layers are printed on top of each other, before a change in their orientation<sup>103</sup>.

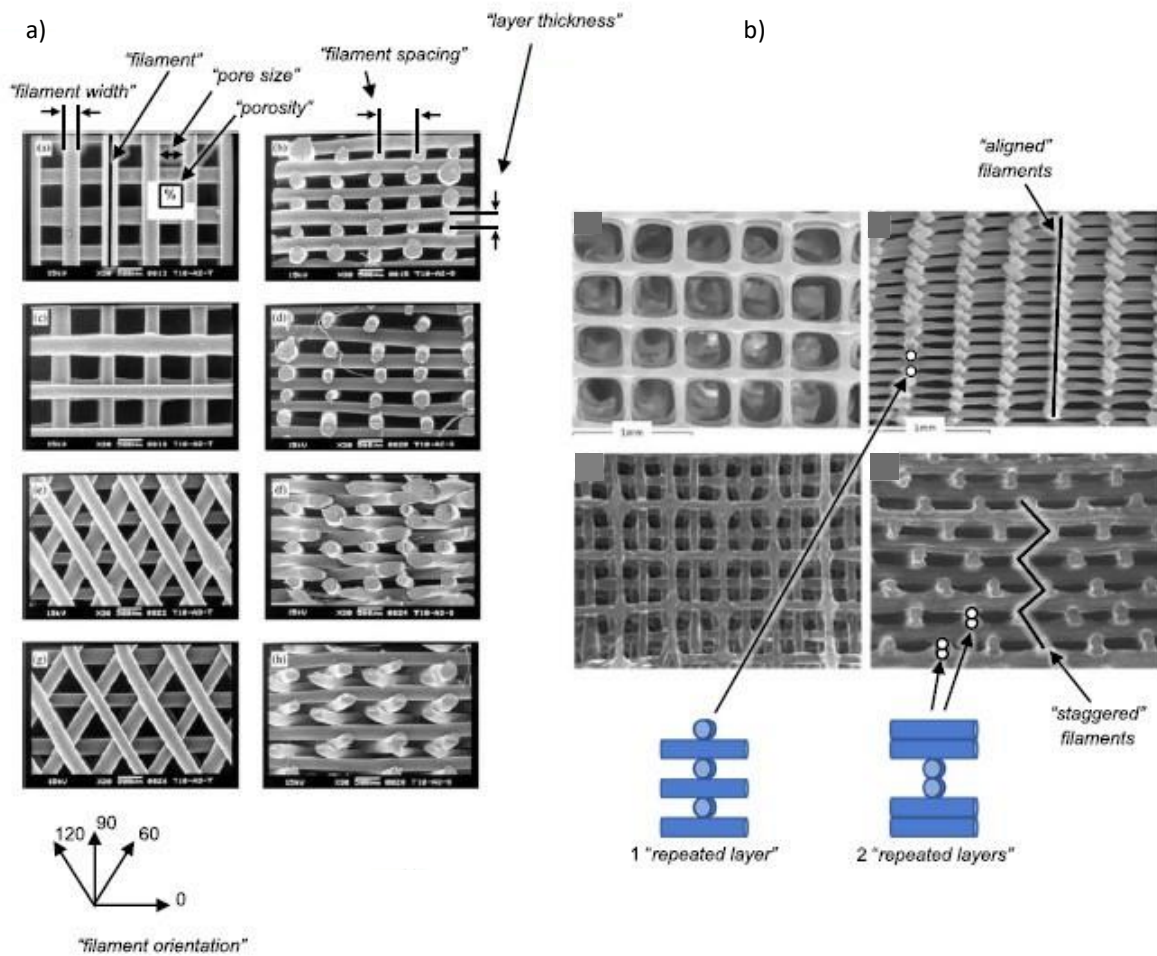


Figure 2.16 – Printing strategies with different filament positions and orientations: a) Changing filament orientation; b) Offsetting layers with the same orientation (adapted from<sup>103</sup>).

The abovementioned varied geometries can impact some important scaffold characteristics. Depending on geometry, pore interconnection may have more resemblance with intersecting columns or with spiraling structures affecting nutrient and oxygen transfer through the scaffold<sup>103</sup>. Considering the mechanical resistance, one trend has been identified both for offset and rotated layers. In the cases where solid profile columns of material are found, a larger mechanical resistance along the direction of compression is noticed due to the resistance of the continuous solid material. In contrast, in the absence of those columns, scaffolds tend to fold, concentrating stress at the hinge points<sup>103</sup>. Considering the case of having layer repetition, results are contradictory, with studies reporting no variation and others a decrease in resistance<sup>103</sup>. The effect of geometric variations on cell seeding and proliferation has also been reported in the literature and results vary considerably, with some studies reporting improved cell attachment in more tortuous scaffolds and other studies not finding significant difference or finding improved proliferation in the typical 0°/90° orientation. These results imply that a more profound knowledge about the effects of scaffold geometry/architecture on cell adhesion and proliferation and long term tissue formation are still required<sup>103</sup>.



### 3D bioprinting

Recently distinguished in the literature, 3D bioprinting consists in a set of techniques allowing the creation of 3D structures with user defined patterns, simultaneously depositing living cells and other biomolecules within the hydrogel material<sup>91,98</sup>. These deposited materials containing living cells, generally dispersed on aqueous or hydrogel formulations are commonly designated as bioinks<sup>107,108</sup>. The most used methods for bioprinting include inkjet, laser-assisted and extrusion, and are illustrated in Figure 2.17<sup>35,75,82,98,109</sup>. Table 2.3 presents a comparison between the features of these different bioprinting strategies.

In order to be suited for bioprinting, a bioink should possess some characteristics beyond supporting cell viability. It should be extrudable in a controlled fashion, generating cylindrical shapes or rigid droplets, it should demonstrate shear thinning behavior (flow under an applied force but retain shape under no loading), and able to be cross-linked or self-assembled to prevent dissolution and maintain shape when deposited in layers<sup>110</sup>. Bioinks have been mainly derived from natural biomaterials (e.g., alginate, collagen, gelatin) using convenient approaches to give them the shear thinning flow characteristics. Popular choices have been the use of thickening agents, bioink printing thermoregulation (for example, maintaining gelatin in the thermal transition region: if it is too warm it will not retain shape after printing while if it is too cold it will extrude at higher pressures, unevenly and will have a poorer layer adhesion), and printing the bioink in a shear thinning support medium, a method designated as freeform reversible embedding of suspended hydrogels (FRESH)<sup>110</sup>. The cross-linking methodologies commonly explored can be grouped by their mechanism. Cross-linking can be achieved by the addition of an ionic solution (e.g., calcium solution) in a process that is often reversible. It can be achieved through a light source, either UV or visible, a popular approach for being fast and flexible, but is often irreversible because it uses a catalyst to bind molecules together. Cross-linking can also be achieved through enzymatic activity, taking advantage of natural biological processes. Finally, it can also be achieved by self-assembly, in processes controlled by environmental factors like temperature, pH or biomolecule concentration, and examples include thermosensitive assembly of gelatin or self-assembly of collagen fibers<sup>110</sup>.

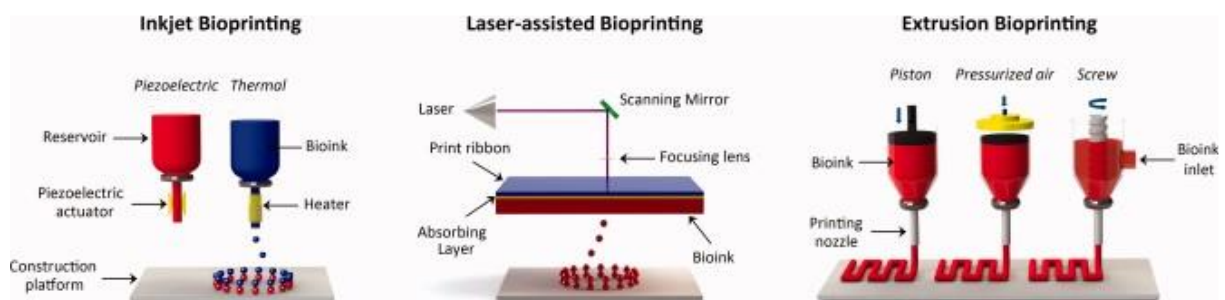


Figure 2.17 – Illustration of 3D bioprinting technologies based on the mechanism used to assist the deposition of the bioinks and its main components (adapted from <sup>82</sup>).

Inkjet bioprinting is based on conventional inkjet printers, which have been adapted to create 3D biological constructs. It is a noncontact technique where droplets of a bioink are jetted onto a build platform in a predefined pattern by means of a pressure change created by an actuator<sup>74,75</sup>. After

deposition, the materials are then polymerized by UV light, chemical, ionic, or enzymatic crosslinking<sup>90,91</sup>. The two most common forms of actuation are thermal and piezoelectric<sup>87,89</sup>. With a thermal actuator, a pressure pulse is created by localized heating pulses, forcing the bioink out through a nozzle. With the piezoelectric actuator, a voltage is applied to a piezoelectric material, causing a volumetric change and a pressure pulse<sup>89,98</sup>. Inkjet bioprinting is compatible with a wide range of biomaterials, such as sodium alginate, poly(ethylene glycol) dimethacrylate (PEGDMA), fibrin-based hydrogels, calcium phosphate, and HAp<sup>91</sup>. The main advantages of inkjet bioprinting include its low cost, the use of already available components, high printing speeds with tissue compatible resolutions, and the possibility of controlling concentration gradients in the printed constructs<sup>74,91,109</sup>. The disadvantages include the limited range in printable viscosities that only allow low cell densities, being limited to ejection of liquid phase materials, droplet irregularity and directionality, nozzle clogging in the thermal actuation, and the risk of cell death in high-frequency actuation when using the piezoelectric system<sup>74,89,91</sup>.

Laser-assisted bioprinting was developed from laser-induced forward transfer, a method to pattern metals and inorganic materials onto a substrate<sup>89,91,109</sup>, which has been successfully applied to peptides, DNA and cells<sup>74,87</sup>. This system can be divided into four parts, which are a pulsed laser source, a laser focusing tool, a ribbon structure composed of a laser absorbing metallic ribbon on top and a layer of bioink solution suspended on the bottom, and a receiving substrate<sup>89,109</sup>. During printing, laser pulses are directed to the metal layer of the ribbon, producing a high pressure bubble, which in turn leads to the ejection of the bioink towards the receiving substrate<sup>75,89,91,111,112</sup>. The main advantages reported about this technique are the high cell viability since the shear stress cell damage is eliminated; the high resolution allowing printing close to single cell per droplet; the capacity of accommodating high cell densities, and of being suited to low material viscosities. The main disadvantages include a relatively small range of printing viscosities; the limitation in gelation methods available; the fact that it is limited to produce thin structures; the possible adverse effects on biological material of metallic residues resultant from the laser exposure, and the complexity and cost of the method<sup>74,89,91,98,109</sup>.

Extrusion bioprinting presently corresponds to the most commonly used method in bioprinting. A material is extruded in a continuous fashion, rather than in droplets as in inkjet printing, in a process similar to FDM. During bioprinting, pressure can be applied by piston, pneumatic, or screw driven systems, with this last method being the most suited for high viscosity bioinks<sup>98,107</sup>. Important for this method is the flow behavior of these materials, which should exhibit shear-thinning properties. These materials are viscous when no shear stress is applied and flow easily under high shear rates, like through the narrow extrusion nozzles<sup>91</sup>. To enable the cross-linking reactions and to stabilize the produced constructs, the extruded bioinks can be modified with appropriate functional groups<sup>107</sup>. Considering the advantages relative to the other methods, extrusion bioprinting has the ability to print high viscosity materials and higher cell densities, making possible to generate constructs comparable to the native tissues, and has more available polymerization mechanisms. Considering the disadvantages, there may be limitations in maintaining high cell viabilities, especially with high viscosity materials, and having at the same time high resolution and print speed. Better resolutions require narrower nozzles, where higher shear rates would be noticed. Additionally, the possibility of nozzle clogging should be considered, particularly for higher viscosity materials<sup>91,109</sup>.



Table 2.3 – Comparison of common 3D bioprinting strategies (adapted from <sup>91,98,109,113</sup>).

	<b>Inkjet</b>	<b>Laser-assisted</b>	<b>Extrusion</b>
Droplet size	<1 pL to >300 pL drops (50-300 µm wide)	>20 to 80 µm	5 µm to >1 mm
Spatial resolution	Medium	Medium to high	Low to High
Quality of vertical structure	Poor	Fair	Good
Material viscosity	3.5 to 12 mPa s	1 to 300 mPa s	30 mPa s to >600 kPa s
Gelation method	Ionic, enzymatic, photo-crosslinking, thermal, chemical	Ionic, chemical, photo-crosslinking	Chemical, ionic, enzymatic, photo-crosslinking, shear thinning, thermal, pH
Gelation speed	High	High	Medium
Cell viability	>85%	>95%	40 to 80%
Cell density	Low, <10 <sup>6</sup> cells mL <sup>-1</sup>	Medium, <10 <sup>8</sup> cells mL <sup>-1</sup>	High, cell spheroids
Encapsulation control	Low	Medium to high	Medium
Preparation time	Low	Medium to high	Low to medium
Print speed	Fast	Medium to fast	Slow
Throughput	High	Low to medium	Medium
Cost	Low	High	Moderate
Reported applications	Tissue engineering (Blood vessel, bone, cartilage, neuron, cardiac, skin)	Tissue engineering (Blood vessel, bone, skin, cardiac, adipose)	Tissue engineering (Blood vessel, bone, cartilage, neuron, cardiac, skeletal muscle, liver, skin, tumor) Controlled release of biomacromolecules Organ-on-a-chip
Representative materials for bioinks	Alginate, PEGDMA, collagen	Collagen, Matrigel	Alginate, GelMA, collagen

## 2.5. Computational modeling in tissue engineering

One aim of TE is the culture of living cells within devices and scaffolds that create a growth environment mimicking the native tissue as closely as possible. In that regard, some key aspects have been identified as of major relevance: the interactions of cells with the surrounding ECM and other cells, in which ECM modulates cell proliferation, differentiation, and metabolic functions; and the influence of environmental factors such as mechanical (e.g., flow-induced effects), electrical and biochemical stimuli. As a complement to the *in vitro* experimental research on the influence of these aspects, the use of detailed mathematical models as a virtual *in silico* representation of the tissues/scaffolds/bioreactors can be advantageous. These models are designated digital twins and are developed with the objective

of providing a more profound characterization of the culture systems/scaffolds as well as optimizing stimulation parameters and predicting experimental outcomes while reducing the time and costs involved<sup>114</sup>.

Digital twins can be thought of as “digital replications of living as well as non-living entities that enable data to be seamlessly transmitted between the physical and virtual worlds,” and it has found remarkable applications outside the field of TE, for example in industries developing electronics, aircraft and automobile design, and energy production. The digital twin concept provides the engineering community with a way to handle increasing complexity in the design, manufacturing, control and maintenance of objects, systems, and processes. In recent years, a major obstacle to the widespread implementation of digital twins is being overcome with the increase in computational power, enabling the study of progressively more complex processes<sup>114,115</sup>.

Digital twins can be seen as an engineering strategy with the following advantages in TE: i) linking physical laws and process parameters describing an experiment in a computational system, ii) allow the increase in knowledge about that experiment through an iterative fine tuning process; iii) allow a decrease in development costs for experimental design; iv) is compliant with the development of patient personalized solutions; v) facilitates the integration of acquired knowledge and improvements to the digital twin during the lifecycle of a product; vi) make possible the evaluation, screening, and virtual testing of new configuration and settings prior to experiments<sup>114</sup>.

One way to classify digital tools is according to the modelling method supporting the model. Mechanistic models are developed based on concepts and hypothesis informed by biological knowledge and insight, with its parameters having a physical meaning. However, they may have a higher cost of development, be more difficult to parametrize, and be generally harder to compute in real-time, which can frequently be a requirement for digital twins. Additionally, if the complexity of the biological processes is too high, or the understanding of the process is too limited, a fully mechanistic model will not be achievable. Conversely, data driven models are developed only with experimentally generated evidence. Due to this black-box nature, they provide less insights into the system, and are more straightforward to develop. In situations where data-logging is faster than its analysis, they provide a good basis for prediction and control. Nevertheless, there might be some reluctance in using these models in clinical settings, as results from data-driven models can often not be extrapolated to cases outside the scope of the training data. Alternatively, hybrid strategies combining both models could provide a more capable framework<sup>115</sup>.

To conclude, revealing of its widespread use in TE, the following tasks have already been addressed with digital twin modeling: cell growth, morphology, heterogeneity, dynamics; cell kinetics; systems biology; cell handling, seeding, culture conditions; cell penetration, fluid permeation, diffusion; scaffolds-fluid flow, shear stress, mass transfer; bioreactor-fluid flow, mass transfer; mechanical stimulation; image-based modeling; tissue specific effects; pharmacology; handling of models; model-assisted experimental design<sup>114</sup>. As particular examples, a study by Meneses et.al.<sup>116</sup> modeled the mechanical and electrical stimulation in a bioreactor system, and a study by Xue et.al.<sup>117</sup> compared, through FEA, the flow velocity, fluid shear stress and media mixing in a CAD model and a micro-CT reconstruction of a scaffold for coculture of AC and bone.

## 3. Materials and Methods

### 3.1. Modeling software and manufacturing device

Models were created in Autodesk Fusion 360 student edition (version up to 2.0.11415, on-line automatically updated) computer-aided design (CAD) software. Designs were made parametrically, which means that the model is constructed using a set of built-in geometric operations in the software, and that variables can be used to assign dimensions to the model. In this parametric environment, there is only a virtual representation of the models, which means that changes can be made quickly by simply assigning new values to the parameters, with the software rebuilding the entire model. To create 3D objects, models were exported from Fusion 360 as stereolithography (STL) files. This process takes the model and creates a triangle mesh, which level of detail can be controlled, covering the surface of enclosed volumes, but losing all information concerning the steps to build the model. With the created STL file, the quick model modifications can no longer be made due to limitations of this format.

When editing of 3D STL files was necessary, Autodesk Netfabb Premium 2020 was used. This software is more suited for operations involving orienting, cutting, adding, and subtracting STL objects than modeling softwares like Fusion 360. STL editing was necessary when manipulating a 3D reconstruction of a human femur.

In this thesis project, all FDM 3D printing was done in a Prusa i3 MK3S commercial 3D printer (Prusa Research, Praha, Czech Republic). One modification was made to the stock printer, which was the replacement of the standard 0.4 mm nozzle by a 0.25 mm nozzle (Prusa Research), to allow greater definition in the printed parts. This change occurred during the execution of this work, so the earlier prints were done with the 0.4 mm nozzle.

Materials for this printer come in spools of filament with 1.75 mm diameter. In this work the following materials were used: flexible filament from MakerBot (PCL, estimated density of  $1.12 \text{ g/cm}^3$  <sup>118</sup>), electrically conductive PLA from Protopasta ( $1.24 \text{ g/cm}^3$ ), and generic PLA from Velleman ( $1.24 \text{ g/cm}^3$ ).

In FDM, objects are printed layer by layer. To create the G-code file that contains the machine-readable information to print each object, the slicer software PrusaSlicer (Prusa Research) was used. Briefly, STL objects were imported into the software, the intended number of copies was set, all placed with the appropriate location and orientation on the print bed, and the convenient profile settings were chosen for the model being printed. The exported G-code file contains all the information for the printer to create an object according to the defined settings.

### 3.2. Model fabrication profiles

A profile is a set of parameters used to configure how the slicer software creates the G-code. In PrusaSlicer they are grouped into three categories: print settings relate to controlling the quality and choosing the features of the objects being printed; filament settings concerning characteristics more specific to tuning how each filament is used in the printer; printer settings controlling the characteristics and limits of operation of the printer hardware. Currently, printer manufacturers already provide pre-tuned profiles that can generally produce good quality prints for a wide range of objects, bypassing the

need for the user to tune the hundreds of existing parameters. Therefore, in this work, the profiles used or created were based on existing profiles, but slightly changed when required, to improve print quality.

Concerning print settings, the “0.15 mm QUALITY” profile was the one used and adapted. Concerning the filament settings, two profiles were used, one for PLA and another for PCL. For PLA, the default “Prusament PLA” profile was used. For PCL, a new profile had to be created, since this filament does not exist in the software database. The “Prusament PLA” profile was used as template and the following parameters were changed: filament density to 1.12 g/cm<sup>3</sup>; first layer nozzle temperature to 95 °C; other layers nozzle temperature to 90 °C; first layer bed temperature to 40 °C; other layers bed temperature to 40 °C; full fan speed at layer 1. Concerning the printer settings, the “Original Prusa i3 MK3S & MK3S+ 0.25 nozzle” profile was used, when printing with PLA. To print with PCL, a new profile needed to be created since the printer has a firmware protection to prevent extrusion below 180 °C. The new profile was the same as for PLA, only with a difference in the Start G-code, where an M302 instruction was added (Figure 3.1).

```
M862.3 P "[printer_model]" ; printer model check
M862.1 P[nozzle_diameter] ; nozzle diameter check
M115 U3.9.3 ; tell printer latest fw version
G90 ; use absolute coordinates
M83 ; extruder relative mode
M302 S75 ; Allow low temperature extrusion
M104 S[first_layer_temperature] ; set extruder temp
M140 S[first_layer_bed_temperature] ; set bed temp
M190 S[first_layer_bed_temperature] ; wait for bed temp
M109 S[first_layer_temperature] ; wait for extruder temp
G28 W ; home all without mesh bed level
G80 ; mesh bed leveling
G1 Y-3.0 F1000.0 ; go outside print area
G92 E0.0
G1 X60.0 E8.0 F700.0 ; intro line
G1 X100.0 E12.5 F700.0 ; intro line
G92 E0.0
M221 S{if layer_height<0.075}100{else}95{endif}

; Don't change E value below. Excessive value can damage the printer.
{if print_settings_id=~/*@0.25 nozzle MK3.*}/M907 E430 ; set extruder motor current{endif}
```

*Figure 3.1 – Start G-code of the printer profile created to allow printing at low temperatures with PCL filament.*

When printing with PCL a further adjustment was considered beneficial because quicker movements of the printhead tended to drag and displace recently deposited filament, distorting the object being printed. To minimize this problem, whenever an object was printed with PCL, the printing speed was reduced to 50 %, an adjustment made by turning the knob in the printer console (for that reason, this information will not be found in the file G-code).

Since many parameters can be configured to fine tune a print, not all objects were printed with the same exact profile. Whenever that was the case, the changes made in relation to these default profiles will be pointed out in this thesis. Having access to the G-code files, the complete profile configuration can also be retrieved. It is written at the end of the file G-code files and PrusaSlicer provides an option to import it automatically.

### 3.3. PEDOT:PSS coated PCL films manufacturing and characterization

One of the objectives of this work was the production of new electroconductive coating formulations to coat PCL to allow the ES of cells seeded on 3D-printed PCL scaffolds. In the following subsections, the protocols used for the fabrication and characterization of such scaffolds will be described. Given that most techniques selected for the coating characterization cannot be accomplished with scaffolds, they were done with the material manufactured in the form of a film.

#### 3.3.1. PCL films manufacturing

PCL (Makerbot) films with a parallelepipedal shape (20 mm × 10 mm × 1 mm) were designed in Fusion 360 and fabricated by FDM in a Prusa i3 MK3S commercial 3D printer.

The techniques required for the film characterization provide better results on smoother surfaces. With the 3D printer used in this work, the smoothest surface that can be obtained is the first layer printed against the build plate. So, the characterization assays would be done on materials deposited over that surface. In order to increase the smoothness of the first layer, the following modifications were made to the default printing profile, only for the first layer: 0.15 mm extrusion width instead of 0.25 mm; 2 perimeters instead of 3; 100 % infill/perimeter overlap instead of 25 %; 1.2 extrusion multiplier instead of 1. Figure 3.2 shows a representative detail of the first layer.

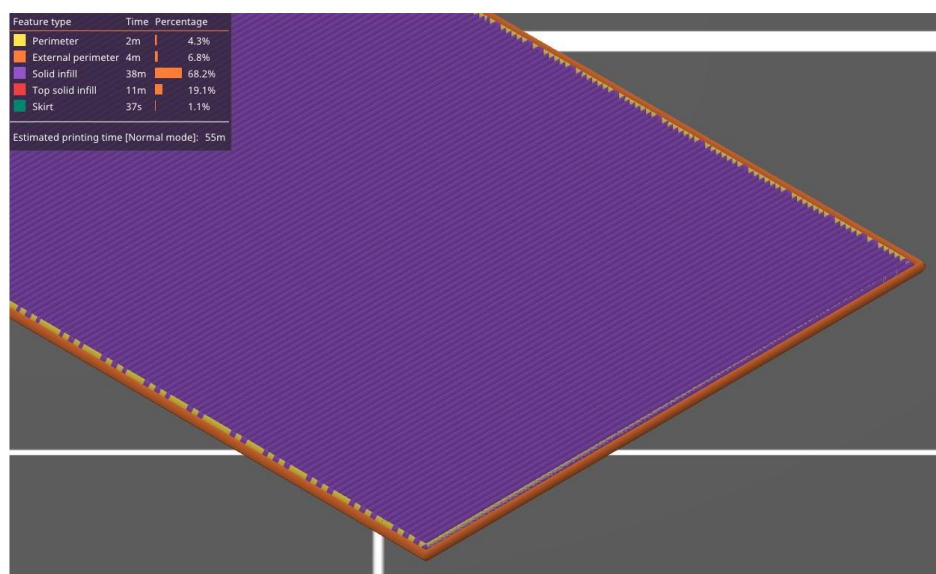


Figure 3.2 – Detail of the sliced first layer of the 3D printed films. To increase the smoothness of this layer, the following parameters were changed in relation to the default profile: 0.15 mm extrusion width; 2 perimeters; 100 % infill/perimeter overlap; 1.2 extrusion multiplier.

#### 3.3.2. Coating and crosslinking protocol

PCL has an hydrophobic nature which can impair cell attachment and compromise the success of TE strategies<sup>119</sup>. To enhance its hydrophilicity, an alkaline treatment was employed to increase the number of hydroxyl and carboxyl hydrophilic groups on the material surface. PCL films were fully immersed in a 1 M sodium hydroxide (NaOH, Sigma) aqueous solution for 24 h. After exposure, the

films were rinsed three times with distilled water to ensure the finalization of the treatment and let to dry overnight at 37°C.

Three strategies were followed for the coating of PCL films with the objective of improving their electroconductivity. These strategies were applied to pristine PCL films and to films subjected to alkaline treatment (denominated PCL(NaOH)). In one strategy, only the PEDOT:PSS dispersion was used, and in the others, two distinct crosslinkers were used to improve the structural stability of the PEDOT:PSS dispersions coating the PCL films, according to the following protocols:

i) PEDOT:PSS dispersion (Clevios PH 1000, Heraeus Holding GmbH);

ii) PEDOT:PSS+GOPS dispersion, adding the dopants ethylene glycol (EG) (1:4 volume parts, Sigma-Aldrich), dodecylbenzenesulfonic acid (DBSA) ( $0.5 \mu\text{L mL}^{-1}$ , Sigma-Aldrich) and (3-glycidyloxypropyl)trimethoxysilane (GOPS) ( $10 \mu\text{L mL}^{-1}$ , Sigma-Aldrich);

iii) PEDOT:PSS+GOPS dispersion, adding the dopants ethylene glycol (EG) (1:4 volume parts, Sigma-Aldrich), dodecylbenzenesulfonic acid (DBSA) ( $0.5 \mu\text{L mL}^{-1}$ , Sigma-Aldrich) and divinyl sulfone (DVS) ( $30 \mu\text{L mL}^{-1}$ , Sigma-Aldrich).

Films were fully immersed in these dispersions for 24 h at room temperature. Then, excess dispersion solution was absorbed from the surface of the films with paper towels and the remaining allowed to anneal for 24 h at 55°C.

### 3.3.3. Coating stability assay

To determine the coating stability, coated films were submerged in phosphate-buffered saline (PBS, Gibco) and placed in an incubator at 37°C and 5% CO<sub>2</sub>. At the established time points (0, 1, 7, 14, and 21 days) films were collected and washed three times with distilled water and let to dry overnight at 37°C, and then stored. Stability assays described in the next subsections were performed after all films had been collected by the end of the 21 days.

#### 3.3.3.1. Resistance measurement

A preliminary experiment was done to assess the coating stability. Four films were coated with each of the six coating protocols described in section 3.3.2. The resistance on the surface of films was measured using a Velleman DVM832 multimeter, with probes 1 cm apart. This measurement corresponded to the initial time point of the experiment. Next, films were submerged in PBS solution in closed containers and placed in an incubator at 37°C. Every 24 h, for seven days, the films were taken from PBS and the resistance measurement was repeated, to assess its variation.

#### 3.3.3.2. Electroconductivity measurement: 4-point probe method

The electroconductivities of the coated films were measured with the standard four-point probe method. For that purpose, four stripes of gold were deposited over the films by physical vapor deposition with an Edwards E306A thermal evaporator, across the entire films and with equal distance from each other. Measurements were done in triplicate. By applying a range of currents at the outer contacts, potential differences were measured between the two inner contacts. Using Ohm's law ( $R=V/I$ ), the resistance,  $R$ , is given by the slope between the potential  $V$  and the current  $I$ . At a constant temperature,

the resistance of the sample,  $R$ , is proportional to its resistivity,  $\rho$ , and to the separation between the two inner contacts,  $L$ , and inversely proportional to the cross-section,  $A$  (product of the coating thickness,  $t$ , by its width,  $w$ ), as described by equation 3.1.

$$R = \rho \times \left(\frac{L}{A}\right) \text{ [S}^{-1} \text{ or } \Omega] \quad 3.1$$

Therefore, electroconductivity,  $\sigma$ , was obtained calculating the reciprocal of the determined resistivity, using equation 3.2.

$$\sigma = \frac{1}{\rho} \text{ [S cm}^{-1}] \quad 3.2$$

The coating thickness,  $t$ , was measured with a Bruker's Dektak 3.21 Profilometer. With a scalpel, the coating superficial layer was scrapped off, until reaching the PCL film. The thickness was measured upon surface scanning perpendicularly to the cut.

#### 3.3.3.3. *Attenuated total reflectance-Fourier-transform infrared (ATR-FTIR) spectroscopy*

ATR-FTIR analysis was done to pristine and PEDOT:PSS coated PCL films, and also to the crosslinker coating dispersions. Concerning the dispersions, in order to have samples analyzable in the spectrometer, they were prepared as described in section 3.3.2 ii and iii and were placed in an incubator at 55°C until fully dried. Analysis was performed using a Spectrum Two FT-IR Spectrometer (Perkin-Elmer, Waltham, MA, USA). Transmittance spectra were obtained over the region from 400 to 4000  $\text{cm}^{-1}$ , with a resolution of 1  $\text{cm}^{-1}$ , at room temperature and with an accumulation of 8 scans.

#### 3.3.3.4. *Contact angle*

Contact angle measurements were performed through the sessile drop method using a Krüss DSA25B goniometer. A drop of distilled water was deposited on the surface of the various films and its shape recorded every 0.5 s for 1 minute, to allow drop stabilization. To determine if a measurement should be considered, the last ten angle measurements were analyzed. If any of those values was more than 1° away from the last ten average, that measurement was discarded. Seven replica measurements ( $n=7$ ) were done for each condition and results were analyzed using the software Drop Shape Analysis 4 version 2.1.

### 3.4. Scaffold fabrication and characterization

During this work a variety of 3D FDM-based scaffolds were developed, involving four main purposes. The first, was the creation of a 3D PCL scaffold that would be coated with PEDOT:PSS, creating a novel material to be used in electroconductivity assays. The second, concerned the creation of scaffolds with a curved structure, as a step in the creation of scaffolds mimicking the natural curvature of tissues. The third, concerned designing a scaffold reproducing the knee medial condyle structure and curvature. And the fourth, to demonstrate techniques for fast prototyping of scaffolds with a wide variety of geometries. In chapter 4 the detailed designing of all these scaffolds is presented.

Considering these many scaffolds and the purposes with which they were created, their characterization was done only with the methods considered relevant while the work progressed. However, it does not invalidate that further characterization could be meaningful in the future. In the next subsections, the utilized characterization techniques will be described, as well as to which scaffolds they were applied.

### 3.4.1. Scaffold manufacturing

PCL scaffolds, with the objective of being coated with the PEDOT:PSS dispersions, were designed in Fusion 360 and manufactured by FDM. The chosen dimensions for these scaffolds were 10.5 mm × 10.5 mm × 3 mm, with a 0-90° lay-down pattern and aligned fibers (cf. Figure 2.16). The selected size for the pore and for the scaffold fibers was 300 μm. Since 300 μm is a dimension too high to be printed with a 0.25 mm nozzle, printing layer height was set to 150 μm, meaning that two layers were necessary to print each scaffold fiber. Ahead, in section 4.1, the detailed design and manufacturing process will be described and analyzed. For printing, the default profiles created to print with PCL were used, as described in section 3.2, but with the following modifications: in the print settings, first layer height was set to 0.15 mm, detect thin walls option checked, minimum of 2 loops for the skirt, a 2 layer height for the skirt, travel speed for non-print moves was reduced to 45 mm/s, and extrusion width for the first layer was set to 0.25 mm; in the printer settings, the retraction length was increased to 1.2 mm, the Z lift (when there is a retraction) was increased to 0.3 mm, and the extra length on restart (after a retraction) was increased to 0.12 mm.

The scaffolds reproducing the knee medial condyle surface and the scaffolds to demonstrate techniques for fast prototyping with a wide variety of geometries were also printed in PCL. For both, the printing profile described in the previous paragraph was used.

The curved scaffolds were printed with PLA, and for that reason the PLA printing profiles described in section 3.2 were used, although with the following modifications: in the print settings, first layer height was set to 0.15 mm, detect thin walls option checked, a 1 layer skirt height, travel speed for non-print moves was reduced to 45 mm/s, and extrusion width for the first layer was set to 0.25 mm; in the filament settings, nozzle temperature for the first and all other layers was set to 210 °C, and the bed temperature for the first and all other layers was set to 65 °C; in the printer settings, the retraction length was increased to 1.2 mm, and the Z lift (when there is a retraction) was increased to 0.3 mm.

### 3.4.2. Coating and crosslinking protocol

This procedure was executed only with the scaffolds for electroconductivity assays, and the same coating and crosslinking protocol described in section 3.3.2 for the PCL films was followed.

### 3.4.3. Compressive mechanical testing

The scaffolds were evaluated under uniaxial compressive mechanical testing using a TA.XTplusC Texture Analyser (Stable Micro Systems, Godalming, Surrey, United Kingdom) equipped with a 50 kg load cell. A displacement rate of 1 mm/min was used and six different scaffold specimens (n=6) were tested for each condition. Exponent Connect software (Stable Micro Systems) was used to collect and



process the experimental data. The compressive moduli were calculated from the slope of the initial linear regions of the stress-strain curves. The maximum stresses withstand by the scaffolds were determined from the maximum of these stress-strain curves.

#### 3.4.4. Micro-computed tomography analysis

Internal microstructure images of PCL scaffolds were obtained using micro-computed tomography (micro-CT) with a SkyScan 1174v2, Bruker version 1.1 (Bruker, Billerica, MA, USA). Image reconstruction was performed using NRecon Program Version 1.6.8.0 (Bruker), CTVox and CTVol softwares version 2.3.2.0 (Bruker) were used to obtain realistic 3D visualizations of the scanned scaffold samples, and CTAn version 1.20.0 software (Bruker) was used for image analysis.

The acquisition parameters depended on the sample being analyzed. With the scaffolds for electroconductivity assays, the following parameters were used: source voltage of 50 kV; source current of 800 mA; image pixel size of 14  $\mu\text{m}$ ; exposure time of 6000 ms; rotation step of 0.5°; frame averaging on (2); no filter. For the curved scaffolds, in order to have greater detail in the reconstructions, the following parameters were used: source voltage of 50 kV; source current of 800 mA; image pixel size of 30.11  $\mu\text{m}$ ; exposure time of 9000 ms; rotation step of 0.5°; frame averaging on (3); no filter.

#### 3.4.5. Computational simulation of compressive mechanical behavior

Finite element analysis (FEA) was performed using the Solid Mechanics (solid) module from COMSOL Multiphysics 5.5 software (COMSOL, Sweden). A stationary study was considered, with the objective of determining the stresses when scaffolds are subjected to compressive forces. This analysis was performed only for the curved scaffolds.

Sections of the scaffolds in STEP format were imported into COMSOL, where a physics-controlled mesh with extra-fine element size was used to generate the elements of the model. The assigned scaffold material was PLA, from the software materials library. For the solid mechanics studies, the faces of the scaffold corresponding to the AC side were subjected to a boundary load of 1 MPa, and the faces of the scaffold corresponding to the subchondral bone side were constrained to a fixed position. Results were calculated for the von Mises Stress (solid.mises plot) and for displacement (solid.disp plot).

### 3.5. Statistical analysis

Throughout this work, when applicable, the results are presented as mean values  $\pm$  standard deviations (SD). The statistical analysis was performed using GraphPad Prism 9.2 (GraphPad Software, San Diego, CA, USA). To assess statistically significant differences between independent samples, ANOVA tests were performed followed by Tukey's multiple comparison test. Statistically different values were considered for p-value < 0.05 (95% significance level; \* denotes p<0.05, \*\* denotes p<0.01, \*\*\* denotes p<0.001, \*\*\*\* denotes p<0.0001). The number of replicates varied between experiments and, for that reason, will be indicated whenever the statistical analysis is presented.

## 4. Results and Discussion

### 4.1. Procedures for the fabrication and characterization of electroconductive orthogonal scaffolds

#### 4.1.1. Orthogonal scaffold design

From previous works<sup>120,121</sup>, an orthogonal scaffold model with 0°-90° orientated fibers was already available. However, to accommodate the requirement of having a scaffold that would fit in a 24 well plate and to have the possibility of manufacturing scaffolds with different pore and fiber dimensions, a new scaffold was designed in Fusion 360. To expedite the creation of different models, at an early stage of the work when this design was created, the parameters indicated in Table 4.1 were chosen as the necessary to determine scaffold geometry. So, it would only be necessary a change in a parameter value for the software to automatically create a different design. At this stage, pore and scaffold fibers were defined by the same parameter and had necessarily the same dimension. Figure 4.1 shows the steps involved in the design of the scaffold.

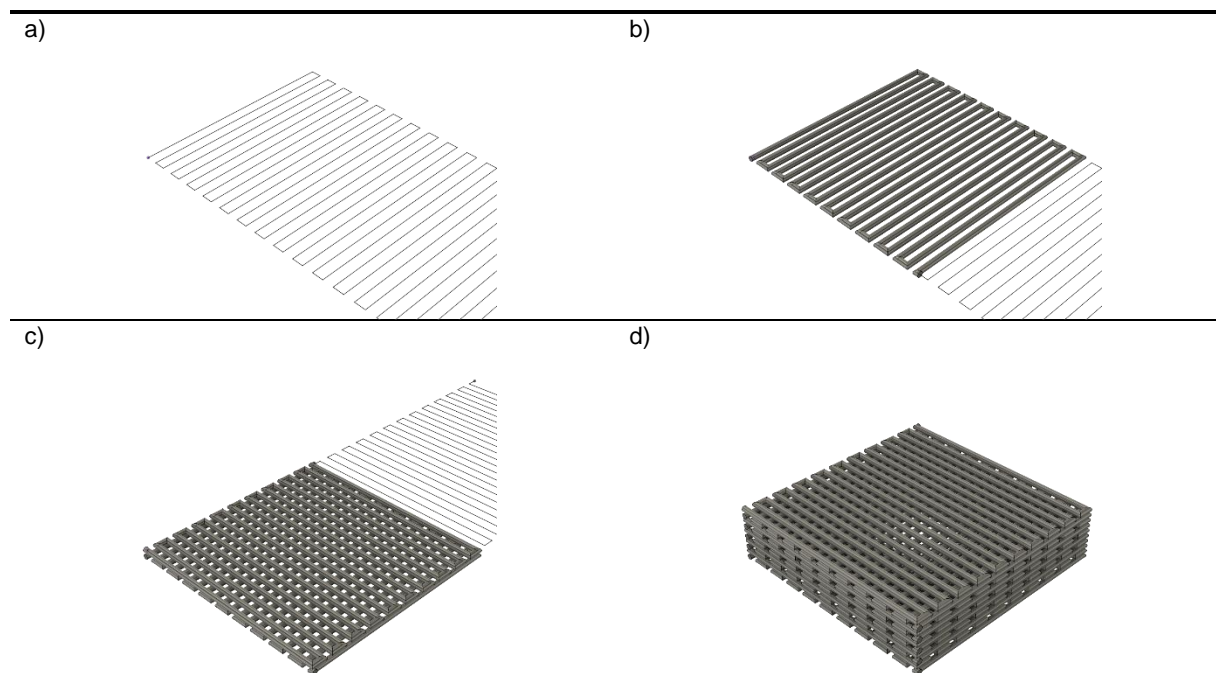


Figure 4.1 – Steps in the design of orthogonal scaffolds in Fusion 360: a) Sketch of an S shaped path along the x-axis; b) Creation of a scaffold fiber along that path; c) Repetition of sketch and fiber creation along the y-axis, on top of the previous fiber; d) Copy of the previous two scaffold fibers along the z-axis.

An important parameter for scaffold characterization as well as relevant for its performance that can be predicted from the model is porosity. Taking advantage of the software capabilities, fiber and total scaffold volume can be easily calculated. If a fiber cross-section with a square shape is considered, as an approximation of the shape of the filament extruded by FDM, a porosity of 47.18% ( $156.06 \text{ mm}^2 / 330.75 \text{ mm}^2$ ) is obtained. Variability in FDM extrusion width and the possibility of pore occlusions during

manufacturing will affect porosity and therefore, if experimental porosity data were available, it would be possible to determine the fidelity between the 3D print and the designed model.

Table 4.1 – Parameters chosen to determine the size and geometry of orthogonal scaffolds.

Model parameters	Comments	Designed
Width of scaffold fibers	Pore width assumes the same value	0.3 mm
Height of scaffold fibers	Corresponds to layer height	0.3 mm
Number of fibers along x-axis	Determines the size along x-axis	20
Number of fibers along y-axis	Determines the size along y-axis	20
Number of repetitions of the first two layers	Determines scaffold thickness	5

#### 4.1.2. Manufactured electroconductive films and scaffolds

As described in sections 3.3.1 and 3.4.1, PCL films and scaffolds were manufactured by FDM, and coated with electroconductive dispersions, as described in sections 3.3.2 and 3.4.2. The appearance of films and scaffolds before and after coating is exemplified in Figure 4.2, with the dark blue color indicating that some material was deposited over the PCL. From a visual inspection, only a thin layer was deposited, with pores remaining opened. Some occlusions can however be seen, which are most likely to be caused by excess coating dispersion that remained bound to the scaffolds due to surface tension. The procedures described in the following subsections were carried out to have a systematic and precise characterization of the properties of coatings.

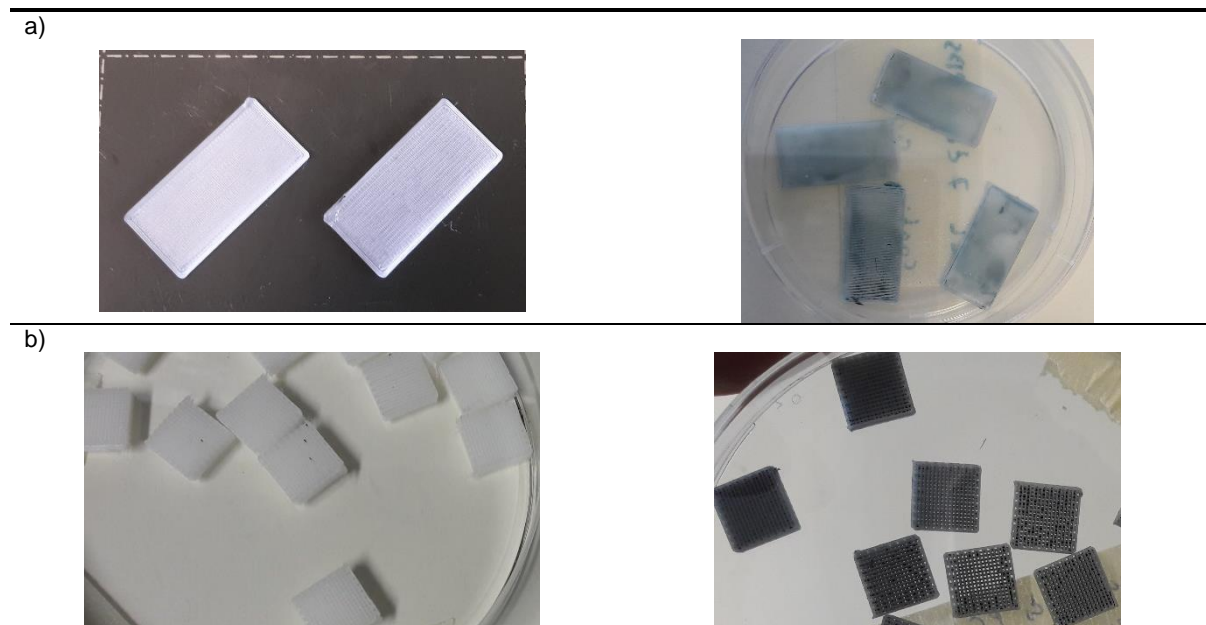


Figure 4.2 – Representative images of manufactured PCL films and scaffolds before and after coating with PEDOT:PSS dispersions: a) 2 mm x 1 mm x 0.5 mm films (left), and coated with PEDOT:PSS(GOPS) (right); b) 10.5 mm x 10.5 mm x 3 mm scaffolds (left), and coated with PEDOT:PSS(GOPS) (right).

### 4.1.3. Coating characterization

In order to make a preliminary assessment of the stability of the six different PEDOT:PSS coatings, described in section 3.3.2, the resistance on the surface of four films for each condition was measured over 7 days. The objective was to estimate qualitatively, with a very simple procedure, the effect of GOPS and DVS binding to PSS on the stabilization of the coatings, before doing the more time consuming four-point probe electroconductivity measurements. The evolution of the resistance measurements is shown in Figure 4.3. It can be observed that the initial measurements have the lowest resistance, which would relate to higher conductivities. The measured resistances showed an increase after that initial measurement but seemed to stabilize by the end of the 7 days. This observation suggested that the coatings were not delaminating and that a stability assay could also be conducted over a longer period of 21 days, a period that would be compatible with cell proliferation and differentiation experiments. Two of the six coating conditions are not represented in Figure 4.3, because the measured resistances were higher than the detection limit of the multimeter (over 2 M $\Omega$ ). When both PCL and PCL(NaOH) were coated only with PEDOT:PSS without any cross-linker, the coating seemed more brittle throughout the 7 days of the assay, with bits of coating coming loose more easily. Without the cross-linkers, a sufficiently thick continuous layer may also not have formed, which might explain why the resistance was so high. Since this was only a preliminary measurement to assess stability resorting to a multimeter, significance among the conditions was not investigated.

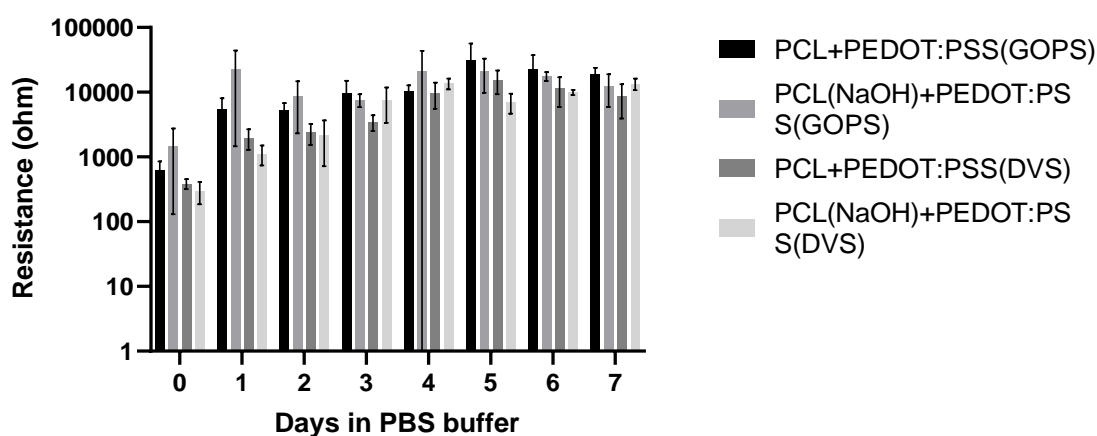


Figure 4.3 – Measured resistance with a multimeter, over 7 days, on the surface of coated PCL films submerged in PBS and at 37°C. PCL films and alkaline treated PCL films (PCL(NaOH)) coated with PEDOT:PSS are not represented because the measured resistances were above the detection limit of the multimeter. Results are expressed as mean  $\pm$  SD ( $n=4$ ). (Resistance log scale).

In order to assess the effect of the different cross-linking strategies on the electroconductivity of PEDOT:PSS coated films, another assay was conducted before the longer 21 days stability assay. Electroconductivity was measured with the four-point probe method on the surface of films that were coated following the six strategies described in section 3.3.2, without submerging them in PBS (corresponding to day 0). The results are shown in Figure 4.4. It can be observed for both cross-linking strategies an improved electroconductivity in relation to the coating only with PEDOT:PSS, although this improvement was only statistically significant in comparisons with PCL+PEDOT:PSS(DVS). Still,

observations seem to suggest an enhancing effect due to the cross-linker protocols, confirming findings already reported in previous studies<sup>69,72</sup>. Both protocols increase electroconductivity in comparable extents, only with a statistically significant difference comparing PCL(NaOH)+PEDOT:PSS(GOPS) and PCL+PEDOT:PSS(DVS). Considering the alkaline treatment, it was a strategy used to functionalize PCL and make it more reactive<sup>122</sup>. However, there was no clear effect identified to support or oppose the use of an alkaline treatment. The mean electroconductivity of the alkaline treated scaffolds was lower in relation to the pristine scaffolds, though the difference was not significant. Concerning the mean electroconductivity values determined, they are below 0.01 S/cm for PCL and PCL(NaOH) films coated with PEDOT:PSS and range between 0.73-16 S/cm for the coatings using cross-linkers. From previous works in the SCERG group, coatings with a mean conductivity of 12 S/cm have been used for ES studies with neural stem cells<sup>123</sup>. Therefore, it is plausible that the coating procedures using the cross-linkers may be used for ES studies, related with OC tissue, having conductivities with the same magnitude.

It should also be pointed out that there was a great variability in the electroconductive measurements obtained, seen in the error bars in Figure 4.4. The primary cause for this variability was the need to determine the height of the PEDOT:PSS coatings deposited over the PCL films in order to perform the four-point probe method calculations. The procedure involved using a scalpel to remove the superficial PEDOT:PSS coating from the PCL films and then measuring the height of the coating layer with the profilometer. However, scraping needed to be very precise to not affect the PCL, and that might not always have been the case.

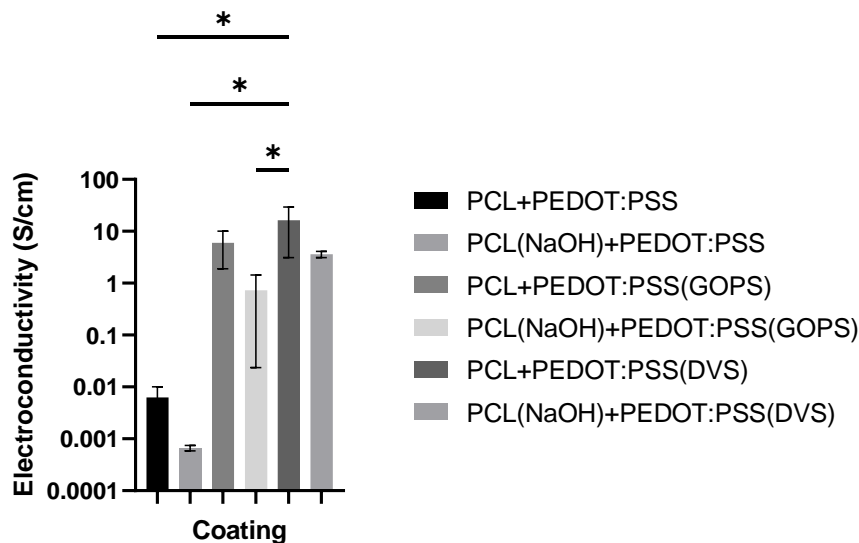


Figure 4.4 – Calculated conductivity, with the four-point probe method, on the surface of coated PCL films. Results are expressed as mean  $\pm$  SD (n=3). (Electroconductivity log scale).

Based on the obtained results, it was decided to run a 21 days stability assay only with films coated using the protocols including the cross-linkers due to the reduced stability and electroconductivity of coatings using PEDOT:PSS alone. The assay was performed with both PCL and PCL(NaOH) films because no evidence had been gathered to support one alternative over the other. Groups of coated films were immersed in PBS and placed in an incubator at 37°C and 5% CO<sub>2</sub>. At the chosen time points

the necessary number of films was withdrawn from each condition to conduct the characterization assays.

Figure 4.5 shows the results of the electroconductivity measurements on the coated films. Electroconductivity values do not show any significant variation throughout the 21 days of the experiment, as confirmed by the 2-way ANOVA test: at a significance level of 5%, the variation between the five time points, the variation between the four coating strategies, and the interaction variation were all non-significant. Contrary to what was seen in Figure 4.3, using the more precise four-point probe method there was no substantial decrease in conductivity in relation to day 0, giving an indication that the coatings are stable and not delaminating. The mean values are in the range 3.0-26 S/cm, again close to values already used in cellular ES studies<sup>123</sup>. As referred previously and also observed in Figure 4.4, the standard deviation error bars are considerably large, suggesting a high variability in the measurements. Once again, the reason might be need of scraping the PEDOT:PSS coatings from the surface of the films, and due to the softness of PCL some may have been removed together with the coating. Thus, from Figure 4.5, it was not possible to identify a coating strategy with a better performance in comparison to the others.

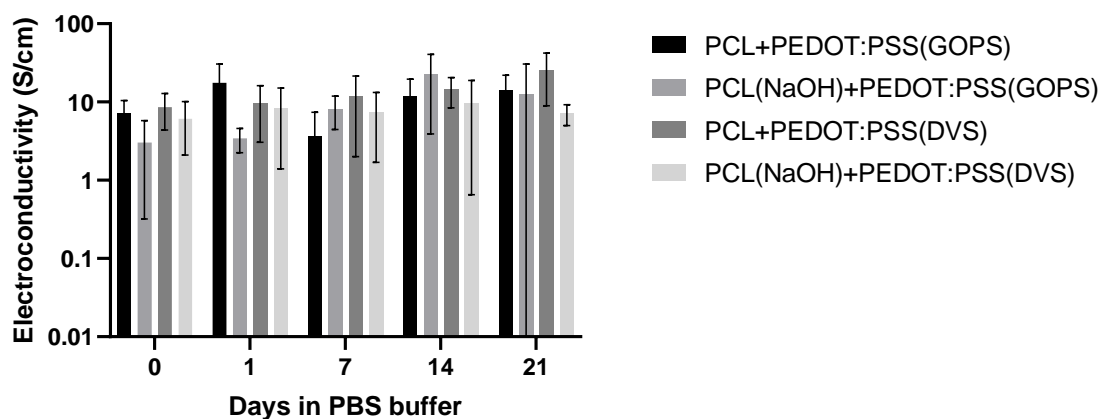


Figure 4.5 – Calculated conductivity with the four-point probe method for the coating stability assay. Conductivity was measured on coated PCL films submerged in PBS at 37°C and 5% CO<sub>2</sub>. Films were collected to be analyzed on the days 0, 1, 7, 14, and 21 of the stability assay. Results are expressed as mean ± SD (n=3). (Electroconductivity log scale).

Figure 4.6 depicts the ATR-FTIR spectra of the coating dispersions, uncoated PCL and PCL(NaOH) films (used as controls), and coated PCL and PCL(NaOH) films. Concerning the two coating dispersions (PEDOT:PSS(GOPS) and PEDOT:PSS(DVS)), the spectra are dominated by the ethylene glycol that is also present in the coating formulations and is identified by its characteristic peaks (broad peak centered at about 3300 cm<sup>-1</sup> corresponding to O-H stretching, two peaks above and below 2900 cm<sup>-1</sup> corresponding to C-H stretching, a peak around 1460 cm<sup>-1</sup> corresponding to the CH<sub>2</sub> bending of an alkyl group, peaks around 1085 cm<sup>-1</sup> and 1035 cm<sup>-1</sup> corresponding to C-O stretching and C-C-O asymmetric stretching, and peak around 880 cm<sup>-1</sup> corresponding to C-C-O symmetric stretching)<sup>124,125</sup>, and the weak PEDOT:PSS peaks between 400 cm<sup>-1</sup> and 1600 cm<sup>-1</sup> are not discernible<sup>126</sup>. The reduced volumes of GOPS, DVS, and DBSA present in the coating dispersions also prevent the detection of the corresponding peaks. Concerning the uncoated and coated PCL films, due to the very thin coating layer

that was deposited, the spectra are dominated by the PCL characteristic peaks (double peaks between 2800  $\text{cm}^{-1}$  and 3000  $\text{cm}^{-1}$  corresponding to C-H stretching of the methylene groups, a peak around 1720  $\text{cm}^{-1}$  corresponding to C=O stretching, with the variety of peaks between 700  $\text{cm}^{-1}$  and 1600  $\text{cm}^{-1}$  corresponding to many other PCL characteristic modes of absorption)<sup>127</sup>. With these substances showing such a dominance in the ATR-FTIR spectra, it is not possible to analyze the chemical reactions occurring during annealing between PEDOT:PSS, the cross-linkers and other substances. The effect of alkaline treatment on the spectra is also not noticeable, most likely because it is only superficial.

As previously mentioned, one film was collected at each time point for each coating to be analyzed by ATR-FTIR. The obtained spectra are presented in annex A.1. Since PCL is present in a much greater quantity in relation to the coating substances in the analyzed films, no significant variation was identified in the spectra throughout the 21 days of the assay, and no definite conclusions could be drawn about the coating stability using this characterization method.

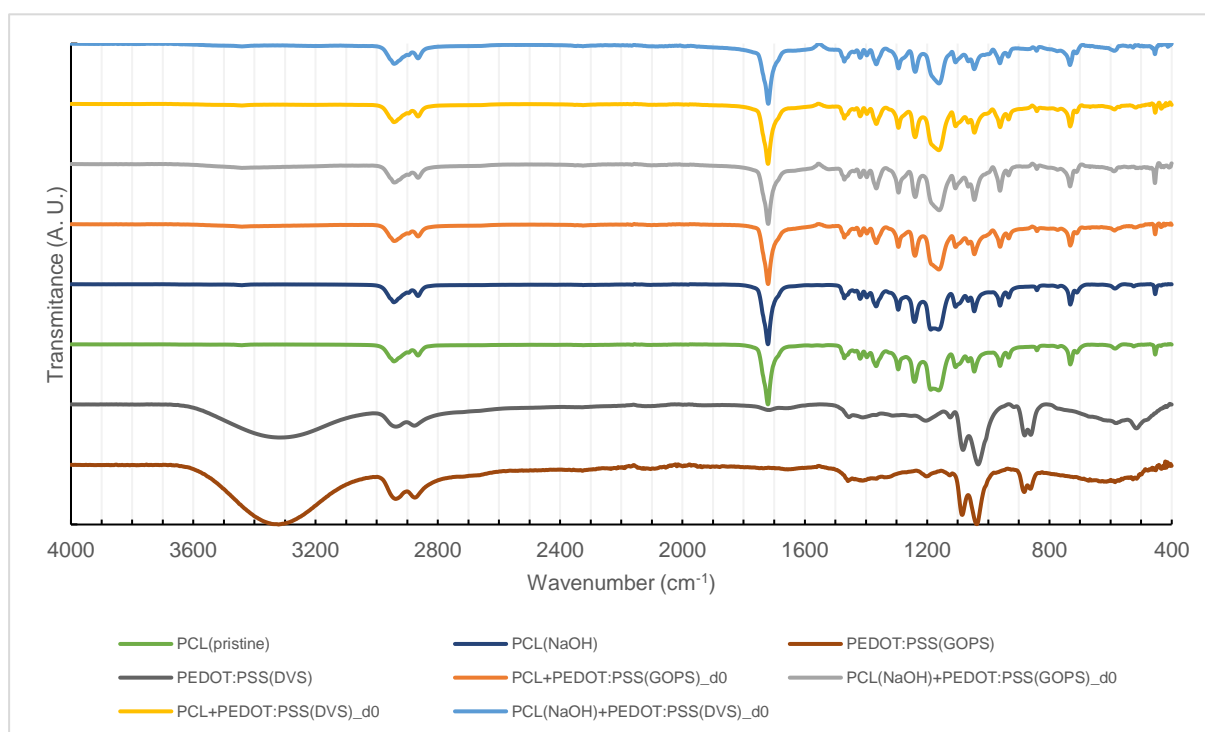


Figure 4.6 – ATR-FTIR spectra of samples of uncoated PCL films, samples of coating dispersions, and samples of coated PCL films collected at the day 0 of the stability assay.

Hydrophilicity of the uncoated and coated films was determined measuring the contact angle. Figure 4.7 shows representative pictures of water droplets on the films and the respective values, and Figure 4.8 shows the determined contact angles of the analyzed samples. If an angle is superior to 90° a surface is considered hydrophobic and if it is inferior to 90° it is considered hydrophilic. In the tested samples, PCL is the least hydrophilic, however still below the 90° threshold while all the other samples are more hydrophilic.

By performing the coating procedures, a new surface was added over the PCL, which can have an effect on cell behavior. Modifying surface hydrophilicity and roughness has been a strategy used to



improve cell attachment, despite still not existing a clear relation between hydrophilicity and cell attachment, with studies showing contradictory results<sup>119</sup>.

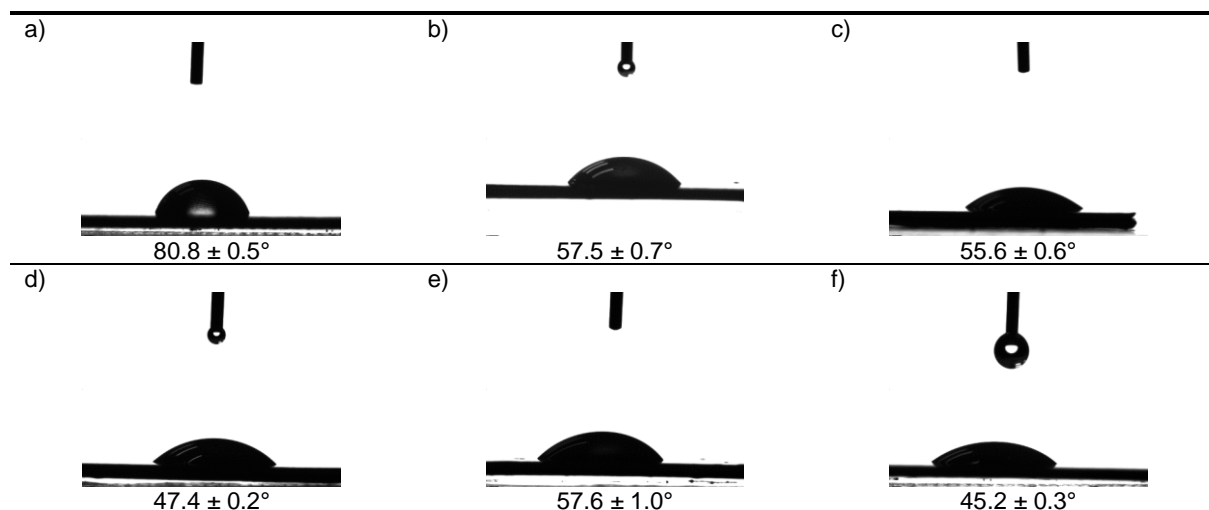


Figure 4.7 – Representative pictures of water droplet contact angles on PCL films: a) Pristine PCL; b) PCL(NaOH); c) PCL coated with PEDOT:PSS(GOPS); d) PCL coated with PEDOT:PSS(DVS); e) PCL(NaOH) coated with PEDOT:PSS(GOPS); f) PCL(NaOH) coated with PEDOT:PSS(DVS). The corresponding angles are shown below each photograph.

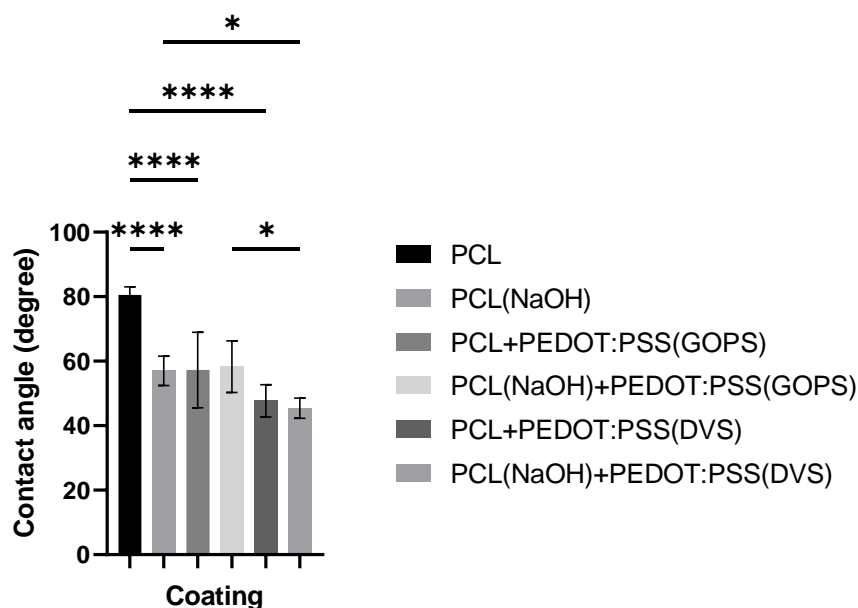


Figure 4.8 – Contact angle on the surface of uncoated and coated PCL films determined by the sessile drop method. Coated films were collected to be analyzed on day 0 of the stability assay. Results are expressed as mean ± SD (n=7).

Significant differences were found in all pairwise comparisons with pristine PCL. Using DVS as a crosslinker seems to have a greater effect increasing hydrophilicity, but only the comparison between PCL(NaOH)+PEDOT:PSS(GOPS) and PCL(NaOH)+PEDOT:PSS(DVS) was significant. From previous works<sup>119</sup>, it was expected that pristine PCL would have a contact angle above 90°, which was not confirmed. Possible explanations may be that some hydrolytic degradation might already have occurred



on the filament material due to being stored exposed to the laboratory environment, without any protection, or that some other components may be present in the purchased PCL filament, causing a decrease in contact angle. However, these possibilities could not be verified.

Concerning the alkaline treatment, the change to the film surface was confirmed, verified by the decrease in the contact angle, in relation to the untreated films (PCL vs. PCL(NaOH)). Remarkably, when the films were coated with the PEDOT:PSS dispersions, the coatings resulted in a range of values for contact angle measurements similar to the PCL(NaOH) samples. The alkaline treatment also did not seem to interfere with the coating procedure. The two coatings with PEDOT:PSS(GOPS) did not show a significant difference between them, and the same was verified for the two coatings with PEDOT:PSS(DVS).

#### 4.1.4. PEDOT:PSS-coated PCL scaffold characterization

The mechanical characterization of the scaffolds was done through compressive testing. Figure 4.9 shows representative stress-strain curves of the analyzed PEDOT:PSS-coated PCL scaffolds. Uncoated PCL scaffolds and alkaline treated PCL scaffolds were used as controls. One substantial difference was seen between the coated and uncoated scaffolds. All coated scaffolds shattered during the compression test (Figure 4.10), while the uncoated scaffolds, although plastically deformed, maintained structural integrity. A plausible explanation may be related with the acidic PEDOT:PSS dispersion used in the coating procedure causing an acid catalyzed degradation of PCL, which has been described<sup>128</sup>. Moreover, some structural modifications to the PCL during annealing should not be ruled out. This process was carried out at 55°C for 24 hours, close to the PCL melting temperature (around 60°C), which may have led to polymer chain rearrangements.

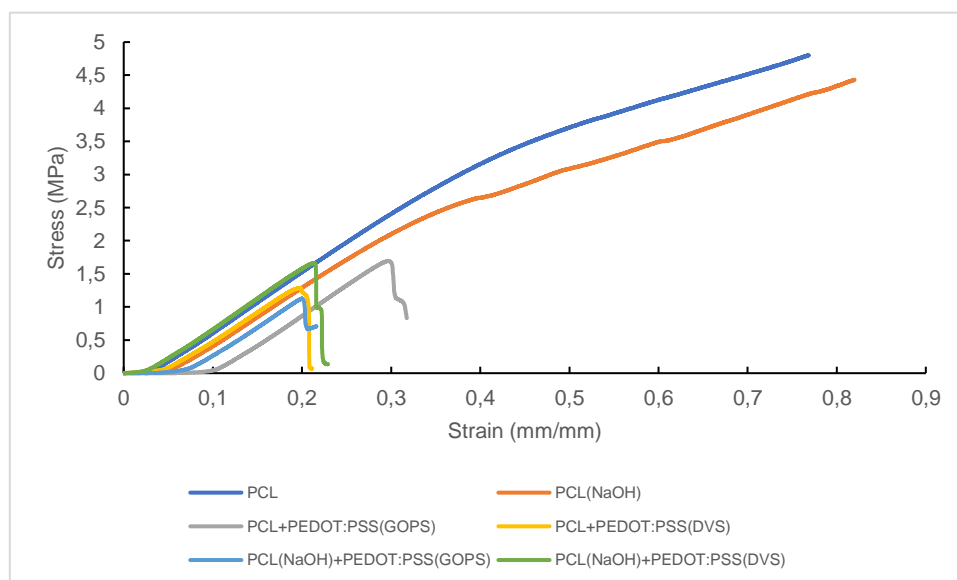


Figure 4.9 – Representative compressive stress-strain curves of uncoated and PEDOT:PSS-coated PCL scaffolds.

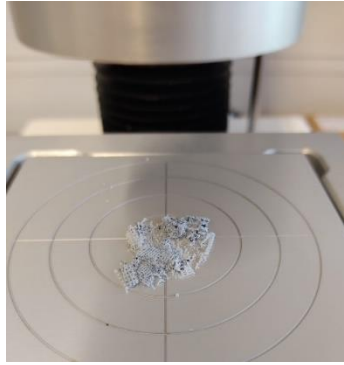


Figure 4.10 – Representative picture of the collapse of the coated PCL films during compressive mechanical testing. The collapse occurred in all samples with coating (PCL+PEDOT:PSS(GOPS) and PCL+PEDOT:PSS(DVS)) and did not occur in the uncoated control samples (PCL and PCL(NaOH)).

Considering the compression moduli, calculated from the initial linear regions of the stress-strain curves, all were very similar, only with statistically significant differences observed when comparing PCL(NaOH)+PEDOT:PSS(GOPS) with PCL(NaOH)+PEDOT:PSS(DVS) (Figure 4.11). Neither the alkaline treatment nor the possible effect of the acidic PEDOT:PSS coating dispersion evidenced an effect in the compressive modulus. Particularly in the case of alkaline catalyzed degradation, a decrease in the compression modulus has been reported in similar conditions (24 hours in 1 M NaOH)<sup>119</sup>, but it was not reproduced in the current work. Longer exposure to NaOH, in the order of weeks, might be necessary to identify a reduction in the modulus<sup>128</sup>. In relation to the obtained compressive modulus values, they are inside the range of 2.41-77 MPa of PCL scaffolds manufactured by FDM reported in the literature<sup>129</sup>.

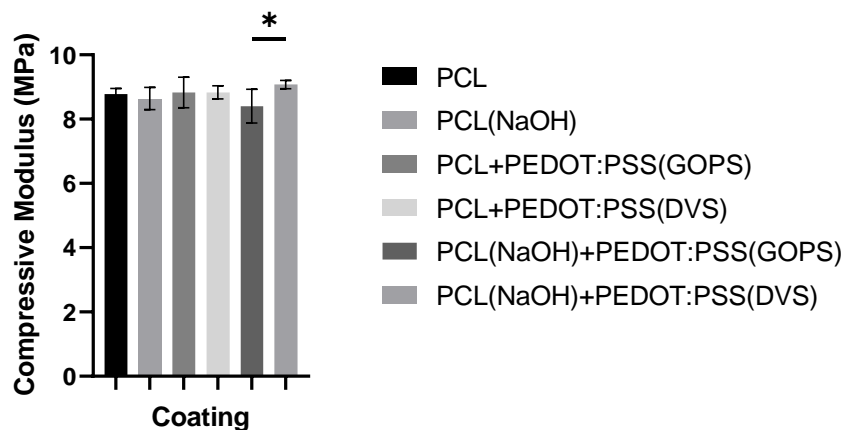


Figure 4.11 – Compressive Young's modulus of uncoated and PEDOT:PSS-coated PCL scaffolds. Results are expressed as mean  $\pm$  SD (n=5).

The maximum stresses for the PEDOT:PSS-coated and uncoated scaffolds were estimated from the stress-strain curves (Figure 4.12). These represent the stresses scaffolds can withstand before breaking. Uncoated scaffolds deformed plastically but did not break using the 50 kg load cell while maximum stress was achieved for the PEDOT:PSS-coated scaffolds. However, there is no significant difference between the determined maximum stress values. As referred previously, this implies a relation between the coating and annealing procedure with the reduction in the maximum stress.

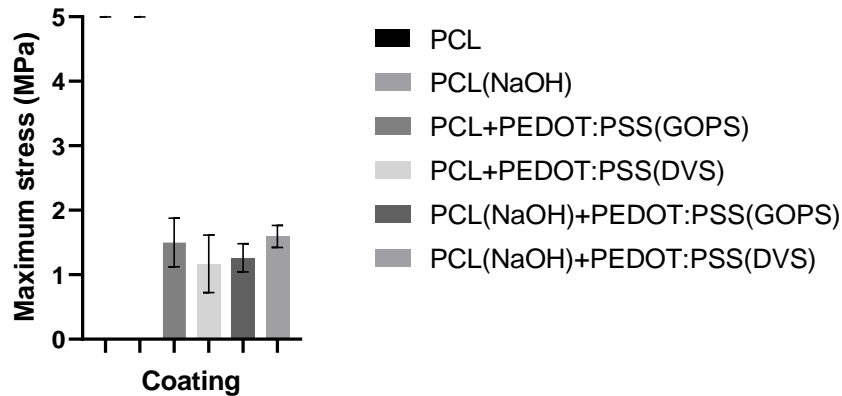


Figure 4.12 Estimated maximum stresses of uncoated and coated PCL scaffolds. Results are expressed as mean  $\pm$  SD (n=5).

To study the morphological features and the fidelity between the printed scaffolds and the created designs, a micro-CT reconstruction was done with one sample of each of the four PEDOT:PSS-coated scaffolds and of the two uncoated scaffolds. Representative pictures of the obtained reconstructions are shown in Figure 4.13. In both 2D plane cuts and 3D reconstruction, the designed grid pattern can be identified and also the individual strands of filament deposited during the FDM printing process, clearly showing the two passages of the printhead to create each scaffold fiber. In Figure 4.13a it is also possible to identify some vestiges of the coating dispersion, manifested in the bright spots in the coronal cut, which remained adhered to the scaffold during the annealing process. A similar situation was normally found in the other coated scaffolds. Although they do not seem to be occluding the pores, it will be important to understand if it will constitute an obstacle to cell proliferation and differentiation and also to the transport of nutrients within the scaffold.

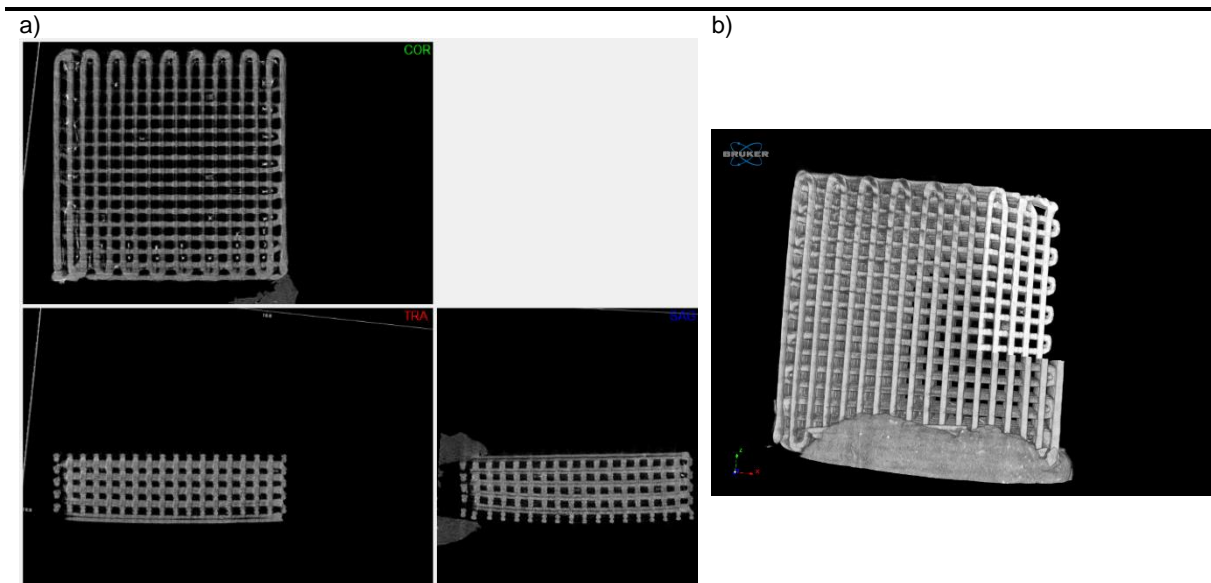


Figure 4.13 – Micro-CT imaging reconstructions: a) Representative pictures of coronal, transverse, and sagittal cuts of a PCL scaffold (PCL+PEDOT:PSS(GOPS) scaffold in the picture); b) Representative 3D reconstruction, (with a cut section) of a PCL scaffold (PCL(NaOH)+PEDOT:PSS(DVS) scaffold in the picture).

In order to evaluate the accuracy of the printing process, for each scaffold, the transverse cut was used to measure the dimension of 3 consecutive pores and fibers. Figure 4.14 shows an agreement between the designed pore and scaffold fiber dimensions, both designed with 0.3 mm, and the calculated values of those two features. Some variations around the 0.3 mm can be accounted by some experimental imprecision in selecting the correct plane for the transverse cut. At a significance level of 5%, no differences were determined between the estimated dimensions of the scaffolds.

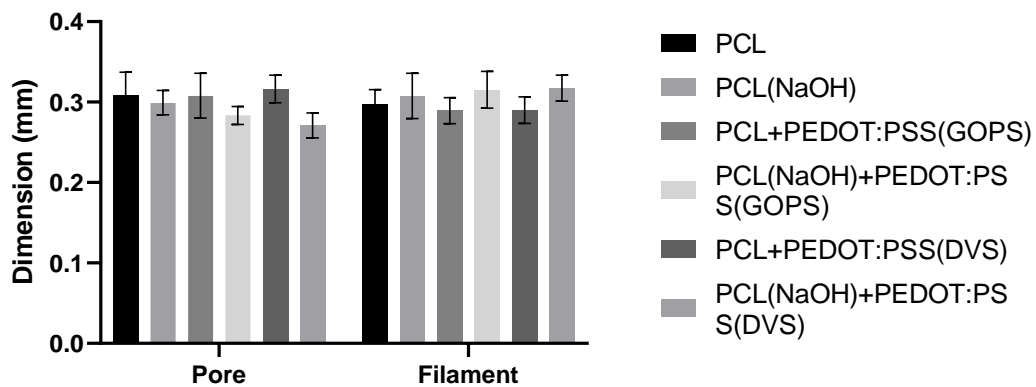


Figure 4.14 –Pore and fiber dimensions of uncoated and PEDOT:PSS-coated PCL scaffolds, estimated from measurements in transverse cuts obtained from micro-CT imaging. Results are expressed as mean  $\pm$  SD (n=3).

From all gathered evidence in the film and scaffold characterizations, there was no clear distinction between the two coating strategies. Thus, further characterization methods could prove beneficial, namely scanning electron microscopy (SEM) analysis of both films and scaffolds to verify the effect of the alkaline treatments on PCL and maybe verify coating thickness.

## 4.2. Designs for osteochondral tissue engineering applications

### 4.2.1. Processes for the quick design of scaffolds

To create scaffolds with a non-orthogonal geometry (lay-down pattern between fibers different than 0°-90°), new models had to be created in Fusion 360 since the design described in section 4.1.1 would not accommodate the desired modifications. As before, the design would take advantage, as much as possible, of parametric design, so that changes in geometry could be quick, easy, and automated. The processes to create models with non-orthogonally rotated layers, with pore size variation, and with a pore gradient along the layers are described below.

Scaffolds manufactured with designs from this section are shown with the sole intent of demonstrating the possibilities of the quick design processes. Although it would be compelling to further characterize them, time constrains and the fact that the coating procedure would not be applied to these scaffolds at this moment, ruled out those characterization studies.

#### 4.2.1.1. Layer rotation

The process to create a scaffold where the angle between successive layer fibers would not be the usual 90° started with the construction of yet another model with orthogonal layers, but in which the angle of the second layer in relation to the first could be altered. Then, it would only be necessary to change the angle between layers in order to have a new design. Table 4.2 shows the parameters that were chosen to control scaffold geometry, again based in typical values found in the literature<sup>130</sup>. The parameters were adapted so that the scaffold would have a total dimension similar to the scaffold described in section 4.1.1.

In relation to the model in section 4.1.1, pore and fiber width are now defined independently. Fibers were again drawn with a circular cross-section, defined by the “fiber width” parameter. However, at the time this model was being designed, the intention to simulate computationally the mechanical behavior of scaffolds had already been settled. To perform these simulations it was necessary that fibers in successive layers intersected each other. The tangential contact of previous designs was not adequate for the simulations. With this purpose, the “layer height” parameter was added to the model. In this way, all scaffold layers would still be 0.3 mm high, but model fibers could be slightly larger, ensuring that their intersection defined a volume in space. Considering scaffold dimensions, a note should be made about the parameter “Number of fibers parallel to y-axis.” It allows the control over the size along the x-axis. The actual number of fibers only matches the defined value when layers are rotated 90° apart. When the angle between layer is different, the scaffold will have a different number of fibers in that layer, however the size along the x-axis remains the same.

Table 4.2 – Parameters chosen to determine the size and geometry of scaffolds with layer rotations.

Model parameters	Comments	Designed orthogonal example
Number of fibers parallel to x-axis	Determines the dimension along the y-axis	13
Number of fibers parallel to y-axis	Determines the dimension along the x-axis	13
Pore width		0.39 mm
Fiber width		0.3 mm
Layer height	Determines the height difference between the rotated layers	0.3 mm
Number of repetitions of the first two layers	Determines the scaffold thickness	6

Figure 4.15 presents the first steps to create an orthogonal scaffold. First, a frame is designed, delimiting the scaffold size. The vertical line in the middle of Figure 4.15a represents the reference 0°. Then, a path is drawn with fibers running parallel to this reference line. Afterwards, a second path is drawn, with fibers rotated with the intended angle in relation to the reference line (90° in Figure 4.15).

Figure 4.16 shows the modifications to the layer represented in Figure 4.15c when the angle between successive layers is not 90°. In order to facilitate the design process, the short line segments parallel to the scaffold frame change automatically, to accommodate the change in rotation. So, when

the angle was changed, a continuous S shaped path would still be drawn, greatly expediting the construction of the fiber.

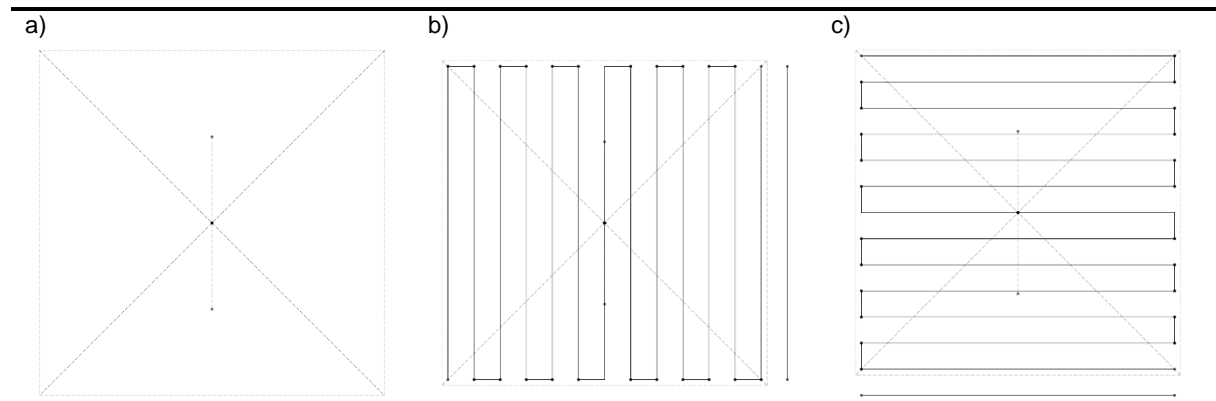


Figure 4.15 – Steps to create the S shaped fiber paths with 0-90° orientation: a) Quadrilateral delimiting final scaffold size. Short vertical line is the reference for layer rotations; b) S shaped path rotated 0° in relation to the reference line; c) S shaped path rotated 90° in relation to the reference line.

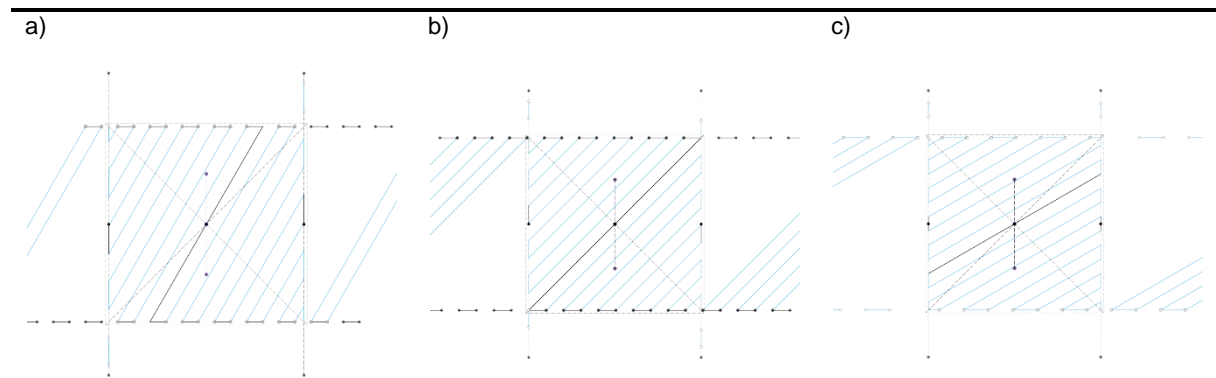


Figure 4.16 – S shaped fiber paths for non-orthogonal scaffolds: a) Path for 30° rotations; b) Path for 45° rotations; c) Path for 60° rotations.

Figure 4.17 and Figure 4.18 show the process to create the scaffold fibers from the paths in Figure 4.15 and Figure 4.16a, respectively. In the case of the orthogonal scaffold (Figure 4.17), the portions of the paths inside the delimiting frame were selected and the fibers were generated. Then, the two layers were copied to get the complete scaffold design. Figure 4.17d shows a picture of this scaffold manufactured in PCL, using the profile specified in section 3.4.1. In the case of non-orthogonal orientations (Figure 4.18), the process is exemplified with the 0-30° rotation, but it would be similar with other rotations. Again, the paths inside the delimiting frame were selected, and two fibers were created. Then, by copying these fibers and rotations of these fibers so that each layer was rotated 30° in relation to the previous, the complete scaffold was created.

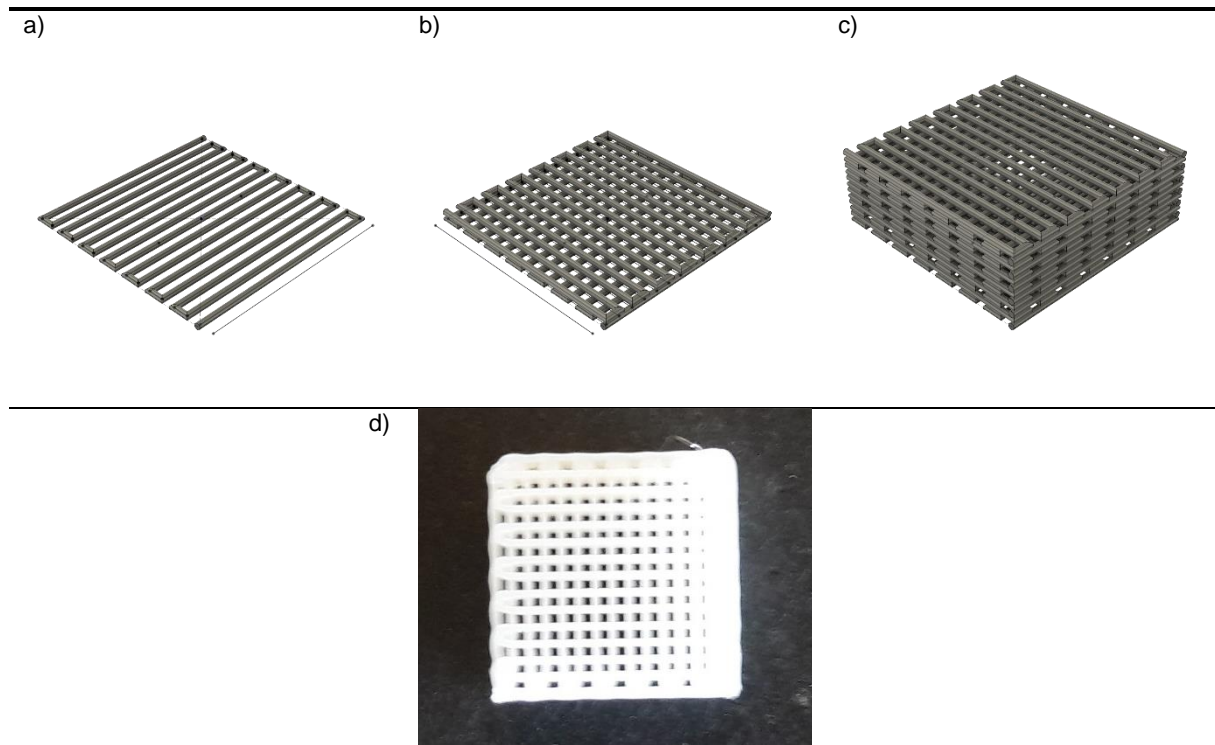


Figure 4.17 – Steps in the creation of a scaffold with 0-90° oriented fibers: a) 0° scaffold fiber; b) 90° scaffold fiber designed above the previous fiber; c) Scaffold model created by stacking copies of this fiber pair; d) Picture of FDM manufactured PCL scaffold.

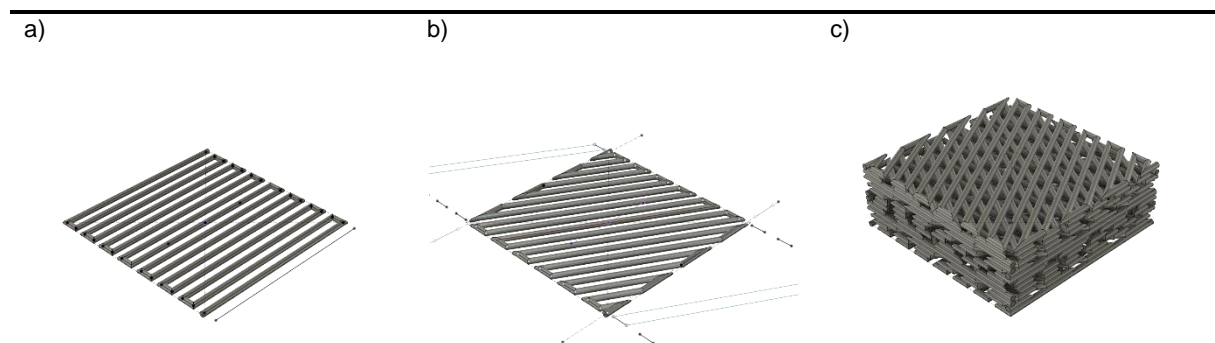


Figure 4.18 – Steps in the creation of a non-orthogonal scaffold (example with 0-30° oriented fibers): 0° scaffold fiber; b) 30° scaffold fiber designed above the previous fiber; c) Scaffold model created by stacking copies and rotations of copies of the previous two fibers.

Figure 4.19 shows a top view of the scaffolds with 0°-30°, 0°-45°, and 0°-60° fiber rotations, and also the result of manufacturing those scaffolds by FDM using PCL. The profile used was again the one described in section 3.4.1. Interestingly, only the scaffold with 0-60° fiber rotations presents a regular pattern, with the other two having a top view appearance that will never repeat itself. It could have some effects on the scaffold mechanical properties and on the behavior of the seeded cells, which could be interesting to evaluate.

The developed procedure could also be applied to create rotations with any other desired angle rotations. It would require the creation of more rotated layers in relation to the reference 0° since no



obvious symmetries would exist between layers, yet it would be feasible since the tracing of the fiber path, which is the step that takes longer, is already automated.

One feature could still be added to the process devised to create the scaffolds in Figure 4.19, which is the possibility of offsetting the layers along the x- or y-axis, in an amount between 0 and 1 pore distances. That modification would allow the creation of even further distinct scaffolds, and their different behavior could be studied, since previous works have already shown that layer offsets can influence mechanical properties and diffusion in scaffolds, as well as cell seeding efficiency<sup>106</sup>.

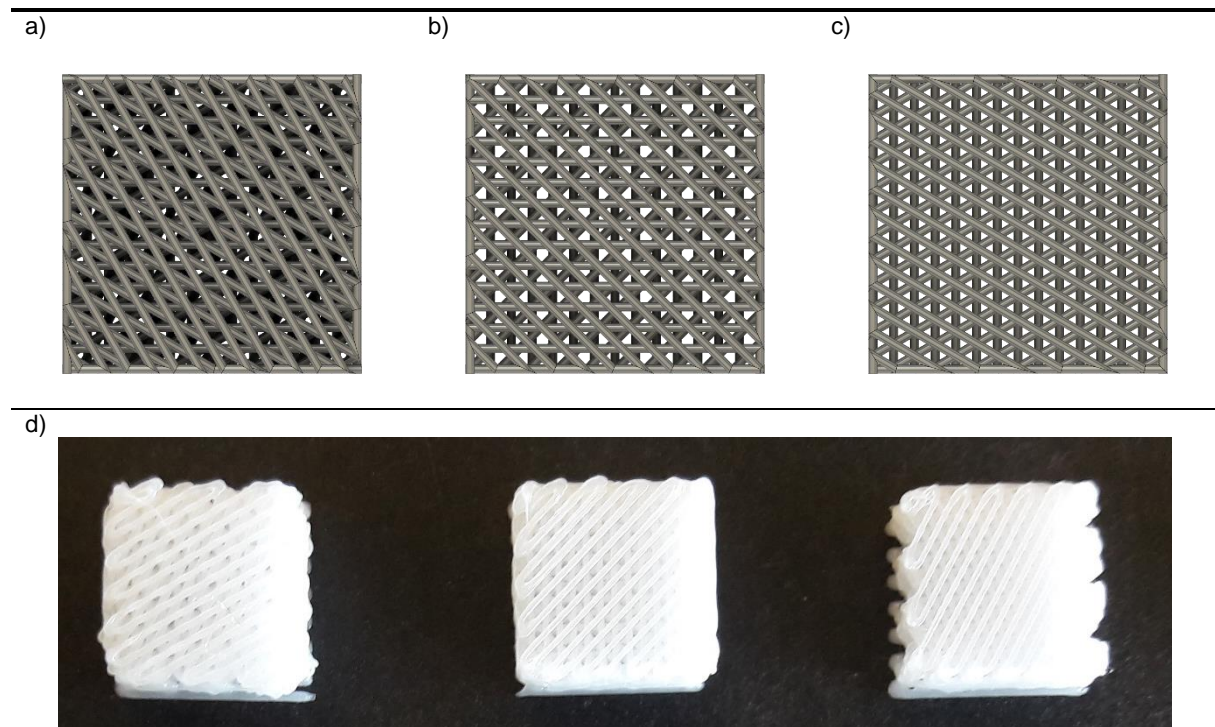


Figure 4.19 – Models and manufactured scaffolds with non-orthogonally oriented fibers: a) Model with 0-30° oriented fibers; b) Model with 0-45° oriented fibers; c) Model with 0-60° oriented fibers; d) Picture of FDM manufactured PCL scaffolds with layer rotation of, from left to right, 0-30°, 0-45°, and 0-60°.

#### 4.2.1.2. Pore size variation

To create scaffolds where, in each layer, there was a variation in pore size, the option provided by Fusion 360 of using a python script to make the design was preferred. Using the program's built-in geometrical operations, which were used to create models of all the other scaffolds, the design process would not be as straightforward. The code that was written is presented in Annex A.3.

As for previous models, some parameters were chosen to define the scaffold size and geometry, which are indicated in Table 4.3. Fiber diameter and layer height can be again independently defined, so that there could be an intersection between fibers in successive layers in the created model, not just a tangential contact. The other parameters define the desired pore dimensions at the edge and at the center of the scaffold along the x- and y-axis. The number of pores in these directions controls the size of the scaffold.



Table 4.3 – Parameters chosen to determine the size and geometry of scaffolds with pore size variation.

Parameter name	Description	Designed example
tubeWidth	Diameter of the scaffold fibers	0.3 mm
x_edgePore	Pore width at the edge of the scaffold in the x direction	0.15 mm
x_centrePore	Pore width at the center of the scaffold in the x direction	0.6 mm
x_nPores	Number of pores in the x direction (must be an odd number)	15
y_edgePore	Pore width at the edge of the scaffold in the y direction	0.15 mm
y_centrePore	Pore width at the center of the scaffold in the y direction	0.6 mm
y_nPores	Number of pores in the y direction (must be an odd number)	15
layerHeight	Determines the height difference between the layers	0.3 mm

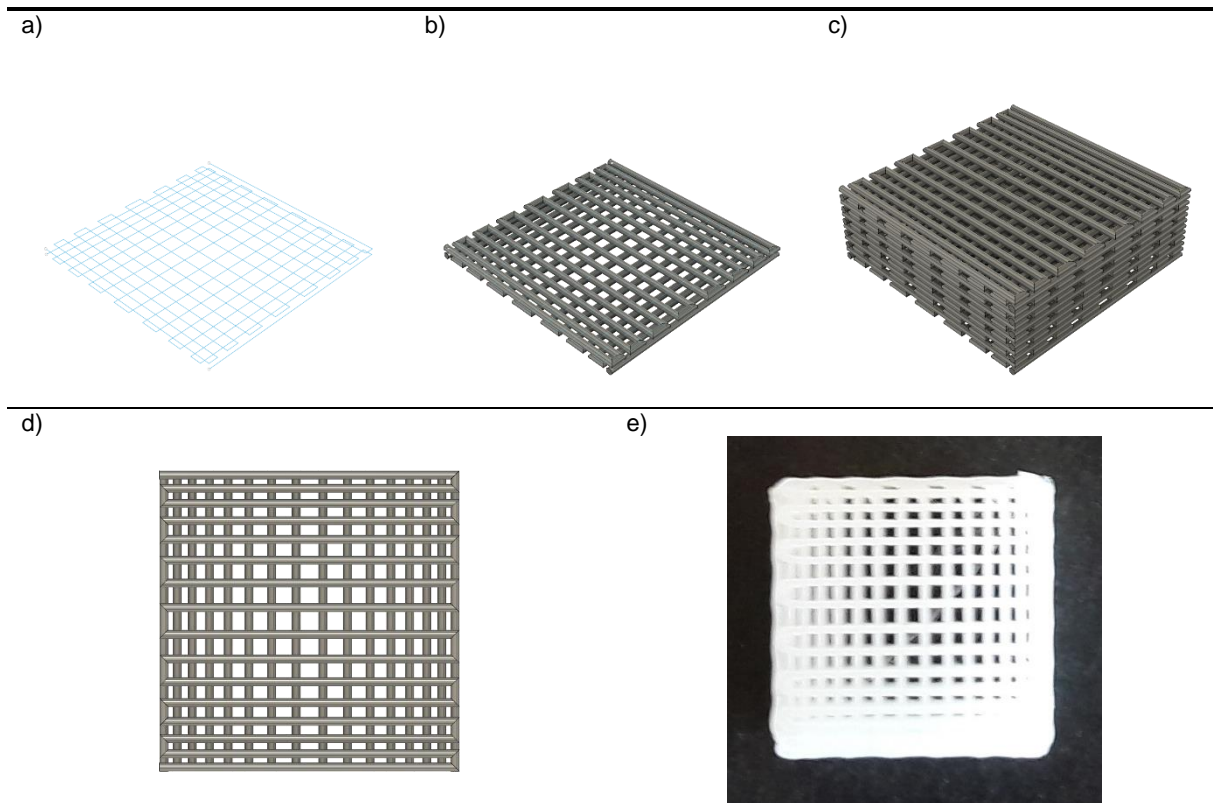


Figure 4.20 – Steps in the creation and manufacture of a scaffold with pore size variation: a) Paths of the first two layers of the scaffold; b) Creation of the scaffold fibers along those paths; c) Scaffold model created by stacking copies of this fiber pair; d) Scaffold model top view; e) Picture of FDM manufactured PCL scaffold with pore size variation.

The rationale to use a script to design these scaffolds was that in the Fusion 360 script environment there is a function that can connect two points with a straight line, and those lines can be connected to each other, creating a path. Thus, it was only a matter of defining functions that would calculate the coordinates of the points to be connected. Two functions were defined. The first calculated all pore dimensions along one axis, given the pore sizes at the edge and center of the scaffolds and the number of pores desired. The other calculated the coordinate of the center of the fibers, parallel to a given axis. Then, by calculating the length the fibers would have, a path could be traced. Figure 4.20a-c exemplifies the procedure to create a scaffold with pore size variation. After the paths for two layers are created by

running the script, fibers are created following those paths and then copied to create the final scaffold design. Different designs can quickly be created by changing the parameters and repeating these simple operations.

Figure 4.20d shows a top view of the designed scaffolds and Figure 4.20c shows a picture of that scaffold manufactured by FDM with PCL. The profile used was the one described in section 3.4.1. At the time the functions that calculated the coordinates of the center of the fibers were written, they only accounted for an odd number of pores, for simplicity. So, one improvement could still be made in this procedure, which was to allow the design of layers with an even number of pores.

#### 4.2.1.3. Scaffolds with pore gradient along the layers

As described in section 2.2.1, pore morphology can have an influence on cell behavior and provide conditions more favorable for either osteogenic or chondrogenic differentiation. Smaller pores have been shown to favor chondrogenesis, while larger pores would favor osteogenesis<sup>131–133</sup>. The purpose was then established to create a process which would allow the design of a scaffold with layers exhibiting a pore size gradient. To accomplish this objective, either of the designs described in sections 4.1.1 or 4.2.1.1 could be used. Each section of the scaffold would be created independently, and then all joined together. In the particular case of the scaffold shown next, the process described in 4.2.1.1 was followed.

The scaffold to be designed should have three sections with different pore sizes. Typical values were chosen for its dimensions, specifically 0.3 mm for the fiber diameter, for the chondrogenic side a pore size of 0.15 mm was chosen, and for the osteogenic side a pore size of 0.6 mm was chosen. These pore dimensions were also conveniently chosen so that both sections could have the same width: with 23 parallel segments in the chondrogenic section and 12 parallel segments in the osteogenic section, both create a scaffold with a width of 10.2 mm. So, for the middle section, an intermediate pore dimension was chosen in order to have a section with approximately the same width. The middle section was then designed to have pores with 0.28235 mm and composed by 18 parallel segments. Figure 4.21a and Figure 4.21b show, respectively, a top view and a cross-section of the created model. Figure 4.21c shows a side picture of the side of this model, manufactured by FDM using PCL. The printing profile used was the one described in section 3.4.1.

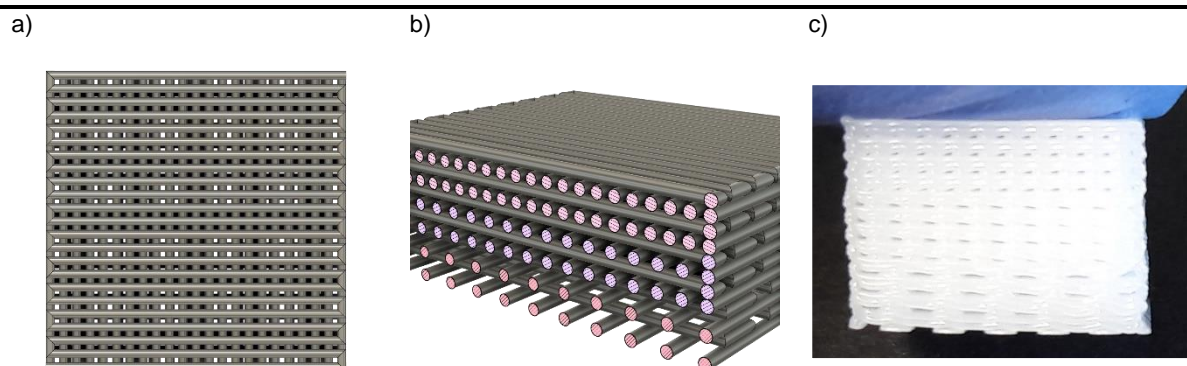


Figure 4.21 – Model and manufactured scaffold with pore gradient along the layers: a) Scaffold model top view; b) Scaffold cross-section; c) Picture of FDM manufactured PCL scaffold with pore gradient along the layers.

#### 4.2.2. Manufacturing a scaffold mimicking the knee medial condyle surface

To explore the possibility granted by FDM of creating personalized constructs, that can mimic in some extent the native tissues, a scaffold was also developed reproducing the OC tissue structure. The area of interest to be constructed was selected after a discussion with the medical doctor Nuno Ribeiro (Hospital dos Lusíadas, Lisboa), an orthopedic surgeon specialized in the knee joint. According to him, the most commonly damaged OC region in the knee joint, accounting for around 80% of his surgical procedures, is the load bearing regions of the femur medial condyle. Several kinds of procedures can be performed, according to the severity of the lesion, however none of the currently available treatments, including the ones involving scaffolds, provide a completely satisfactory outcome<sup>1</sup>. For these reasons, this region was chosen to be modeled and reconstructed. A model of a human femur, created from medical imaging was downloaded and a section was cut in the medial condyle with 20 mm × 14 mm. A convenient size for a scaffold for interventions in this region would be, according to Dr. Nuno Ribeiro, 20 mm × 20 mm. Since a cut with this size would extend past the cartilage covered region, the cut was made to be as close as possible to this favored dimension. Figure 4.22 shows the area where the section was cut and a close-up view of that section.

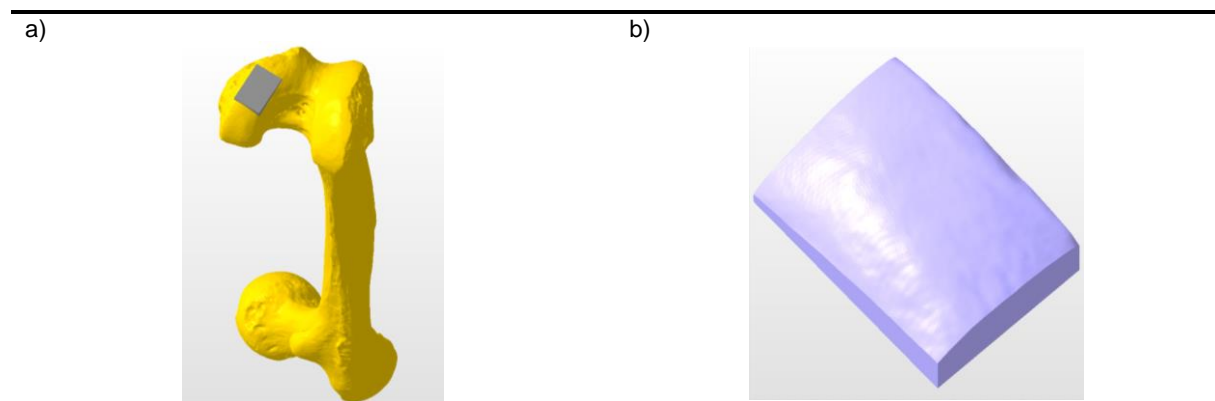


Figure 4.22 – Section of the femur medial condyle to be mimicked by a scaffold a) 20 mm × 14 mm section of interest to be replicated; b) Close-up view of the section.

Figure 4.23 illustrates the procedure to create a scaffold from the section cut from the medial condyle. Typical dimensions were chosen for the creation of the scaffold, so layer height, pore, and fiber dimension were all chosen to be 0.3 mm. To create the scaffold, plane cuts with 0.3 mm intervals were made, and on each plane cut an S shaped path was drawn, with the edges following the irregularity of the cut. These paths would then be used to create the fibers in every plane (rotated 90° in consecutive planes). The scaffold was then created joining all layers (Figure 4.23c).

Since it was considered that there was an interest in simulating computationally the mechanical behavior of this scaffold in COMSOL, some modifications were made to accommodate a simulation. In Figure 4.23d, the edges that followed the irregularity of the cut became straight lines, and in Figure 4.23e those edges were completely removed. In this last case, the height of the scaffold fibers was increased while layer height remained the same so that fibers would intersect, and a fillet was added to every edge. This would be the most convenient format to run the simulation. However, all models were

extremely complex, which limited the possibility of obtaining such simulations within the timeframe of this thesis.

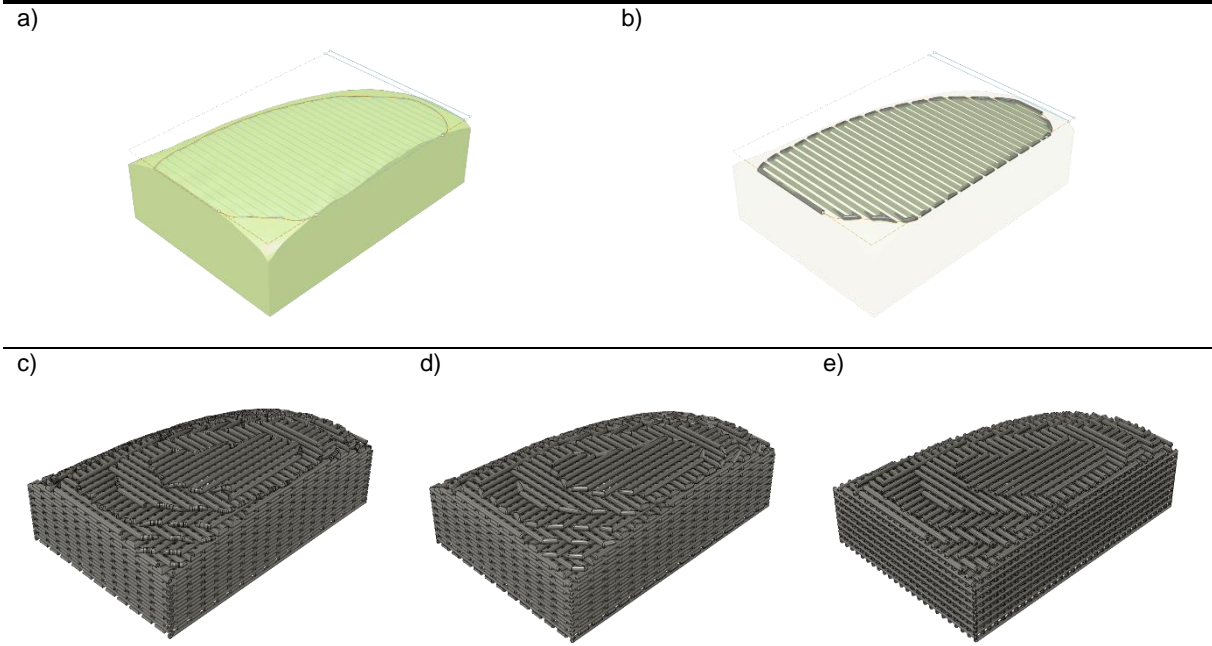


Figure 4.23 – Steps in the reconstruction of a section of a femur medial condyle to be manufactured by FDM: a) Representative layer cut with traced fiber path; b) Scaffold fiber created following the previous path; c- e) Designed scaffolds, replicating the process shown in a-b) for the entire section of the medial condyle, with fibers in successive layers perpendicular to each other. The connections between parallel segments in each layer: c) follow the cut in a); d) are straight segments; e) are not connected.

Figure 4.24 shows the scaffold from Figure 4.23e manufactured by FDM using PCL. It also shows how it could fit the damaged area and providing a surface that would follow the native curvature of the tissue.

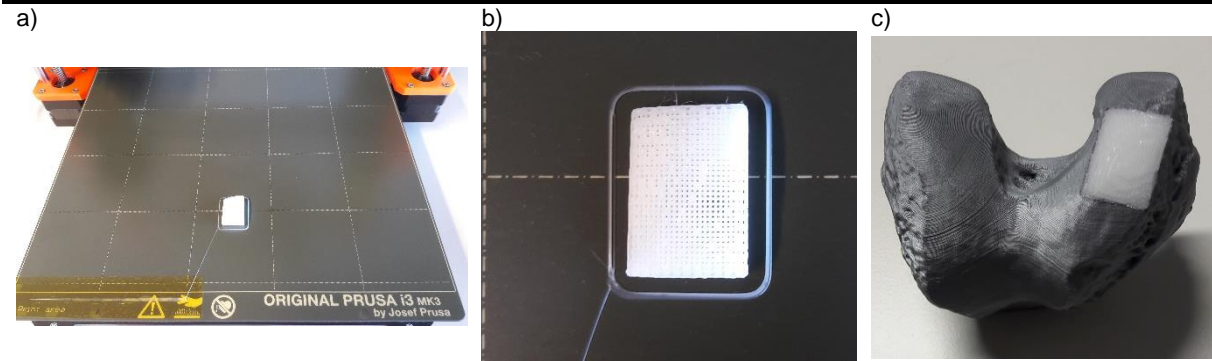


Figure 4.24 – FDM manufactured PCL scaffold mimicking a section of the femur medial condyle, corresponding to the model in Figure 4.23 e): a) Printed scaffold; b) Close-up view; c) Scaffold fitting the cut in the medial condyle and following the native curvature of the tissue.

Besides the possibility of adapting the scaffold to personalized therapeutic strategies, a particular advantage of fabricating this reconstruction by FDM is that it consents the correction of areas with defects. If a reconstruction has to be made with medical imaging of a region that contains a defected area, the obtained model can be digitally manipulated to repair it and have a final construct with the convenient shape.

#### 4.2.3. Design of a double-chamber platform for the study of osteochondral tissue differentiation

Another conceived strategy for the development of constructs replicating the whole OC unit was the creation of a reactor, in which scaffolds could be introduced, and each side would be in contact with a different induction media, one for chondrogenic differentiation, and the other for osteogenic differentiation. A simple preliminary design was created, comprised of a vessel, in which a partition would be slotted, dividing the vessel into two chambers. The partition would incorporate a scaffold in the middle. On top, a lid was added to strengthen the structure. All parts were manufactured by FDM. One design constrain was considered, which was that this vessel would need to fit inside a 12-well culture plate.

The design and manufacture of this pilot reactor is shown in Annex A.4, as the result of the conducted tests. Introducing only water in one of the chambers, at room temperature, no leaks were observed, and the water remained in the chamber until it evaporated. However, when introducing Dulbecco's Modified Eagle Medium (DMEM) in one chamber and placing it in an incubator at 37°C, the medium quickly started to infiltrate through the printed layers and leaked from the vessel, which indicates the need for further optimization. One proposed solution to the infiltration problem, which has already been shown to be effective<sup>134</sup>, was the coating of the parts with a thin layer of poly(dimethylsiloxane) (PDMS). Another possible solution was the fabrication of the parts with a different polymer (acrylonitrile butadiene styrene (ABS) or acrylonitrile styrene acrylate (ASA)), which could be chemically treated with acetone vapor to seal the gaps between the layers.

Still, it was considered that the reactor design still required improvements regarding hermetic sealing, and these proposed solutions to the leaking were not tested. Since this thesis work was also moving towards other objectives, further development of this reactor was deferred to a later moment in time.

### 4.3. Mathematical approach for a curved scaffold design

In recent years, AM has introduced new possibilities to the field of TE, owing to the better control over the design and manufacturing process of scaffold structures<sup>78,135</sup>. Using medical imaging techniques like magnetic resonance imaging (MRI) and computer tomography (CT) to obtain 3D models of tissues and processing them via CAD software is expected to allow the creation of constructs reproducing the correct shape of tissues and also able to be patient-specific to fit individual defects<sup>104,136,137</sup>. Despite some advances, there are still some limitations in the available materials matching native tissue properties and challenges in the scaffold biofabrication to reproduce tissue internal fibers orientation that need to be met before this procedure achieves a more widespread use<sup>32,137</sup>.

Considering scaffolds specifically for OC TE, most constructs described in the literature have a cuboid or a cylindrical shape (e.g., references <sup>138-141</sup>). As seen previously in section 4.2.2, native tissue displays a curved surface and, furthermore, in load-bearing tissues if loads are not evenly distributed scaffold constructs may have a worse performance in the regions exposed to higher loads.



With the aim of determining if a curved scaffold could be manufactured by FDM to address the previously mentioned issues, an experimental curved model was developed with an arbitrary curvature (Figure 4.25). The surfaces to be curved would correspond to the top and bottom surfaces, with larger area, of the conventional orthogonal scaffolds. Due to its rounded shape, some modifications needed to be made in the design and manufacturing process, in relation to the non-curved scaffolds presented previously in this work. Therefore, the changes implemented to produce this scaffold by FDM were:

i) The scaffold would need to be printed supported on one of its smaller sides. If it were to be printed on the top or bottom, due to the curvature, the printing would necessarily have to include supports which, at the scale of these prints, would be very difficult to remove, easily create weaker points in the structure during its removal, leave scars at the points where they contacted the scaffold, and probably lead to distortions in the printed construct. In the design process, supports are not actually in contact with the object to be printed. There is a small gap between the object and the support, so that when the filament with which the object is being printed cools, it only establishes a slight contact with the support and a weak adhesion is created between them. Otherwise, their separation would not be possible. So, in the parts where molten filament would be deposited mid-air, the filament would fall or be dragged, and its location would not match what was modeled;

ii) The base of the scaffold would need to be flat. Since support structures had been ruled out, a flat base is needed to have enough adhesion between the build plate and the object while being printed;

iii) In the design process, so that it would be feasible to create a scaffold, many symmetry operations were employed, in a way that the scaffold would have a top projected quadrilateral shape;

iv) To ensure that perfusion would occur between the top and bottom of the scaffold, the traditional “S” shaped filament lay down pattern was changed. From side to side, filament continued to be deposited in an “S” shape. From top to bottom, filament would be deposited in parallel segments.

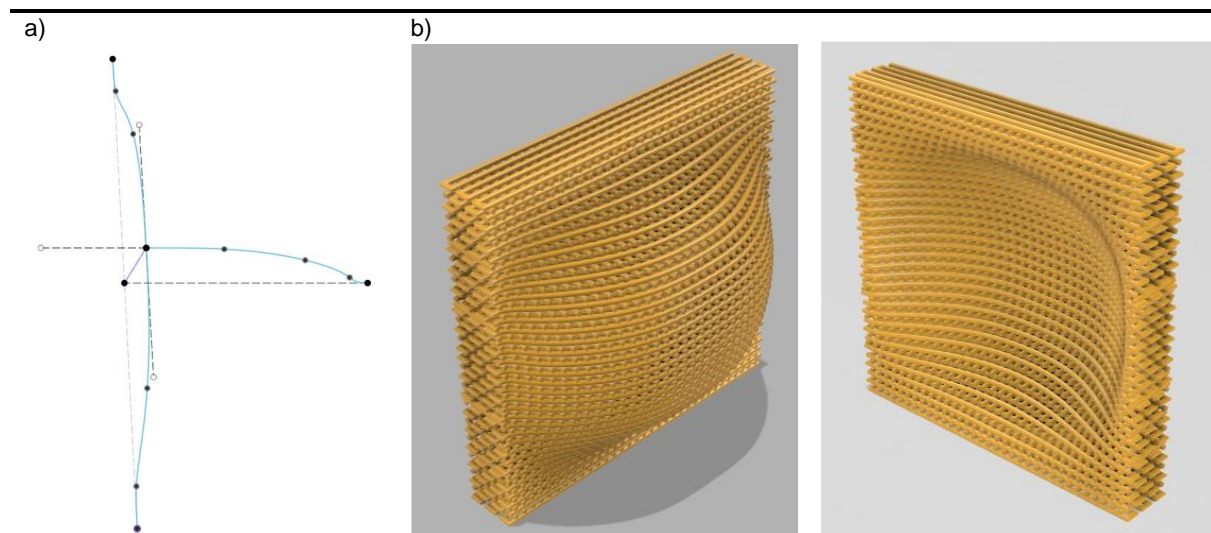


Figure 4.25 – Experimental curved surface scaffold with an arbitrary curvature: a) Profile of the curved surfaces of the scaffold, with two axis of symmetry; b) Top and bottom views of the modeled scaffold.

Considering the dimensions, at this early stage, typical pore and filament dimensions were chosen that could be compatible with OC tissue constructs and also simplify the design process. For these reasons, both the pore size and the filament width in the scaffolds were chosen to be  $300\ \mu\text{m}$ <sup>130,142</sup>.

Concerning the side length, the dimension referred in section 4.2.2 was again chosen, so that it could be representative of constructs for surgical procedures in the knee OC region. The scaffold was then modeled with a base length of 20.3 mm, a height of 20.1 mm and a thickness of 3.3 mm. As one of the first prints made, this model was constructed with the printer still equipped with the 0.4 mm nozzle and using conductive PLA. Again, as stated in section 3.2, the default “0.15 mm QUALITY”, “Prusament PLA” and “Original Prusa i3 MK3S & MK3S+” profiles were used, but with the following modifications: in the print settings, layer height and first layer height set to 0.3 mm, detect thin walls option checked, minimum of 3 loops in the skirt, all printing and non-printing moves set to 8 mm/s, all extrusion widths set to 0.35 mm, the slice gap closing radius set to 0.018 mm, elephant foot compensation set to 0 mm; in the filament settings, fan was set at full speed in layer 1; in the printer settings, no changes were made. Figure 4.26 shows details from top and bottom of the printed scaffold.

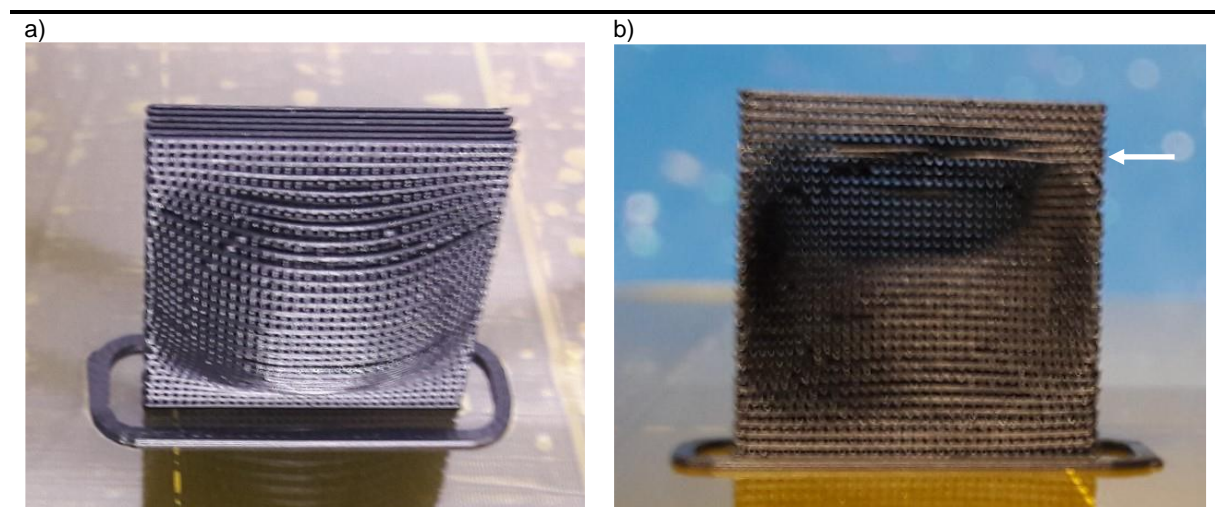


Figure 4.26 – Pictures of an experimental curved scaffold, with arbitrary curvature, manufactured by FDM using conductive PLA filament: a) Top view; b) Bottom view. White arrow points to the height of separated filaments.

Figure 4.26 shows a good quality print, particularly taking into consideration that it was printed with the 0.4 mm nozzle and with a filament width deposition smaller than the nozzle diameter, which is not recommended. Apart from some blobs on the scaffold surface, no other major printer flaws were observed. In Figure 4.26b a flaw resulting from the scaffold geometry can be detected (white arrow). Near the top of the picture, a string of filament is seen separated from the scaffold. It resulted from the fact that this string was printed mid-air, without contacting any material beneath it and with the printhead moving in a curved motion. These results showed that it was possible to print curved scaffolds, but that particular attention should be given to the geometry, so that no overhangs would be created.

#### 4.3.1. Model development

Having established that curved scaffolds could be printed by FDM, it was decided to remake the model, but in a way that the curvature could be quantifiable. The simpler and more obvious hypothesis was to think of a scaffold which curvature would follow a cutout of the surface of a sphere. Then, the radius of that sphere would give a measure of the curvature of the scaffold. Other decisions were also taken in the beginning to simplify the design development, such as:

i) In order to allow the fabrication of as many scaffolds as wanted could be created, the design would need to be parametric. This way, a procedure to create scaffolds would be devised and then it would only be a matter of choosing the value of the radius variable, and the modeling software would redraw the entire scaffold;

ii) As in the experimental curved scaffold, there would be an axis of symmetry in the designed scaffold. Thus, only one quarter of the scaffold would need to be drawn, saving considerable time, and significantly reducing the complexity of the design. Through symmetry operations the whole scaffold would be created;

iii) The fibers of the scaffold would no longer be connected, which means that the “S” shape lay-down pattern would not be used in any layer. This was necessary so that the symmetry operations referred previously could be used, and to reduce model complexity for the computational simulation of mechanical behavior of the scaffolds;

iv) Concerning dimensions, the filament width and the pores of the scaffolds would be 300  $\mu\text{m}$  wide. Scaffold thickness would be around 3 mm, which means that in the layers with curved filaments, there would be six fibers in each layer. The scaffold would have a top projected square shape, with a 20.1 mm side.

The model that was developed allowed intentionally a very direct way to change the curvature of the scaffolds, by simply changing the value of one parameter in Fusion 360. Other dimensions like size, pore, and filament size could conceivably be changed, but it would be more cumbersome. However, the main purpose of this model was only to directly change the curvature.

Figure 4.27 shows the contour that the scaffolds must follow. Figure 4.28 and Figure 4.29 show the steps in Fusion 360 to create scaffolds with this contour. Two strategies were elected to give the scaffold its thickness. In the first one, designated constant radius, all curved surfaces used to trace the path of scaffold fibers have the same radius (Figure 4.28). This means that the dark grey surfaces in Figure 4.28d are equal, with one translated in relation to the other. The scaffold will be limited between those two surfaces; while in the second one, designated concentric radius, a series of concentric curves are used to trace the path of scaffold fibers (Figure 4.29). This means that the dark grey surfaces in Figure 4.29b, c, and f have different radii and are concentric. The radius of the innermost surface is the one that defines the curvature of the scaffold.

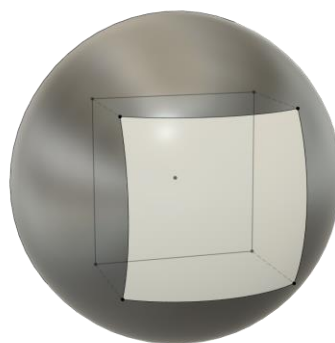


*Figure 4.27 –Contour intended for the surface of curved scaffolds, represented by the bright area. The curvature is defined by the sphere radius. Projected square shape has a 20.1 mm side.*



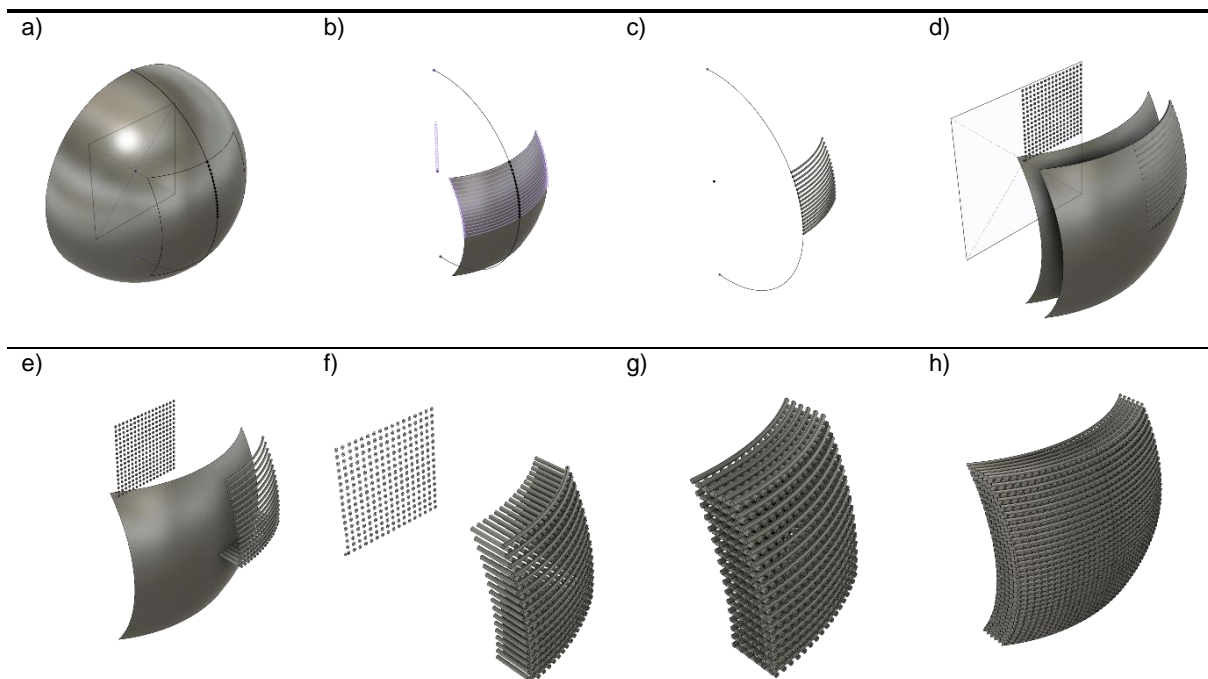


Figure 4.28 – Illustration of the steps in the design of a curved scaffold in Fusion 360, with constant radii surfaces tracing the path of curved fibers of the scaffold.

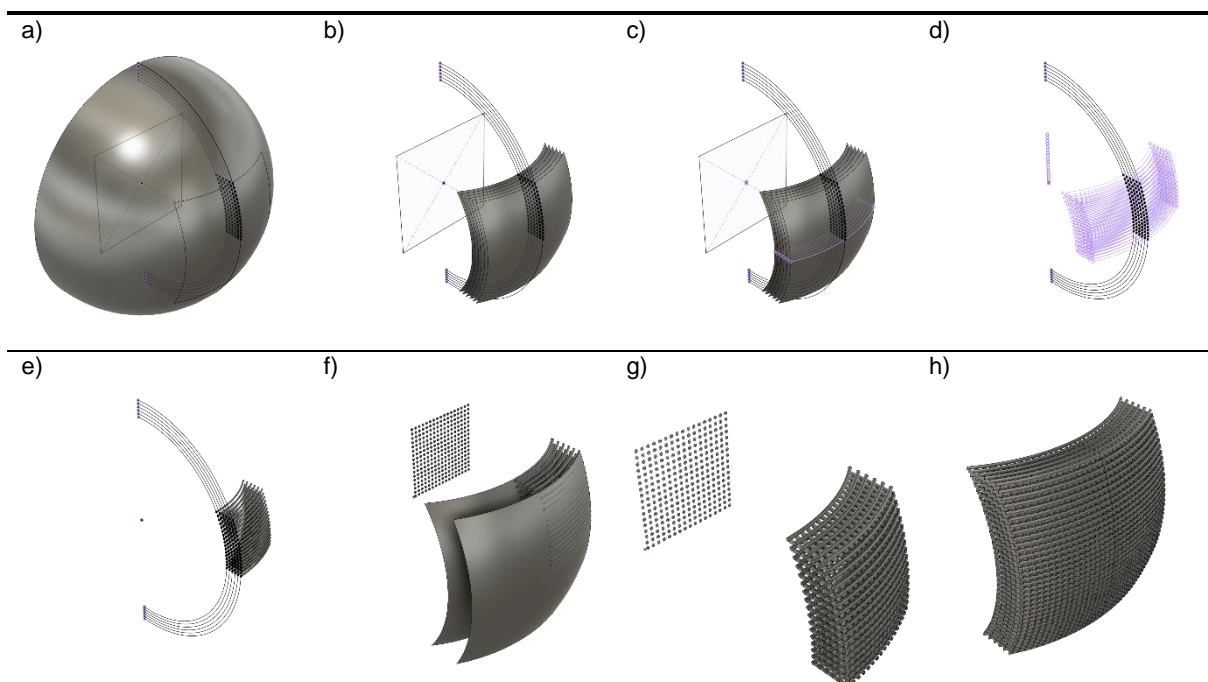


Figure 4.29 – Illustration of the steps in the design of a curved scaffold in Fusion 360, with concentric radii surfaces tracing the path of curved fibers of the scaffold.

The constant radius strategy starts by delineating the scaffold contour on a sphere surface, making a cutout (Figure 4.28a). Then, the positions of the curved fibers of the scaffold are marked on that cutout and extruded between the scaffold centerline and its edge (Figure 4.28b-c). The position of the fibers passing from the bottom to the top of the scaffold is defined and the fibers extruded between the top and bottom surfaces delimiting the scaffold thickness (Figure 4.28d-f). Afterwards, the curved fibers of

the scaffold are replicated between those two surfaces delimiting the scaffold (Figure 4.28g). Finally, one quarter of the scaffold has been built, and two symmetry operations create the complete scaffold (Figure 4.28h).

The concentric radius strategy starts by creating a series of concentric spheres and making a cutout in all of them corresponding to the size of the scaffold (Figure 4.29a). The positions of the curved fibers of the scaffold are marked on those cutouts (Figure 4.29b-d) and extruded between the scaffold centerline and its edge (Figure 4.29e). Then, the position of the fibers running from the bottom to the top of the scaffold is defined and the fibers extruded between the top and bottom surfaces that delimit the scaffold thickness (Figure 4.29f-g). Finally, one quarter of the scaffold has been built, and two symmetry operations create the complete scaffold (Figure 4.29h).

### 4.3.2. Method to determine maximum curvature of FDM printable scaffolds

Having a method to design scaffolds with any arbitrary curvature, the question then becomes to assess the possibility of manufacturing them by FDM. Increasing the curvature, the print will be closer to the situation where the filament being deposited will not be supported by the layer underneath, in which case the print will fail.

Regarding the designed scaffolds, this possibility of lack of support will be more pressing closer to the base and the top of the printed object, where the printing slope is higher (Figure 4.30a). Closer to the center of the scaffold, layers will be deposited almost vertically on top of each other, and the lack of support will not be an issue. Even though the curvature is the same throughout the scaffold, the problem will predictably only be seen at the base and top of the printed object.

The design objective then became to determine the curvature at which, in the extremities of the scaffold, there would be the bare minimum contact between adjacent layers. Mathematically, this translated into having a tangential alignment between the walls of deposited filaments in consecutive layers (Figure 4.30b). The maximum distance between scaffold fibers then corresponds to the minimum contact. In Figure 4.30b, the bottom fiber represents fibers parallel to the plane of this page, and the top fiber represents fibers perpendicular to the plane of this page.

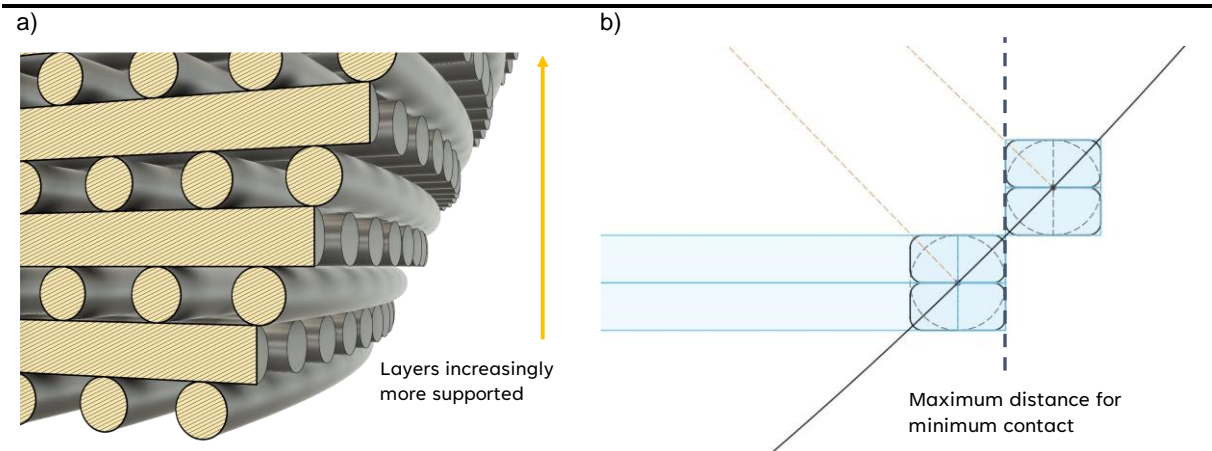


Figure 4.30 – Design objective to determine the maximum curvature of an FDM printed scaffold. a) Cross-section, through the middle of the scaffold, observing decreased layer support closer to the base of the print; b) Minimum contact between adjacent layers when maximum curvature is reached.



$$\begin{cases} distance = R(\cos \alpha - \cos \beta) \\ R(\sin \beta - \sin \alpha) = 2 \times 0.15 \\ R \sin \beta = L - 0.15 \end{cases} \quad 4.1$$

Two strategies were used to calculate  $R$ : one graphical using Fusion 360, and one analytical using Mathematica 12.3. In Fusion 360, if all dimensions are constrained and there are no degrees of freedom, the values of dependent variables can be obtained. Using Mathematica, the solution was obtained evaluating expression 4.2 and choosing the answer with positive values. Both strategies returned the same solutions, which are shown in Table 4.4.

$$\begin{aligned} \text{Solve}\{r((\text{Sin}[b]) - (\text{Sin}[a])) == 2 * 0.15, 0.15 + 0.15 = \\ = r(\text{Cos}[a] - \text{Cos}[b]), r(\text{Sin}[b]) == 10.05 - 0.15\}, \{a, b, r\} \end{aligned} \quad 4.2$$

Even though Equations in 4.1 were only used to calculate  $R$  with given values to  $distance$  and  $L$ , the system can be used to solve for other variables as well. For example, if a radius  $R$  and a height  $L$  have already been chosen, it would be possible to calculate how much the fibers would overlap. Also, if a radius  $R$  and the overlap  $distance$  have been chosen, the height  $L$  of the scaffold can be calculated. As long as values are assigned to two variables, it will be possible to find a solution for the other three variables.

Table 4.4 – Solution to Equations in 4.1 that describe mathematically the problem formulated in Figure 4.31, calculating the most extreme curvature for a scaffold to be manufactured by FDM.

Assigned parameters	Solution
$distance = 0.3 \text{ mm}$	$R = 13.7902 \text{ mm}$
$L = 10.05 \text{ mm}$	$\alpha = 44.1186^\circ$
	$\beta = 45.8814^\circ$

The previous deduction for  $R$  applies to the radius of circles parallel to the ones in Figure 4.32, the same as the orientation of the cut in Figure 4.30. This was the intent of the deduction: to determine what was the smallest radius these circles could have. It can be seen that towards the edges the radius is smaller, compared to the radius through the middle of the scaffold. The extreme calculated case corresponds to the circles on the edge. So, if for example the scaffold were to be wider, in a way that it could be manufactured by FDM, its surface would need to be straighter.

To find the radius of the circle through the middle of the scaffold, which is also the radius of the sphere defining the surface curvature of the scaffold, the Pythagorean theorem can be used (Figure 4.32). The calculated sphere radius is 17.064 mm. Table 4.5 summarizes the dimensions that characterize the scaffold.

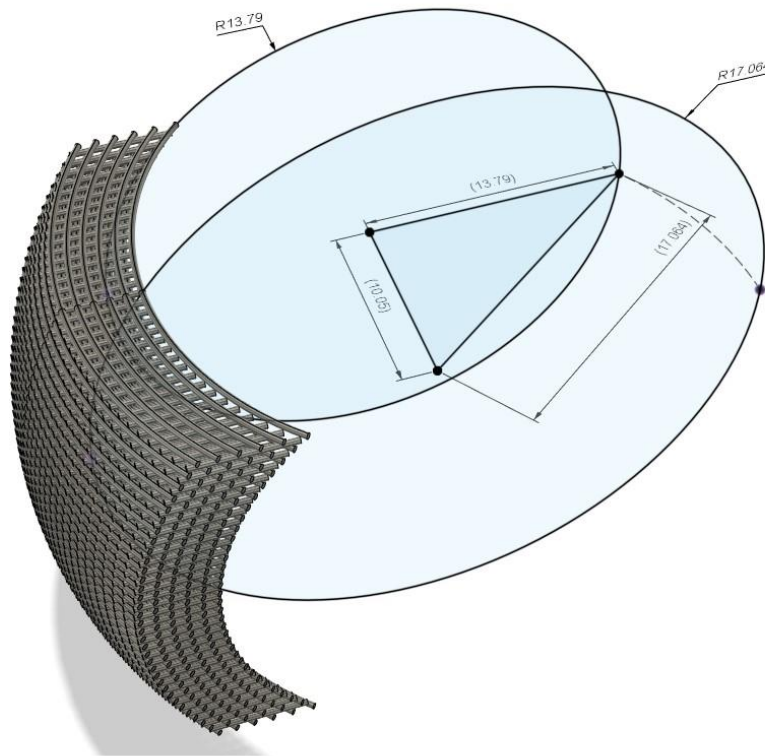


Figure 4.32 – Calculation of the sphere radius (17.064 mm) defining scaffold surface curvature from the radius calculated to provide minimum support between scaffold fibers (13.7902 mm).

Table 4.5 – Summary of deducted curved scaffold dimensions that provide minimum support between scaffold fibers.

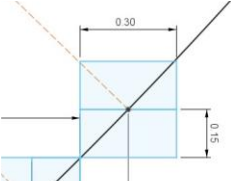
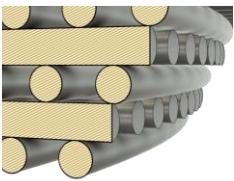
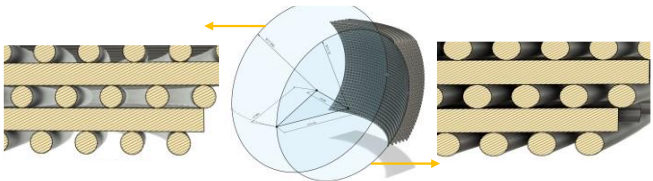
Scaffold dimension	
Height	20.1 mm
Width	20.1 mm
Scaffold fiber height	300 $\mu\text{m}$
Overlap between scaffold fibers ( <i>distance</i> )	300 $\mu\text{m}$
Radius of sphere characterizing surface curvature	17.064 mm

In order to reach this result for the radius of the sphere, some important assumptions were made during the deduction, which are summarized in Table 4.6. The first is that during the printing process it will be possible to always maintain an extrusion width of 0.3 mm, which might not always be possible in FDM due to small variations in pressure at the end of the nozzle or dragging of the filament. However, it is being assumed a perfect layer deposition. The second is that no overhangs are created. This means that the amount of filament hanging is so small that it does not create any sag. The third is that the different fiber orientation in the scaffold cuts will not impact the previous deduction.

Having an automated method to create curved scaffolds and after determining a limit curvature for the manufacture of scaffolds, six different designs were created to confirm assumptions and to test the scaffolds. The radii of curvature selected were the limit radii calculated, two smaller radii, and three larger radii. The two strategies referred in section 4.3.1 were used, one in which the curved fibers of the scaffold are concentric, and another in which the radius of those fibers is constant. The models are depicted in Figure 4.33 and in Figure 4.34, respectively.



Table 4.6 – Assumptions in the deduction of curved scaffold dimensions that provide minimum support between scaffold fibers.

		
<p>Extrusion width is always 0.3 mm.</p>	<p>At the small scales being printed, if the filament is minimally supported, it does not create overhangs.</p>	<p>Angle between fiber orientation varies between the center and the edge of the scaffolds. This variation is not considered relevant.</p>

Analyzing the designs in Figure 4.33 and in Figure 4.34, it can be seen that, in the designs with radius of 12 mm and 14 mm, some fibers at the base and top of the model do not actually have contact with the rest of the part. For that reason, those fibers should not be printed correctly. In the designs with the radius of 17.064 mm, there is the slightest contact between some fibers at the base and top of the model and will possibly be weak points of the prints. In designs with increasing radii, the contact between fibers is increasingly larger and so it is expected a better adhesion between all fibers in the print.

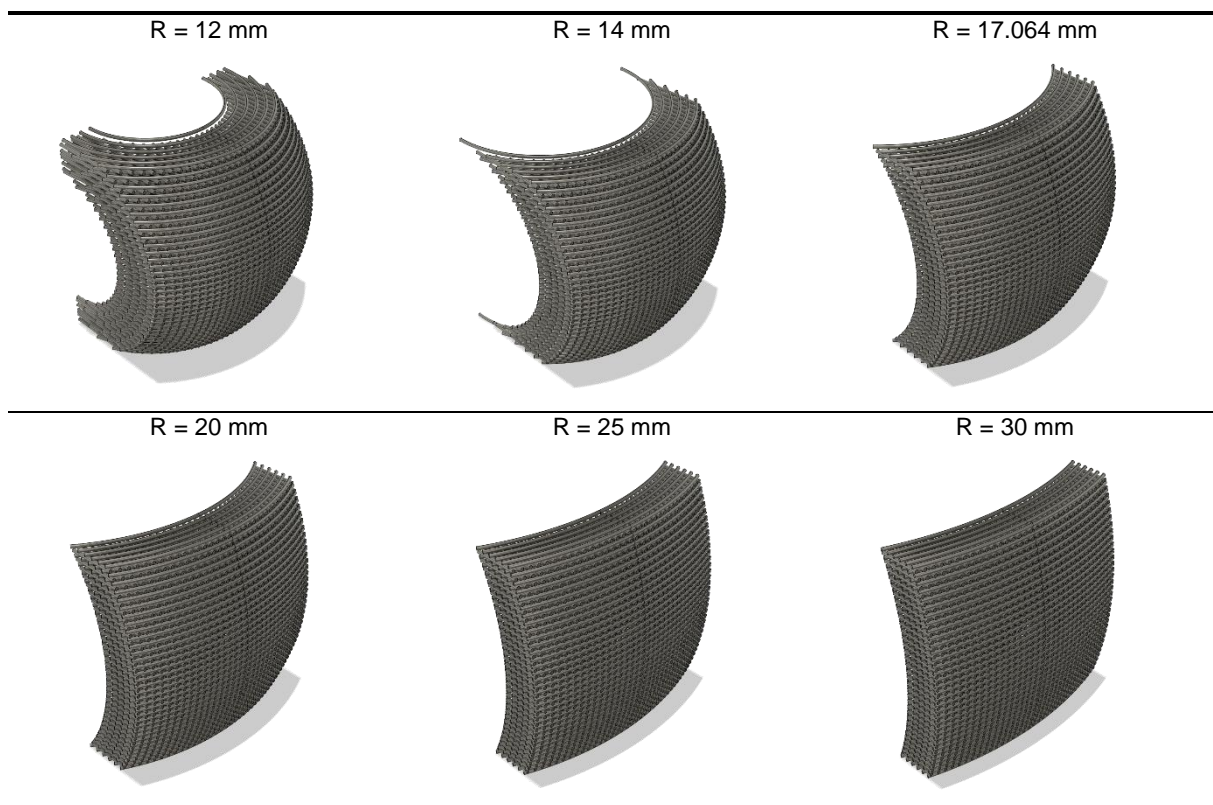


Figure 4.33 – Designed curved scaffolds with concentric radius surfaces.

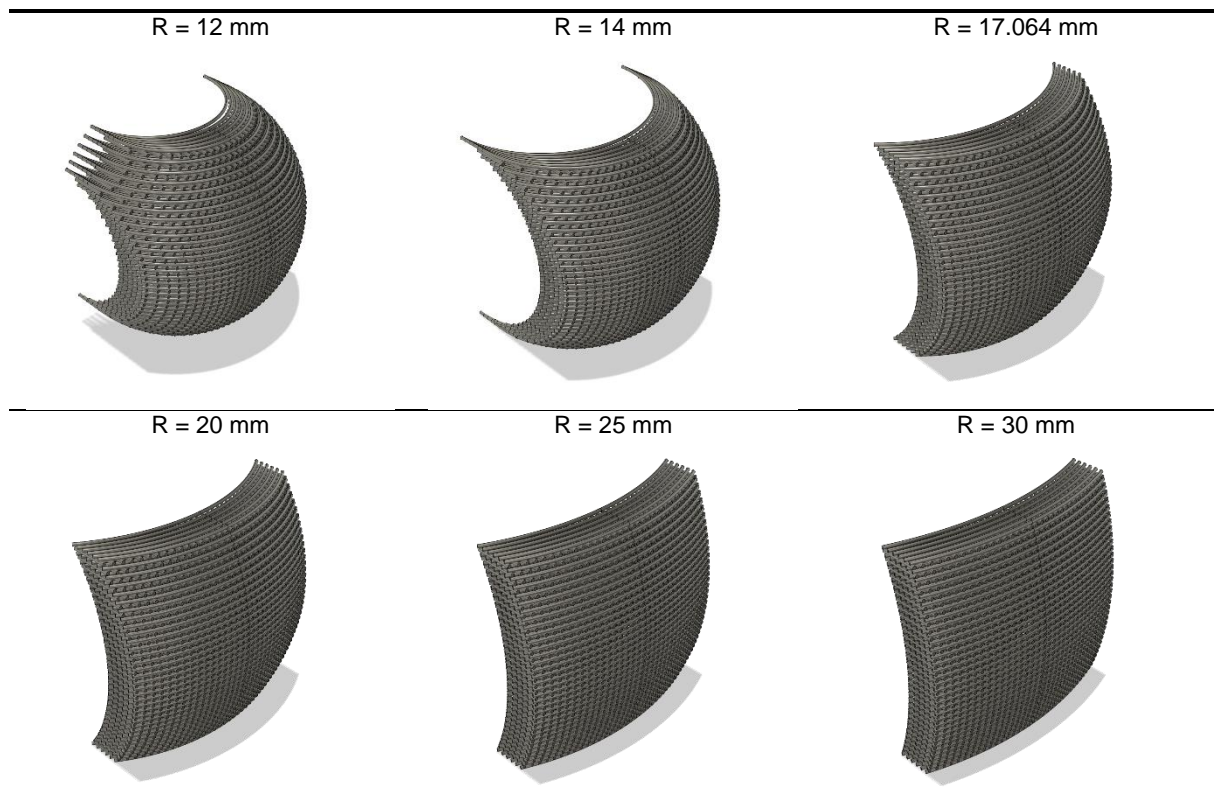


Figure 4.34 – Designed curved scaffolds with constant radius surfaces.

As described in section 4.3.1, the two strategies used to generate the thickness dimension of the scaffold (concentric and constant radius strategies) have consequences on their overall shape and pore dimensions, which are elucidated in Table 4.7. The top layers of the 20 mm scaffolds are represented because in that layer the effects are more noticeable. It is apparent, with the concentric strategy, that the thickness of the scaffold is greater at the edges than at the center. On the contrary, with the constant strategy, the thickness is smaller at the edges than at the center. Due to that variation, the projected pore area on the top layer increases towards the edges with the concentric strategy and decreases towards the edges with the constant strategy. This variation is a direct necessary consequence of how the curved spherical surfaces are defined and is intrinsic to both strategies. This consequence was exemplified for the 20 mm radius scaffolds. Still, the same consequences would be seen in the scaffolds with other radii. The variations would be more pronounced in scaffolds defined by smaller radii, and less pronounced in scaffolds defined by larger radii, since their shape would be getting closer to a straight orthogonal scaffold.

Comparing two scaffolds with the same radius but built with different strategies, they will be equal at the center of the scaffold. As pore size is measured towards the sides and also to the top and bottom, a variation in pore size will be noticeable. Table 4.8 shows that variation again with the example of the 20 mm radius scaffold. In the case of the constant radius strategy, because all the curved fibers in Table 4.7 are parallel, there is no difference between the front and back of the scaffold, and so there isn't that distinction in Table 4.8.

Table 4.7 – Pore size variation in the top layer of the 20 mm radius scaffolds created with the concentric and constant radius strategies.

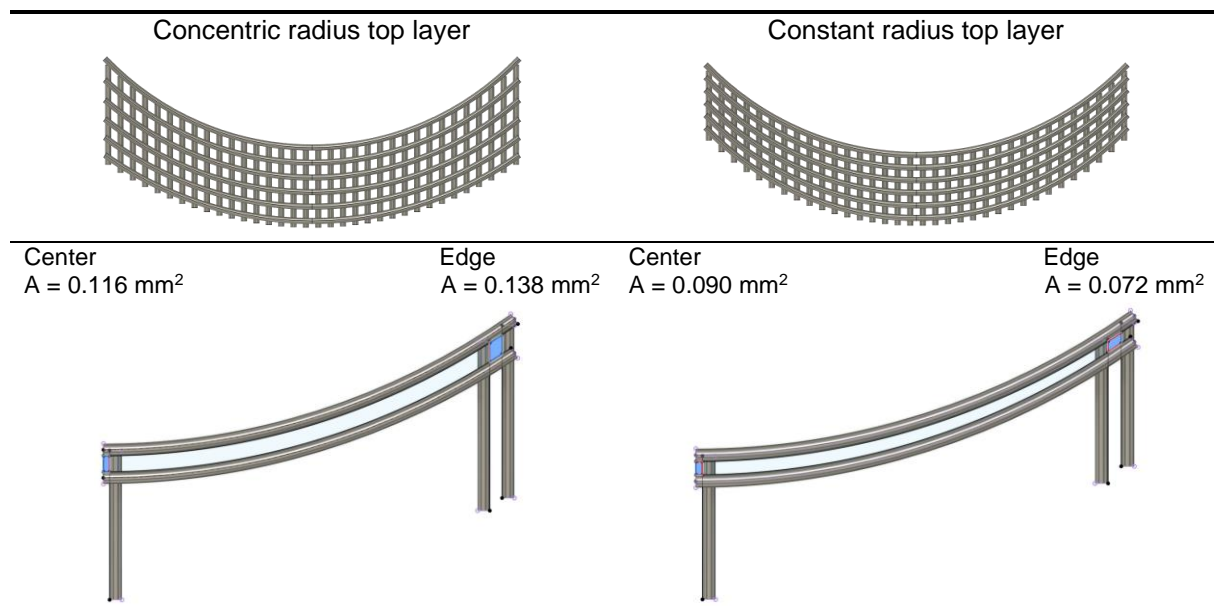


Table 4.8 – Projected pore area at the center and edge of top and middle layers of the 20 mm radius scaffolds created with the concentric and constant radius strategies.

Projected pore area / mm <sup>2</sup>		Concentric		Constant	
		Center	Edge	Center	Edge
Top layer	Front	0.11	0.125	0.09	0.072
	Back	0.116	0.138		
Middle layer	Front	0.09	0.099	0.09	0.077
	Back	0.09	0.102		

### 4.3.3. Manufacturing of curved scaffolds

Scaffolds from Figure 4.33 and Figure 4.34 were manufactured by FDM so that the predictions about their printability could be verified and also so that other analysis that require physical models could be performed. The material chosen for the scaffolds was PLA and the profile described in section 3.4.1 used. In annex A.2 pictures of the top and bottom surfaces of the scaffolds designed with both concentric and constant radius strategies are shown.

From pictures in annex A.2, a preliminary analysis can be made about the quality of manufactured scaffolds. For scaffolds with surface radius of 20 mm and superior, for both concentric and constant radius strategies, the prints showed good overall quality, however with some pore occlusions being detected (Figure 4.35a). These most likely result from occasional residual pressure at the end of the nozzle, which cause oozing of the filament. Due to multiple printhead movements between scaffold fibers, oozing occurrences were more likely to happen and on some occasions pores became occluded. The fact that PrusaSlicer does not allow total control over the printhead movement, which could not be fully optimized for the scaffolds being printed, with the printhead occasionally moving from side to side



of the scaffold, also favors this occlusion. In relation to stringing, very little was detected. Considering the individual scaffold fibers, none were detached from the print and the scaffolds seemed to have good integrity.

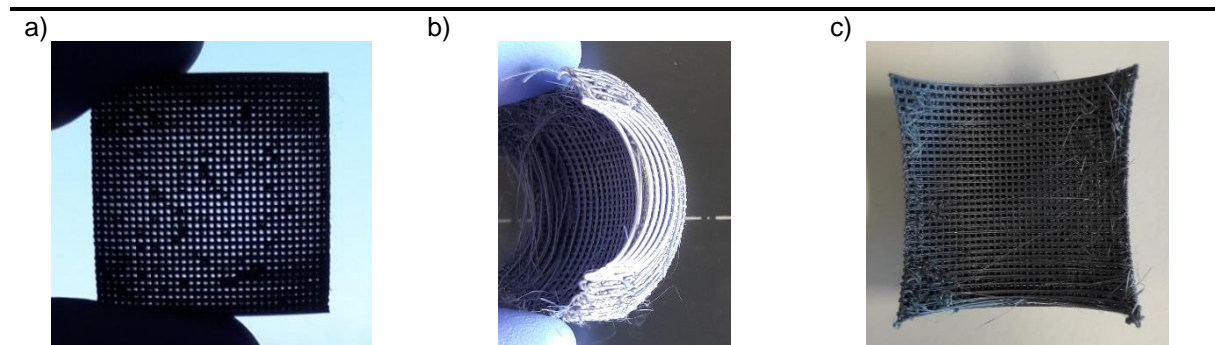


Figure 4.35 – Representative pictures of imperfections in the curved scaffolds manufactured by FDM: a) pore occlusions seen in all curved scaffolds; b) detached fibers seen in scaffolds with radius of 14 mm and 12 mm; c) stringing, more noticeable in scaffolds of radius 17.064 mm and smaller.

For the scaffolds with surface radius of 17.064 mm and inferior, the anticipated problems were detected. In the scaffolds with 14 mm and 12 mm radius, some fibers printed on the first and on the last layers were totally detached from the remainder of the printed object or hanging by some loose threads but without structural integrity and could be separated by a slight pulling (Figure 4.35b). In some places those fibers were even deformed, due to the fact of being printed without support. In the scaffolds with 17.064 mm radius, no fibers were detached, however some had a very small contact with the rest of the scaffold and could therefore be easily separated, which is in line with the assumptions made when calculating this extreme plausible curvature. In these scaffolds it was visible more stringing (Figure 4.35c), and an apparent relatively similar pore occlusion (which was not possible to quantify only with visual means). Concerning the stringing and the occlusion defects, a first approach to reduce them would be fine tuning the printing profile.

Beyond this preliminary visual analysis, a comprehensive laboratory examination should be done, namely with micro-CT imaging and by mechanical characterization. Concerning the mechanical behavior, it would be an important analysis to undertake. Since in these curved scaffolds the adhesion between some fibers is reduced there could be a reduction in the mechanical resistance, which would be important to quantify.

#### 4.3.4. Scaffolds micro-CT characterization

Micro-CT reconstructions of the curved scaffolds are shown in Figure 4.36 and Figure 4.37. At the current stage of the work, the reconstructions were done with three radii for each of the two scaffold construction strategies. Selected radii were the limit 17.064 mm, one higher, and one smaller. As discussed previously, it can again be seen that some fibers at the edge of the scaffolds are detached, and more noticeably in the scaffolds with a smaller radius. In the scaffolds with 14 mm radius, edge fibers are seen completely detached and distorted, in the scaffolds with 17.064 mm the extremities of fibers are seen detached, and in the scaffolds with 20 mm, although the fibers were printed respecting the curvature of the design, the contact points of the edge fibers do not seem the most robust.

With the data from the micro-CT reconstructions, shape fidelity could be determined in relation to the printed scaffolds, to determine the accuracy of the printing. One convenient measure that could be obtained from micro-CT and the scaffold CAD model is the porosity over a control volume. Time and equipment constraints hindered the collection of this data within the timeframe for this thesis, but it should be attainable in the near future.

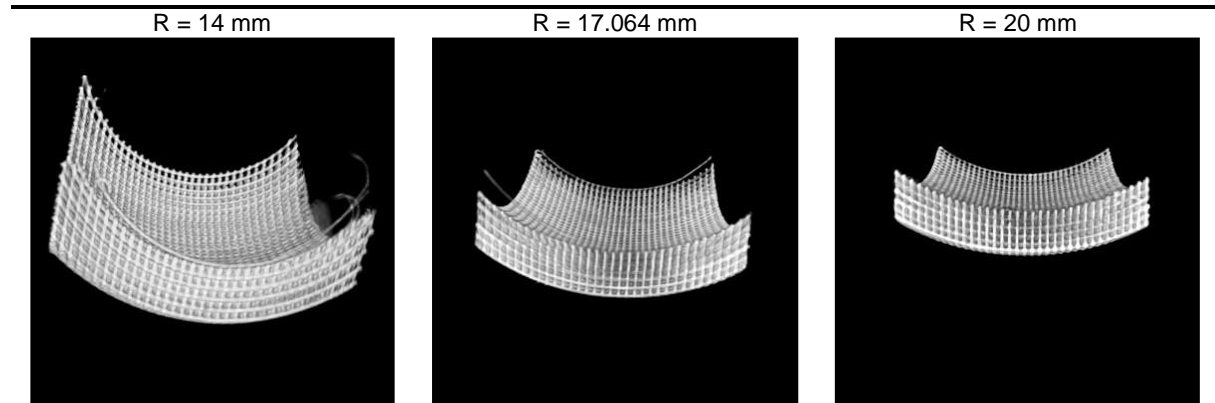


Figure 4.36 – Curved scaffolds micro-CT imaging reconstructions. Scaffolds designed with concentric radius strategy.

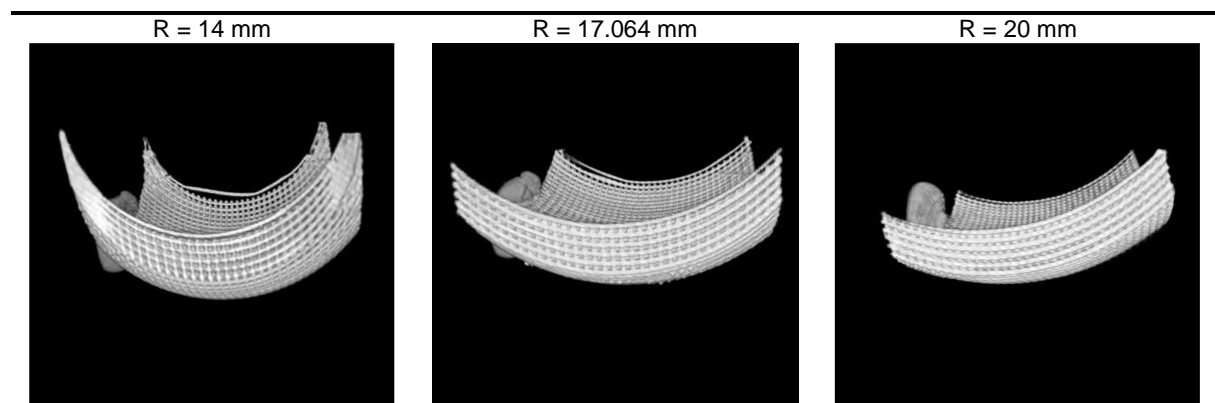


Figure 4.37 – Curved scaffolds micro-CT imaging reconstructions. Scaffolds designed with constant radius strategy.

#### 4.3.5. Computational simulation of the compressive mechanical behavior of the scaffolds

For the simulation of the compressive mechanical behavior, one scaffold was selected to demonstrate the calculations results. The chosen was the scaffold with 20 mm radius and concentric curved surfaces, because it should be a scaffold that would have a good fidelity in relation to its FDM print. The scaffolds with 17.064 mm radius are at the limit of printability, with some fibers detaching, so the next most curved scaffold was chosen. The concentric strategy was chosen because with this strategy, when creating the G-code files for the smaller radius scaffolds, all pores remain open, which does not happen with the constant radius strategy.

Due to the complexity of the curved scaffold model, generating a file too big for COMSOL to handle, the simulation could not be done using the entire model. The alternative was to select relevant regions of interest in the scaffold, run the simulation on those regions, and then extrapolate the results for the

entire scaffold. Figure 4.38 shows the selected regions of interest. Their size is close to the largest COMSOL could use so that it would return a result in a reasonable time. The square regions were chosen to compare the opposing situations that would be verified at the center and at the corner of the scaffold, and the slice was chosen to analyze the behavior from the center to the edge. Using symmetry, the obtained results could be generalized for the rest of the scaffold.

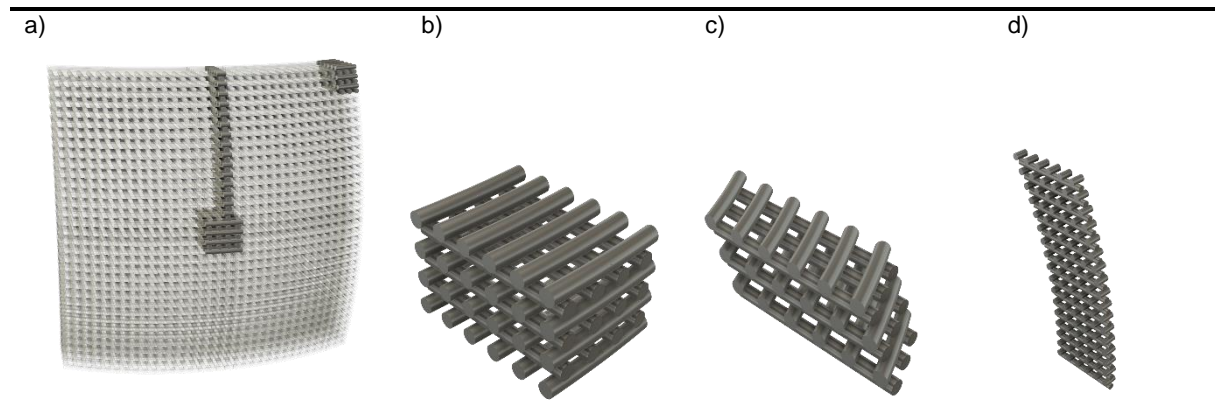


Figure 4.38 – Regions of interest for finite element analysis of the mechanical behavior in an illustrative curved scaffold: a) Concentric, 20 mm radius scaffold (light) and regions of interest (dark); b) Section through the center; c) Section on the corner; d) Slice next to the vertical axis of symmetry.

Figure 4.39a, b, and c show respectively the von Mises stress for the center, the corner, and the slice of the scaffold, that allows to determine if the material will yield under the applied load. It can be seen that the greater stresses are predicted for the fiber connections in the front of the scaffold, where the load is applied, and that this value is significantly higher in relation to the stresses in every other region of the scaffold. Besides these extremes, it is also in the other fiber connections that the stress is higher, but with values within the same magnitude as the maximum in the rest of the scaffolds. It can also be observed that the fibers that run from the front to the back of the scaffold show an evenly distributed stress except in the front, where the load is applied. In the fibers parallel to the load, except the ones in the front row, the stress is considerably lower, meaning that very little load is transferred to those fibers.

Due to the fact that only sections of the scaffold were modeled, some observations need a more careful analysis. In Figure 4.39a, the two fibers at the top and bottom of the section, show extraordinarily high stresses because the fibers that exist above and below them in the complete scaffold were not considered in the model. The load they are subjected to would be transferred in two directions instead of only one. So, the maximum stress value calculated in this simulation is not totally realistic. It must be understood that the actual scaffold goes beyond this section in four directions. A comparable situation is seen in Figure 4.39b. Since only a small section from the corner was modeled, the simulation predicts that it bends upwards with the applied load. However, from Figure 4.39c it can be anticipated this bending would not be seen in a complete scaffold because the fibers below would prevent it from happening. Figure 4.39c also confirms the intuition that the fibers at the edge of the scaffold will be the ones more susceptible of yielding.

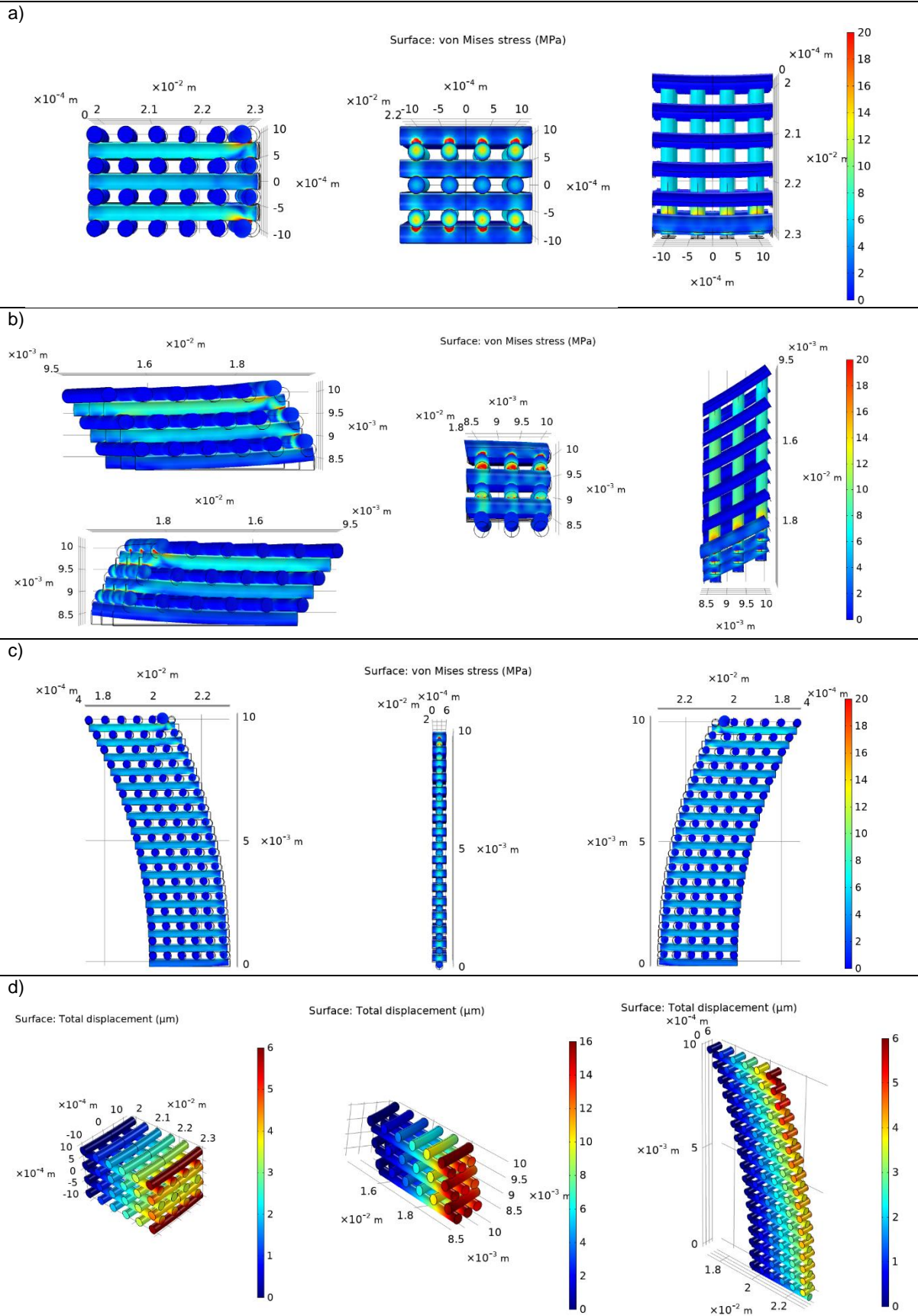


Figure 4.39 – Finite element analysis on the regions of interest from Figure 4.38, simulating the mechanical behavior to regions of interest of a PLA scaffold when 1 MPa load is applied on the front surface and the back is considered fixed: a) Side, front, and top views of the von Mises stress; b) Both sides, front, and top views of the von Mises stress; c) Side, front and opposite side views of the von Mises stress; d) Predicted displacement due to the applied load. (Scale bars truncated below the maximum to provide a better sense of the simulated behavior).

Figure 4.39a, b, and c also shows the deformation of the fibers due to the applied load. The farther the fibers are from the wireframe structure and the larger they are, the greater the deformation. Figure 4.39d quantifies this deformation calculating the displacement, in micrometers, caused by the application of the load. The reasoning used in the previous paragraph to grasp the extreme values of stress can also be applied to the displacement. The more extreme values of displacement will probably not be realistic once the whole scaffold is considered.

Scaffold mechanical behavior simulation will be particularly relevant for constructs designed for high load bearing tissues. In humans, the higher stresses are observed in the OC regions of the lower limb, with magnitudes typically in the range of 5.0-6.8 MPa in the ankle joint, and with lower but similar magnitudes in the hip and knee joints<sup>143</sup>. It has also been reported that, during walking, the average stress in the knee is within the range of 1-1.5 MPa<sup>144</sup>, and compressive tests determined the knee cartilage failure with stresses up to an average of 15.3 MPa<sup>145</sup>. It should also be considered that cartilage can be modeled as a viscoelastic or poroelastic material depending on the rate of loading, which could change determined deformations<sup>143</sup>. Some variability may be expected between studies due to different methodologies applied, but there is an agreement in the magnitude of the reported values. In the conducted simulation the applied load was 1 MPa and so loads in real conditions and in the simulation seem comparable. Still, it needs to be considered that the study conducted was stationary and that in OC tissues there will be a high variability in applied loads, and so it would also be very relevant to do a time dependent study on the behavior of the scaffold, with loads applied with a frequency similar to the observed in natural tissues.

In the literature, the reported PLA yield strength ranges from 70 to 90 MPa<sup>146,147</sup>. Considering these values, the mechanical simulation predicts that the designed scaffolds might withstand the simulated applied load, however with the question of how they would behave at the places where fibers intersect. In the future, an actual mechanical test with the manufactured scaffolds would be required to validate this hypothesis and other results of the mechanical simulation.

#### 4.3.6. Example applications of curved scaffolds

The development of the curved scaffolds in this work began as an attempt to reproduce the curvature of natural tissues, particularly the OC regions. The manufactured curved scaffolds still do not reproduce the whole surface since there are no variations in their curvature, but they showed that it was possible to manufacture curved scaffolds. Figure 4.40 shows the radius of spheres that approximate the round surfaces of OC tissue in a human femur. The dimensions of the manufactured scaffolds are similar to constructs required for those tissues and the estimated radii could all be reproduced by the FDM method used in this thesis. It would then be plausible that scaffolds could be created that would meet personalized needs to repair defects in OC tissues. The necessity for scaffolds mimicking native tissues is manifested in the literature, and more examples can be found (Figure 4.41).



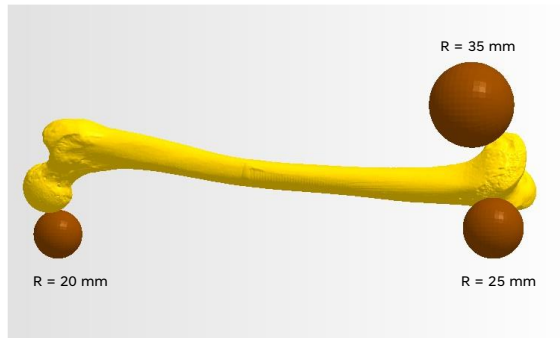


Figure 4.40 – Radius of spheres approximating the curvatures of osteochondral surfaces in a human femur.

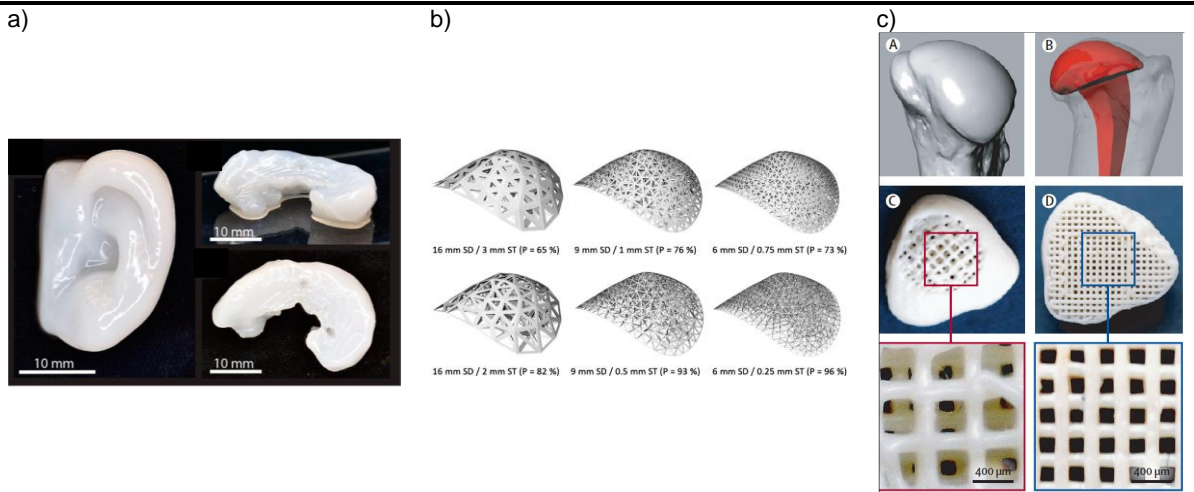


Figure 4.41 – Examples of patient-tailored curved structures produced by additive manufacturing: a) 3D bioprints of human ear and sheep meniscus; b) FDM prints of a breast; c) FDM print of rabbit proximal humeral joint (adapted from <sup>136,148,149</sup>).

## 5. Conclusions and future work

In this work the development of scaffolds for OC TE focused on two aspects: the first concerned the study and characterization of different strategies, based on the conductive polymer PEDOT:PSS, to coat PCL scaffolds and improve its electroconductive surface properties; the second concerned the establishment of fast scaffold design processes, the conceptualization and development of curved scaffolds for personalized TE approaches, and the use of FDM technology to manufacture these scaffolds.

ES is known to guide the development and regeneration of many tissues. To allow the study of its effect in cell proliferation and differentiation envisaging OC TE applications, six different coating conditions were evaluated to functionalize non-electrically conductive PCL scaffolds. The coating strategies combining the cross-linkers GOPS or DVS with the PEDOT:PSS dispersion proved to be superior, maintaining structural integrity and providing adequate, stable and long-lasting electrical conductivity, which the strategy without the cross-linkers could not demonstrate. The surface modification of PCL, attained with an alkaline treatment, increasing hydroxyl and carboxyl groups at its surface, did not seem to influence the performance of the coating strategies, with properties very similar to those of coatings done to pristine PCL. Comparing the two cross-linker coating strategies (GOPS and DVS), no particularly significant differences were identified between them. On the contrary, the impact of the coating and annealing procedure on the mechanical properties of the scaffolds was significant, causing a considerable and similar decrease in the compressive modulus of all PEDOT:PSS-coated scaffolds. Further characterization studies need to be carried out, namely SEM, to have a better understanding of the effect of alkaline treatment on the scaffold surface, confirming the erosion of PCL reported in other studies, and also to possibly have a more accurate determination of the coating thickness.

Beyond characterization, the next steps will involve cell culture work to assess the biological performance of the produced electroconductive scaffolds. Compatibility with the coating could first be tested with cell viability and proliferation assays followed by studies to determine the differentiation potential of the scaffolds. ES protocols could then be implemented to demonstrate their influence in the development of increasingly native-like tissue constructs.

Scaffold geometry also plays an important role determining cell behavior and influencing tissue development. To be able to test the effect of different structures, design processes were implemented to easily modify scaffold dimensions. Specifically, orthogonal scaffolds can be quickly created by specifying pore and fiber dimensions as well as the number of fibers along the three orthogonal axis. Moreover, scaffolds with varying angles between fibers in consecutive layers, and scaffolds with pore dimension varying within the same layer or in consecutive layers were also developed. Having these scaffolds available, future work will include the experimental evaluation of their performance in bone and OC TE strategies.

Of particular interest is the case of the scaffold with pore variation along the layers. The purpose of the design was to provide a geometry with one side more favorable to chondrogenic differentiation, and the other side more favorable to osteogenic differentiation, integrating them both in the same construct,

and reproducing more closely the natural relation between the two tissues. In this regard, considering future work, a further development of the two-chamber reactor would also be beneficial, allowing an individualized stimulation to each side of the scaffold.

With the aim of personalizing TE therapies, it was demonstrated the feasibility of designing scaffolds from medical imaging data and manufacturing them by FDM. Their characterization would be of interest to do in the future, and in particular the prediction of its mechanical properties using numerical modeling strategies and its experimental mechanical characterization, despite the particular challenges it presents due to their curved complex structure.

Considering the mathematically defined curved scaffolds, the micro-CT reconstructions point to the confirmation of the premises behind their modeling. With increased curvature, the contact points between fibers start become increasingly weaker and more easily detachable. The predicted limit of curvature was in line with the observations: scaffolds with the 17.064 mm radius demonstrated fidelity to the designed model, however with some detachments due to very weak adhesion between fibers; with smaller radii some fibers were printed completely detached and deformed; with larger radii, scaffolds seemed more structurally robust. These differences in adhesion, together with the novelty of this geometry, advise for their mechanical characterization in the future, which would be particularly interesting to compare with the mechanical properties of more conventional orthogonal scaffolds.

Further developments could also be considered for these curved scaffolds in the future, using more parameters to control the curvature, in order to approximate it to more natural shapes. The experimental mechanical characterization of the curved scaffold will also be relevant to validate the mathematical simulation of its behavior present in this work.

Having an accurate computational representation of the scaffold physics, in the form of a digital twin, will also provide considerable advantages in time and resources when investigating new scaffold designs. In terms of constructing a mathematical representation of the scaffold, a computational fluid dynamics (CFD) analysis would also be of great relevance. Considering the possibility of seeding cells in these scaffolds and of placing the cell-seeded constructs within bioreactors, it would be essential to avoid detrimental effects caused by high shear stresses or insufficient nutrient and waste transfer.

One final consideration should be made about the printing of all scaffolds in this work concerning the G-code files. These files were created with PrusaSlicer, a program for general 3D printing that should conform to a wide variety of objects and provide normally good quality prints. It allows control over many printing parameters which an algorithm uses to choose the path for filament deposition. However, due to its generality, in the case of scaffolds it does not allow control over the sequence with which the fibers are deposited. In some instances, the chosen path was clearly not the optimal, with the printhead moving from side to side of the scaffold instead of printing in sequence from one side to the other, which resulted in artifacts like pore occlusions and in poorer quality prints. In the future, even if the creation of a slicer software for scaffolds is excessive, a solution could be conceived in which a program could be used to rewrite the G-code, changing the path in which filament is deposited, and minimize these problems.



## References

1. Zhang, B., Huang, J. & Narayan, R. J. Gradient scaffolds for osteochondral tissue engineering and regeneration. *J. Mater. Chem. B* **8**, 8149–8170 (2020).
2. Alexander, P. G., Gottardi, R., Lin, H., Lozito, T. P. & Tuan, R. S. Three-dimensional osteogenic and chondrogenic systems to model osteochondral physiology and degenerative joint diseases. *Exp. Biol. Med.* **239**, 1080–1095 (2014).
3. Di Luca, A., Van Blitterswijk, C. & Moroni, L. The osteochondral interface as a gradient tissue: From development to the fabrication of gradient scaffolds for regenerative medicine. *Birth Defects Res. Part C - Embryo Today Rev.* **105**, 34–52 (2015).
4. Correia, C. R., Reis, R. L. & Mano, J. F. Multiphasic, Multistructured and Hierarchical Strategies for Cartilage Regeneration. in *Engineering Mineralized and Load Bearing Tissues* (eds. Bertassoni, L. E. & Coelho, P. G.) 143–160 (Springer International Publishing, 2015). doi:10.1007/978-3-319-22345-2\_9.
5. Wei, W. & Dai, H. Articular cartilage and osteochondral tissue engineering techniques: Recent advances and challenges. *Bioact. Mater.* **6**, 4830–4855 (2021).
6. Lowe, J. & Anderson, P. *Stevens & Lowe's Human Histology*. (Mosby Ltd., 2014).
7. Carballo, C. B., Nakagawa, Y., Sekiya, I. & Rodeo, S. A. Basic Science of Articular Cartilage. *Clin. Sports Med.* **36**, 413–425 (2017).
8. Baumann, C. A., Hinckel, B. B., Bozynski, C. C. & Farr, J. Articular Cartilage: Structure and Restoration. in *Joint Preservation of the Knee* 3–24 (Springer International Publishing, 2019). doi:10.1007/978-3-030-01491-9\_1.
9. Bhosale, A. M. & Richardson, J. B. Articular cartilage: Structure, injuries and review of management. *Br. Med. Bull.* **87**, 77–95 (2008).
10. Temenoff, J. S. & Mikos, A. G. Review: tissue engineering for regeneration of articular cartilage. *Biomaterials* **21**, 431–440 (2000).
11. Chen, F. H., Rousche, K. T. & Tuan, R. S. Technology Insight: adult stem cells in cartilage regeneration and tissue engineering. *Nat. Clin. Pract. Rheumatol.* **2**, 373–382 (2006).
12. Gupta, R. C., Lall, R., Srivastava, A. & Sinha, A. Hyaluronic Acid: Molecular Mechanisms and Therapeutic Trajectory. *Front. Vet. Sci.* **6**, 1–24 (2019).
13. Deng, C., Chang, J. & Wu, C. Bioactive scaffolds for osteochondral regeneration. *J. Orthop. Transl.* **17**, 15–25 (2019).
14. Cheng, H., Luk, K. D. K., Cheung, K. M. C. & Chan, B. P. In vitro generation of an osteochondral interface from mesenchymal stem cell–collagen microspheres. *Biomaterials* **32**, 1526–1535 (2011).
15. Karsdal, M. A. Introduction. in *Biochemistry of Collagens, Laminins and Elastin* xix–xxxiv (Elsevier, 2016). doi:10.1016/B978-0-12-809847-9.02001-8.
16. Madry, H., van Dijk, C. N. & Mueller-Gerbl, M. The basic science of the subchondral bone. *Knee Surgery, Sport. Traumatol. Arthrosc.* **18**, 419–433 (2010).
17. Salgado, A. J., Coutinho, O. P. & Reis, R. L. Bone tissue engineering: State of the art and future

- trends. *Macromol. Biosci.* **4**, 743–765 (2004).
18. Lopa, S. & Madry, H. Bioinspired Scaffolds for Osteochondral Regeneration. *Tissue Eng. Part A* **20**, 2052–2076 (2014).
  19. Killen, M.-C. & Charalambous, C. P. Advances in cartilage restoration techniques. in *Advances in Medical and Surgical Engineering* (eds. Ahmed, W., Phoenix, D. A., Jackson, M. J. & Charalambous, C. P.) 71–83 (Academic Press, 2020). doi:10.1016/B978-0-12-819712-7.00006-1.
  20. Jacob, G., Shimomura, K. & Nakamura, N. Osteochondral Injury, Management and Tissue Engineering Approaches. *Front. Cell Dev. Biol.* **8**, (2020).
  21. Nukavarapu, S. P. & Dorcemus, D. L. Osteochondral tissue engineering: Current strategies and challenges. *Biotechnol. Adv.* **31**, 706–721 (2013).
  22. Huang, B. J., Hu, J. C. & Athanasiou, K. A. Cell-based tissue engineering strategies used in the clinical repair of articular cartilage. *Biomaterials* **98**, 1–22 (2016).
  23. Kwon, H. *et al.* Surgical and tissue engineering strategies for articular cartilage and meniscus repair. *Nat. Rev. Rheumatol.* **15**, 550–570 (2019).
  24. Sun, A. X. *et al.* Chondrogenesis of human bone marrow mesenchymal stem cells in 3-dimensional, photocrosslinked hydrogel constructs: Effect of cell seeding density and material stiffness. *Acta Biomater.* **58**, 302–311 (2017).
  25. Fu, L. *et al.* Advances and prospects in biomimetic multilayered scaffolds for articular cartilage regeneration. *Regen. Biomater.* **7**, 527–542 (2020).
  26. Vinatier, C., Mrugala, D., Jorgensen, C., Guicheux, J. & Noël, D. Cartilage engineering: a crucial combination of cells, biomaterials and biofactors. *Trends Biotechnol.* **27**, 307–314 (2009).
  27. Makris, E. A., Gomoll, A. H., Malizos, K. N., Hu, J. C. & Athanasiou, K. A. Repair and tissue engineering techniques for articular cartilage. *Nat. Rev. Rheumatol.* **11**, 21–34 (2015).
  28. Turnbull, G. *et al.* 3D bioactive composite scaffolds for bone tissue engineering. *Bioact. Mater.* **3**, 278–314 (2018).
  29. Iulian, A., Dan, L., Camelia, T., Claudia, M. & Sebastian, G. Synthetic Materials for Osteochondral Tissue Engineering. in *Osteochondral Tissue Engineering: Nanotechnology, Scaffolding-Related Developments and Translation* (eds. Oliveira, J. M., Pina, S., Reis, R. L. & San Roman, J.) 31–52 (Springer International Publishing, 2018). doi:10.1007/978-3-319-76711-6\_2.
  30. Armiento, A. R., Stoddart, M. J., Alini, M. & Eglin, D. Biomaterials for articular cartilage tissue engineering: Learning from biology. *Acta Biomater.* **65**, 1–20 (2018).
  31. Yang, J., Zhang, Y. S., Yue, K. & Khademhosseini, A. Cell-laden hydrogels for osteochondral and cartilage tissue engineering. *Acta Biomater.* **57**, 1–25 (2017).
  32. Koons, G. L., Diba, M. & Mikos, A. G. Materials design for bone-tissue engineering. *Nat. Rev. Mater.* **5**, 584–603 (2020).
  33. Morouço, P., Fernandes, C. & Lattanzi, W. Challenges and innovations in osteochondral regeneration: Insights from biology and inputs from bioengineering toward the optimization of tissue engineering strategies. *J. Funct. Biomater.* **12**, (2021).

34. Cheng, A. *et al.* Advances in Porous Scaffold Design for Bone and Cartilage Tissue Engineering and Regeneration. *Tissue Eng. - Part B Rev.* **25**, 14–29 (2019).
35. Roseti, L. *et al.* Scaffolds for Bone Tissue Engineering: State of the art and new perspectives. *Mater. Sci. Eng. C* **78**, 1246–1262 (2017).
36. Puppi, D., Chiellini, F., Piras, A. M. & Chiellini, E. Polymeric materials for bone and cartilage repair. *Prog. Polym. Sci.* **35**, 403–440 (2010).
37. Bartnikowski, M., Dargaville, T. R., Ivanovski, S. & Hutmacher, D. W. Degradation mechanisms of polycaprolactone in the context of chemistry, geometry and environment. *Prog. Polym. Sci.* **96**, 1–20 (2019).
38. Longley, R., Ferreira, A. M. & Gentile, P. Recent approaches to the manufacturing of biomimetic multi-phasic scaffolds for osteochondral regeneration. *Int. J. Mol. Sci.* **19**, (2018).
39. Pereira, D. R., Reis, R. L. & Oliveira, J. M. Layered Scaffolds for Osteochondral Tissue Engineering. *Adv. Exp. Med. Biol.* **1058**, 193–218 (2018).
40. Yousefi, A. M., Hoque, M. E., Prasad, R. G. S. V. & Uth, N. Current strategies in multiphasic scaffold design for osteochondral tissue engineering: A review. *J. Biomed. Mater. Res. - Part A* **103**, 2460–2481 (2015).
41. Liu, Z., Meyers, M. A., Zhang, Z. & Ritchie, R. O. Functional gradients and heterogeneities in biological materials: Design principles, functions, and bioinspired applications. *Prog. Mater. Sci.* **88**, 467–498 (2017).
42. Hutmacher, D. W., Woodfield, T. B. F. & Dalton, P. D. Scaffold Design and Fabrication. in *Tissue Engineering* 311–346 (Elsevier, 2014). doi:10.1016/B978-0-12-420145-3.00010-9.
43. Loh, Q. L. & Choong, C. Three-dimensional scaffolds for tissue engineering applications: Role of porosity and pore size. *Tissue Eng. - Part B Rev.* **19**, 485–502 (2013).
44. Sundelacruz, S. & Kaplan, D. L. Stem cell- and scaffold-based tissue engineering approaches to osteochondral regenerative medicine. *Semin. Cell Dev. Biol.* **20**, 646–655 (2009).
45. Ondrésik, M., Oliveira, J. M. & Reis, R. L. Advances for Treatment of Knee OC Defects. in *Osteochondral Tissue Engineering: Challenges, Current Strategies, and Technological Advances* (eds. Oliveira, J. M., Pina, S., Reis, R. L. & San Roman, J.) 3–24 (Springer International Publishing, 2018). doi:10.1007/978-3-319-76735-2\_1.
46. Canadas, R. F., Pirraco, R. P., Oliveira, J. M., Reis, R. L. & Marques, A. P. Stem Cells for Osteochondral Regeneration. in *Osteochondral Tissue Engineering: Challenges, Current Strategies, and Technological Advances* (eds. Oliveira, J. M., Pina, S., Reis, R. L. & San Roman, J.) 219–240 (Springer International Publishing, 2018). doi:10.1007/978-3-319-76735-2\_10.
47. Gadjanski, I. Mimetic Hierarchical Approaches for Osteochondral Tissue Engineering. in *Osteochondral Tissue Engineering: Nanotechnology, Scaffolding-Related Developments and Translation* (eds. Oliveira, J. M., Pina, S., Reis, R. L. & San Roman, J.) 143–170 (Springer International Publishing, 2018). doi:10.1007/978-3-319-76711-6\_7.
48. Grimaud, E., Heymann, D. & Rédini, F. Recent advances in TGF- $\beta$  effects on chondrocyte metabolism. *Cytokine Growth Factor Rev.* **13**, 241–257 (2002).
49. Deng, Z. H., Li, Y. S., Gao, X., Lei, G. H. & Huard, J. Bone morphogenetic proteins for articular

- cartilage regeneration. *Osteoarthr. Cartil.* **26**, 1153–1161 (2018).
50. Fortier, L. A., Barker, J. U., Strauss, E. J., McCarrel, T. M. & Cole, B. J. The Role of Growth Factors in Cartilage Repair. *Clin. Orthop. Relat. Res.* **469**, 2706–2715 (2011).
  51. Uebersax, L., Merkle, H. P. & Meinel, L. Insulin-like growth factor I releasing silk fibroin scaffolds induce chondrogenic differentiation of human mesenchymal stem cells. *J. Control. Release* **127**, 12–21 (2008).
  52. Ornitz, D. M. & Marie, P. J. Fibroblast growth factor signaling in skeletal development and disease. *Genes Dev.* **29**, 1463–1486 (2015).
  53. Beenken, A. & Mohammadi, M. The FGF family: Biology, pathophysiology and therapy. *Nat. Rev. Drug Discov.* **8**, 235–253 (2009).
  54. Gadjanski, I., Spiller, K. & Vunjak-Novakovic, G. Time-Dependent Processes in Stem Cell-Based Tissue Engineering of Articular Cartilage. *Stem Cell Rev. Reports* **8**, 863–881 (2012).
  55. Schipani, E. *et al.* Hypoxia in cartilage: HIF-1 $\alpha$  is essential for chondrocyte growth arrest and survival. *Genes Dev.* **15**, 2865–2876 (2001).
  56. Henrotin, Y., Kurz, B. & Aigner, T. Oxygen and reactive oxygen species in cartilage degradation: friends or foes? *Osteoarthr. Cartil.* **13**, 643–654 (2005).
  57. Saghati, S. *et al.* Tissue Engineering Strategies to Increase Osteochondral Regeneration of Stem Cells; a Close Look at Different Modalities. *Stem Cell Rev. Reports* **17**, 1294–1311 (2021).
  58. Li, K., Zhang, C., Qiu, L., Gao, L. & Zhang, X. Advances in Application of Mechanical Stimuli in Bioreactors for Cartilage Tissue Engineering. *Tissue Eng. Part B Rev.* **23**, 399–411 (2017).
  59. Davis, S., Roldo, M., Blunn, G., Tozzi, G. & Roncada, T. Influence of the Mechanical Environment on the Regeneration of Osteochondral Defects. *Front. Bioeng. Biotechnol.* **9**, 1–23 (2021).
  60. Thriyakraman, G., Boda, S. K. & Basu, B. Unraveling the mechanistic effects of electric field stimulation towards directing stem cell fate and function: A tissue engineering perspective. *Biomaterials* **150**, 60–86 (2018).
  61. Levin, M. Molecular bioelectricity: How endogenous voltage potentials control cell behavior and instruct pattern regulation in vivo. *Mol. Biol. Cell* **25**, 3835–3850 (2014).
  62. Hronik-Tupaj, M. & Kaplan, D. L. A review of the responses of two-and three-dimensional engineered tissues to electric fields. *Tissue Eng. - Part B Rev.* **18**, 167–180 (2012).
  63. Balint, R., Cassidy, N. J. & Cartmell, S. H. Electrical stimulation: A novel tool for tissue engineering. *Tissue Eng. - Part B Rev.* **19**, 48–57 (2013).
  64. Chen, C., Bai, X., Ding, Y. & Lee, I. S. Electrical stimulation as a novel tool for regulating cell behavior in tissue engineering. *Biomater. Res.* **23**, 1–12 (2019).
  65. Leppik, L., Oliveira, K. M. C., Bhavsar, M. B. & Barker, J. H. Electrical stimulation in bone tissue engineering treatments. *Eur. J. Trauma Emerg. Surg.* **46**, 231–244 (2020).
  66. Ning, C., Zhou, Z., Tan, G., Zhu, Y. & Mao, C. Electroactive polymers for tissue regeneration: Developments and perspectives. *Prog. Polym. Sci.* **81**, 144–162 (2018).
  67. Guimard, N. K., Gomez, N. & Schmidt, C. E. Conducting polymers in biomedical engineering. *Prog. Polym. Sci.* **32**, 876–921 (2007).
  68. Guo, B. & Ma, P. X. Conducting Polymers for Tissue Engineering. *Biomacromolecules* **19**, 1764–

- 1782 (2018).
69. Piro, B. *et al.* Fabrication and use of organic electrochemical transistors for sensing of metabolites in aqueous media. *Appl. Sci.* **8**, (2018).
  70. Pires, F., Ferreira, Q., Rodrigues, C. A. V., Morgado, J. & Ferreira, F. C. Neural stem cell differentiation by electrical stimulation using a cross-linked PEDOT substrate: Expanding the use of biocompatible conjugated conductive polymers for neural tissue engineering. *Biochim. Biophys. Acta - Gen. Subj.* **1850**, 1158–1168 (2015).
  71. Håkansson, A. *et al.* Effect of (3-glycidyloxypropyl)trimethoxysilane (GOPS) on the electrical properties of PEDOT:PSS films. *J. Polym. Sci. Part B Polym. Phys.* **55**, 814–820 (2017).
  72. Mantione, D. *et al.* Low-Temperature Cross-Linking of PEDOT:PSS Films Using Divinylsulfone. *ACS Appl. Mater. Interfaces* **9**, 18254–18262 (2017).
  73. Leong, K. F., Cheah, C. M. & Chua, C. K. Solid freeform fabrication of three-dimensional scaffolds for engineering replacement tissues and organs. *Biomaterials* **24**, 2363–2378 (2003).
  74. Gillispie, G. J. *et al.* Three-Dimensional Tissue and Organ Printing in Regenerative Medicine. in *Principles of Regenerative Medicine* 831–852 (Elsevier, 2019). doi:10.1016/B978-0-12-809880-6.00047-3.
  75. Eltom, A., Zhong, G. & Muhammad, A. Scaffold Techniques and Designs in Tissue Engineering Functions and Purposes: A Review. *Adv. Mater. Sci. Eng.* **2019**, (2019).
  76. Mota, C., Puppi, D., Chiellini, F. & Chiellini, E. Additive manufacturing techniques for the production of tissue engineering constructs. *J. Tissue Eng. Regen. Med.* **9**, 174–190 (2015).
  77. Do, A. V., Khorsand, B., Geary, S. M. & Salem, A. K. 3D Printing of Scaffolds for Tissue Regeneration Applications. *Adv. Healthc. Mater.* **4**, 1742–1762 (2015).
  78. Bahraminasab, M. Challenges on optimization of 3D-printed bone scaffolds. *Biomed. Eng. Online* **19**, 1–33 (2020).
  79. Gay, S. *et al.* PLA scaffolds production from Thermally Induced Phase Separation: Effect of process parameters and development of an environmentally improved route assisted by supercritical carbon dioxide. *J. Supercrit. Fluids* **136**, 123–135 (2018).
  80. Gonçalves, A. M., Moreira, A., Weber, A., Williams, G. R. & Costa, P. F. Osteochondral tissue engineering: The potential of electrospinning and additive manufacturing. *Pharmaceutics* **13**, (2021).
  81. Wubneh, A., Tsekoura, E. K., Ayranci, C. & Uludağ, H. Current state of fabrication technologies and materials for bone tissue engineering. *Acta Biomater.* **80**, 1–30 (2018).
  82. De Mori, A., Fernández, M. P., Blunn, G., Tozzi, G. & Roldo, M. 3D printing and electrospinning of composite hydrogels for cartilage and bone tissue engineering. *Polymers (Basel)*. **10**, 1–26 (2018).
  83. Thavornnyutikarn, B., Chantarapanich, N., Sitthiseripratip, K., Thouas, G. A. & Chen, Q. Bone tissue engineering scaffolding: computer-aided scaffolding techniques. *Prog. Biomater.* **3**, 61–102 (2014).
  84. Melchels, F. P. W. *et al.* Additive manufacturing of tissues and organs. *Prog. Polym. Sci.* **37**, 1079–1104 (2012).

85. Jeong, C. G. & Atala, A. 3D Printing and Biofabrication for Load Bearing Tissue Engineering. in *Engineering Mineralized and Load Bearing Tissues* (eds. Bertassoni, L. E. & Coelho, P. G.) 3–14 (Springer International Publishing, 2015). doi:10.1007/978-3-319-22345-2\_1.
86. Moreno Madrid, A. P., Vrech, S. M., Sanchez, M. A. & Rodriguez, A. P. Advances in additive manufacturing for bone tissue engineering scaffolds. *Mater. Sci. Eng. C* **100**, 631–644 (2019).
87. Matai, I., Kaur, G., Seyedsalehi, A., McClinton, A. & Laurencin, C. T. Progress in 3D bioprinting technology for tissue/organ regenerative engineering. *Biomaterials* **226**, 119536 (2020).
88. Chung, J. J., Im, H., Kim, S. H., Park, J. W. & Jung, Y. Toward Biomimetic Scaffolds for Tissue Engineering: 3D Printing Techniques in Regenerative Medicine. *Front. Bioeng. Biotechnol.* **8**, 1–12 (2020).
89. Huang, Y., Zhang, X. F., Gao, G., Yonezawa, T. & Cui, X. 3D bioprinting and the current applications in tissue engineering. *Biotechnol. J.* **12**, (2017).
90. Mora-Boza, A. & Lopez-Donaire, M. L. Preparation of Polymeric and Composite Scaffolds by 3D Bioprinting. in *Osteochondral Tissue Engineering: Nanotechnology, Scaffolding-Related Developments and Translation* (eds. Oliveira, J. M., Pina, S., Reis, R. L. & San Roman, J.) 221–245 (Springer International Publishing, 2018). doi:10.1007/978-3-319-76711-6\_10.
91. Pedde, R. D. *et al.* Emerging Biofabrication Strategies for Engineering Complex Tissue Constructs. *Adv. Mater.* **29**, 1–27 (2017).
92. Melchels, F. P. W., Feijen, J. & Grijpma, D. W. A review on stereolithography and its applications in biomedical engineering. *Biomaterials* **31**, 6121–6130 (2010).
93. Skoog, S. A., Goering, P. L. & Narayan, R. J. Stereolithography in tissue engineering. *J. Mater. Sci. Mater. Med.* **25**, 845–856 (2014).
94. Kumar, H. & Kim, K. Stereolithography 3D Bioprinting. in *3D Bioprinting: Principles and Protocols* (ed. Crook, J. M.) 93–108 (Springer US, 2020). doi:10.1007/978-1-0716-0520-2\_6.
95. Chia, H. N. & Wu, B. M. Recent advances in 3D printing of biomaterials. *J. Biol. Eng.* **9**, 1–14 (2015).
96. Shirazi, S. F. S. *et al.* A review on powder-based additive manufacturing for tissue engineering: selective laser sintering and inkjet 3D printing. *Sci. Technol. Adv. Mater.* **16**, 033502 (2015).
97. Su, X., Wang, T. & Guo, S. Applications of 3D printed bone tissue engineering scaffolds in the stem cell field. *Regen. Ther.* **16**, 63–72 (2021).
98. Zhang, L., Yang, G., Johnson, B. N. & Jia, X. Three-dimensional (3D) printed scaffold and material selection for bone repair. *Acta Biomater.* **84**, 16–33 (2019).
99. Ngo, T. D., Kashani, A., Imbalzano, G., Nguyen, K. T. Q. & Hui, D. Additive manufacturing (3D printing): A review of materials, methods, applications and challenges. *Compos. Part B Eng.* **143**, 172–196 (2018).
100. No Title. <https://www.prusa3d.com/>.
101. No Title. <https://e3d-online.com/pages/toolchanger>.
102. Jammalamadaka, U. & Tappa, K. Recent advances in biomaterials for 3D printing and tissue engineering. *J. Funct. Biomater.* **9**, (2018).
103. Gleadall, A., Visscher, D., Yang, J., Thomas, D. & Segal, J. Review of additive manufactured

- tissue engineering scaffolds: relationship between geometry and performance. *Burn. Trauma* **6**, 1–16 (2018).
104. Kang, H.-W. *et al.* A 3D bioprinting system to produce human-scale tissue constructs with structural integrity. *Nat. Biotechnol.* **34**, 312–319 (2016).
  105. Jung, J. W., Lee, J.-S. & Cho, D.-W. Computer-aided multiple-head 3D printing system for printing of heterogeneous organ/tissue constructs. *Sci. Rep.* **6**, 21685 (2016).
  106. Bartnikowski, M., Klein, T. J., Melchels, F. P. W. & Woodruff, M. A. Effects of scaffold architecture on mechanical characteristics and osteoblast response to static and perfusion bioreactor cultures. *Biotechnol. Bioeng.* **111**, 1440–1451 (2014).
  107. Schwab, A. *et al.* Printability and Shape Fidelity of Bioinks in 3D Bioprinting. *Chem. Rev.* **120**, 11028–11055 (2020).
  108. Groll, J. *et al.* A definition of bioinks and their distinction from biomaterial inks. *Biofabrication* **11**, 013001 (2018).
  109. Mandrycky, C., Wang, Z., Kim, K. & Kim, D. H. 3D bioprinting for engineering complex tissues. *Biotechnol. Adv.* **34**, 422–434 (2016).
  110. Thayer, P., Martinez, H. & Gatenholm, E. History and Trends of 3D Bioprinting. in *3D Bioprinting: Principles and Protocols* (ed. Crook, J. M.) 3–18 (Springer US, 2020). doi:10.1007/978-1-0716-0520-2\_1.
  111. Hakobyan, D. *et al.* Laser-Assisted Bioprinting for Bone Repair. in *3D Bioprinting: Principles and Protocols* (ed. Crook, J. M.) 135–144 (Springer US, 2020). doi:10.1007/978-1-0716-0520-2\_8.
  112. Koch, L., Deiwick, A. & Chichkov, B. Laser-Based Cell Printing. in *3D Printing and Biofabrication* 303–329 (Springer International Publishing, 2018). doi:10.1007/978-3-319-45444-3\_11.
  113. Murphy, S. V. & Atala, A. 3D bioprinting of tissues and organs. *Nat. Biotechnol.* **32**, 773–785 (2014).
  114. Möller, J. & Pörtner, R. Digital Twins for Tissue Culture Techniques—Concepts, Expectations, and State of the Art. *Processes* **9**, 447 (2021).
  115. Geris, L., Lambrechts, T., Carlier, A. & Papantoniou, I. The future is digital: In silico tissue engineering. *Curr. Opin. Biomed. Eng.* **6**, 92–98 (2018).
  116. Meneses, J. *et al.* A multimodal stimulation cell culture bioreactor for tissue engineering: A numerical modelling approach. *Polymers (Basel)*. **12**, (2020).
  117. Xue, R. *et al.* Osteochondral tissue coculture: An in vitro and in silico approach. *Biotechnol. Bioeng.* **116**, 3112–3123 (2019).
  118. Fiedler, T. *et al.* On the mechanical properties of PLC-bioactive glass scaffolds fabricated via BioExtrusion. *Mater. Sci. Eng. C* **57**, 288–293 (2015).
  119. Moura, C. S. *et al.* Chondrogenic differentiation of mesenchymal stem/stromal cells on 3D porous poly ( $\epsilon$ -caprolactone) scaffolds: Effects of material alkaline treatment and chondroitin sulfate supplementation. *J. Biosci. Bioeng.* **129**, 756–764 (2020).
  120. Silva, J. C., Moura, C. S., Alves, N., Cabral, J. M. S. & Ferreira, F. C. Effects of different fibre alignments and bioactive coatings on mesenchymal stem/stromal cell adhesion, proliferation and chondrogenesis in poly ( $\epsilon$ -caprolactone) scaffolds. (2016).

121. Silva, J. C. *et al.* Effects of glycosaminoglycan supplementation in the chondrogenic differentiation of bone marrow- and synovial- derived mesenchymal stem/stromal cells on 3D-extruded poly ( $\epsilon$ -caprolactone) scaffolds. *Int. J. Polym. Mater. Polym. Biomater.* **70**, 207–222 (2021).
122. Sarkar, S. Roles of Nanofiber Scaffold Structure and Chemistry in Directing Human Bone Marrow Stromal Cell Response. *Adv. Tissue Eng. Regen. Med. Open Access* **1**, (2016).
123. Sordini, L. *et al.* Effect of Electrical Stimulation Conditions on Neural Stem Cells Differentiation on Cross-Linked PEDOT:PSS Films. *Front. Bioeng. Biotechnol.* **9**, (2021).
124. Çabuk, H., Yılmaz, Y. & Yıldız, E. Vortex-Assisted Deep Eutectic Solvent-Based Liquid-Liquid Microextraction for the Analysis of Alkyl Gallates in Vegetable Oils. *Acta Chim. Slov.* **66**, 385–394 (2019).
125. Haoue, S., Derdar, H., Belbachir, M. & Harrane, A. Polymerization of Ethylene Glycol Dimethacrylate (EGDM), Using An Algerian Clay as Eco-catalyst (Maghnite-H<sup>+</sup> and Maghnite-Na<sup>+</sup>). *Bull. Chem. React. Eng. Catal.* **15**, 221–230 (2020).
126. Zhao, Q., Jamal, R., Zhang, L., Wang, M. & Abdiryim, T. The structure and properties of PEDOT synthesized by template-free solution method. *Nanoscale Res. Lett.* **9**, 557 (2014).
127. Phillipson, K., Hay, J. N. & Jenkins, M. J. Thermal analysis FTIR spectroscopy of poly( $\epsilon$ -caprolactone). *Thermochim. Acta* **595**, 74–82 (2014).
128. Lam, C. X. F., Savalani, M. M., Teoh, S.-H. & Hutmacher, D. W. Dynamics of in vitro polymer degradation of polycaprolactone-based scaffolds: accelerated versus simulated physiological conditions. *Biomed. Mater.* **3**, 034108 (2008).
129. Eshraghi, S. & Das, S. Mechanical and microstructural properties of polycaprolactone scaffolds with one-dimensional, two-dimensional, and three-dimensional orthogonally oriented porous architectures produced by selective laser sintering. *Acta Biomater.* **6**, 2467–2476 (2010).
130. Moura, C. S., Silva, C. L. da, Bártolo, P. J. & Ferreira, F. C. Combination of 3D Extruded-based Poly ( $\epsilon$ -caprolactone) Scaffolds with Mesenchymal Stem/Stromal Cells: Strategy Optimization. *Procedia Eng.* **110**, 122–127 (2015).
131. Gupte, M. J. *et al.* Pore size directs bone marrow stromal cell fate and tissue regeneration in nanofibrous macroporous scaffolds by mediating vascularization. *Acta Biomater.* **82**, 1–11 (2018).
132. Murphy, C. M., Haugh, M. G. & O'Brien, F. J. The effect of mean pore size on cell attachment, proliferation and migration in collagen–glycosaminoglycan scaffolds for bone tissue engineering. *Biomaterials* **31**, 461–466 (2010).
133. Zhang, Q., Lu, H., Kawazoe, N. & Chen, G. Pore size effect of collagen scaffolds on cartilage regeneration. *Acta Biomater.* **10**, 2005–2013 (2014).
134. Silva, J. C. *et al.* Extruded Bioreactor Perfusion Culture Supports the Chondrogenic Differentiation of Human Mesenchymal Stem/Stromal Cells in 3D Porous Poly( $\epsilon$ -Caprolactone) Scaffolds. *Biotechnol. J.* **15**, 1–14 (2020).
135. Mota, C., Camarero-Espinosa, S., Baker, M. B., Wieringa, P. & Moroni, L. Bioprinting: From Tissue and Organ Development to in Vitro Models. *Chem. Rev.* **120**, 10547–10607 (2020).



136. Melchels, F. *et al.* CAD/CAM-assisted breast reconstruction. *Biofabrication* **3**, 034114 (2011).
137. Daly, A. C. *et al.* 3D Bioprinting for Cartilage and Osteochondral Tissue Engineering. *Adv. Healthc. Mater.* **6**, 1–20 (2017).
138. Gong, L. *et al.* An interleukin-4-loaded bi-layer 3D printed scaffold promotes osteochondral regeneration. *Acta Biomater.* **117**, 246–260 (2020).
139. Seyednejad, H. *et al.* In vivo biocompatibility and biodegradation of 3D-printed porous scaffolds based on a hydroxyl-functionalized poly( $\epsilon$ -caprolactone). *Biomaterials* **33**, 4309–4318 (2012).
140. Prasopthum, A., Cooper, M., Shakesheff, K. M. & Yang, J. Three-Dimensional Printed Scaffolds with Controlled Micro-/Nanoporous Surface Topography Direct Chondrogenic and Osteogenic Differentiation of Mesenchymal Stem Cells. *ACS Appl. Mater. Interfaces* **11**, 18896–18906 (2019).
141. Song, Y. *et al.* Nano-biphasic calcium phosphate/polyvinyl alcohol composites with enhanced bioactivity for bone repair via low-temperature three-dimensional printing and loading with platelet-rich fibrin. *Int. J. Nanomedicine* **13**, 505–523 (2018).
142. Moura, C. *et al.* Adhesion, proliferation and distribution of human mesenchymal stem/stromal cells (MSCs) in Poly( $\epsilon$ -caprolactone)-caprolactone (PCL) scaffolds with different pore sizes. in *High Value Manufacturing: Advanced Research in Virtual and Rapid Prototyping* 195–198 (CRC Press, 2013). doi:10.1201/b15961-36.
143. Shepherd, D. & Seedhom, B. The 'instantaneous' compressive modulus of human articular cartilage in joints of the lower limb. *Rheumatology* **38**, 124–132 (1999).
144. Barker, M. K. & Seedhom, B. B. The relationship of the compressive modulus of articular cartilage with its deformation response to cyclic loading: does cartilage optimize its modulus so as to minimize the strains arising in it due to the prevalent loading regime? *Rheumatology* **40**, 274–284 (2001).
145. Obeid, E., Adams, M. & Newman, J. Mechanical properties of articular cartilage in knees with unicompartmental osteoarthritis. *J. Bone Joint Surg. Br.* **76-B**, 315–319 (1994).
146. Farah, S., Anderson, D. G. & Langer, R. Physical and mechanical properties of PLA, and their functions in widespread applications — A comprehensive review. *Adv. Drug Deliv. Rev.* **107**, 367–392 (2016).
147. Song, Y. *et al.* Measurements of the mechanical response of unidirectional 3D-printed PLA. *Mater. Des.* **123**, 154–164 (2017).
148. Markstedt, K. *et al.* 3D Bioprinting Human Chondrocytes with Nanocellulose–Alginate Bioink for Cartilage Tissue Engineering Applications. *Biomacromolecules* **16**, 1489–1496 (2015).
149. Lee, C. H. *et al.* Regeneration of the articular surface of the rabbit synovial joint by cell homing: a proof of concept study. *Lancet* **376**, 440–448 (2010).

# Annexes

## A.1. Stability assay ATR-FTIR spectra

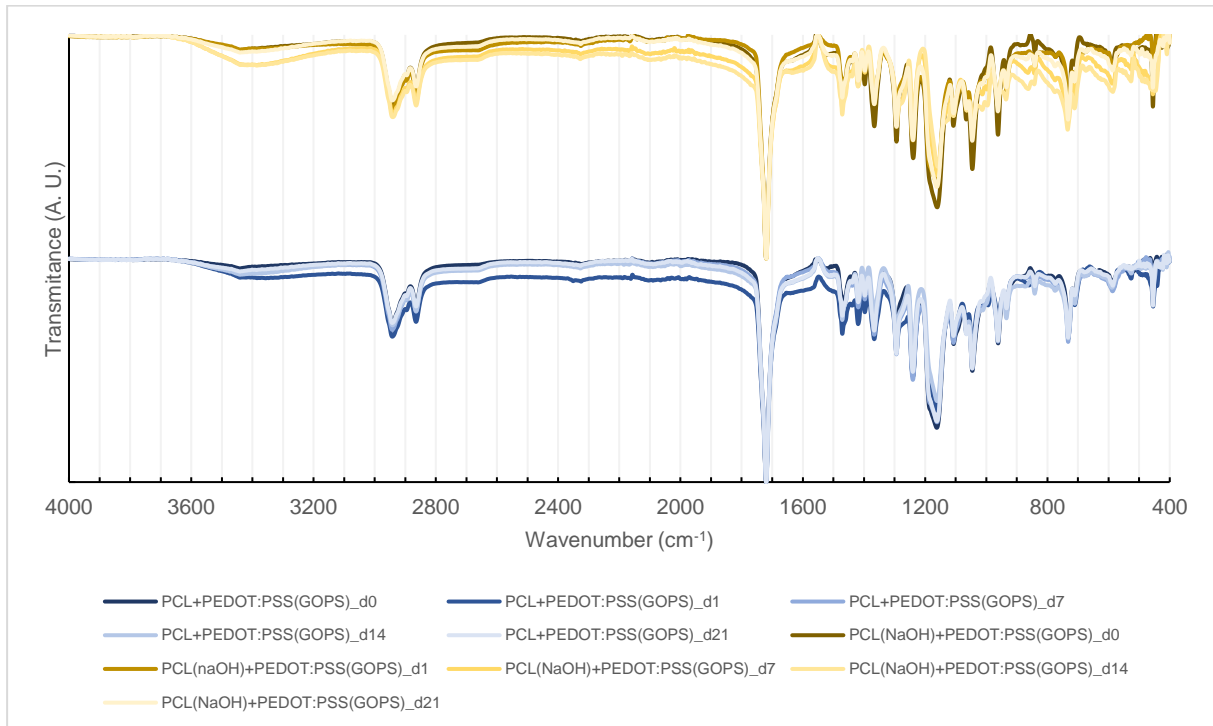


Figure A.1 – ATR-FTIR spectra of samples of PCL and PCL(NaOH) films coated with PEDOT:PSS(GOPS) collected to be analyzed on days 0, 1, 7, 14, and 21 of the stability assay.

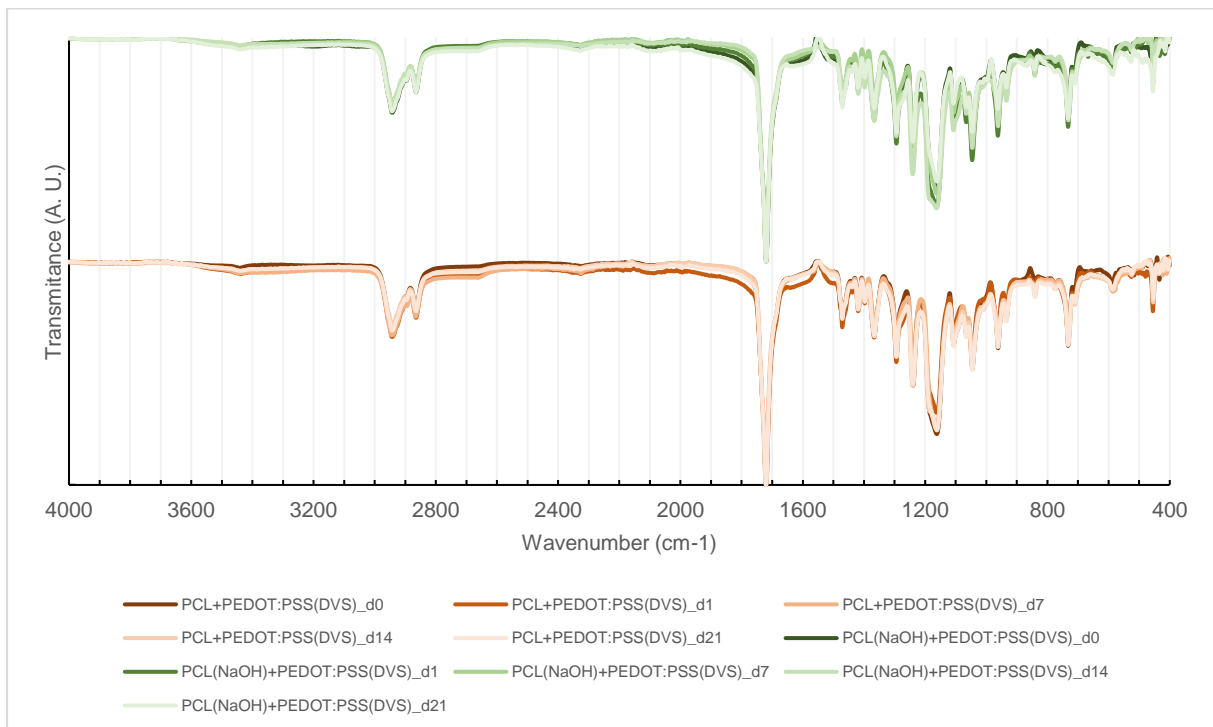


Figure A.2 – ATR-FTIR spectra of samples of PCL and PCL(NaOH) films coated with PEDOT:PSS(DVS) collected to be analyzed on days 0, 1, 7, 14, and 21 of the stability assay.

A.2. Pictures of the manufactured curved scaffolds

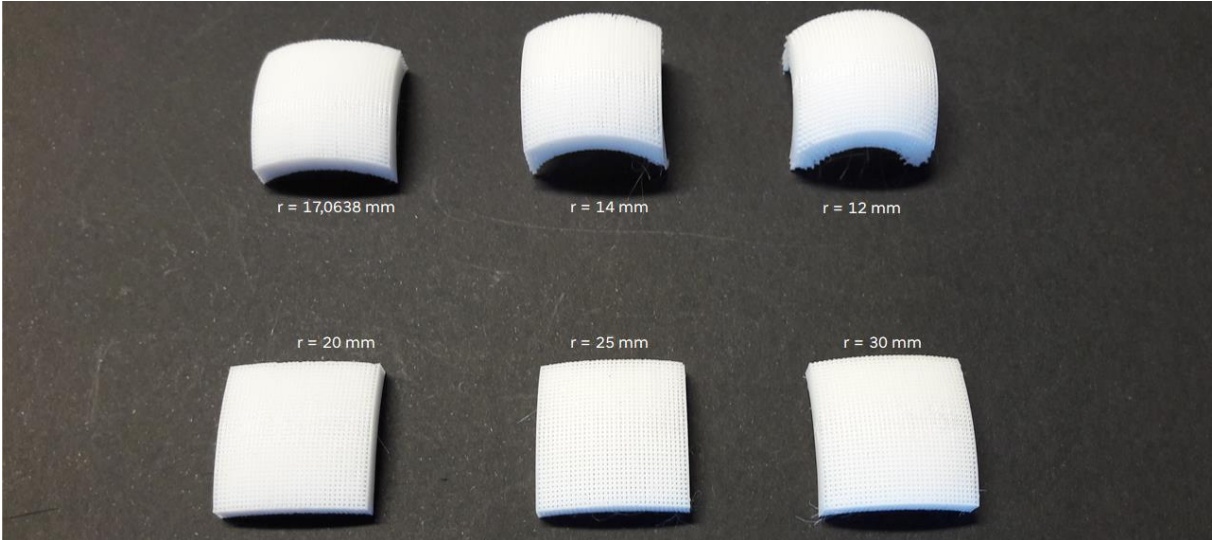


Figure A.3 – Top of FDM manufactured curved scaffolds with concentric radius surfaces.

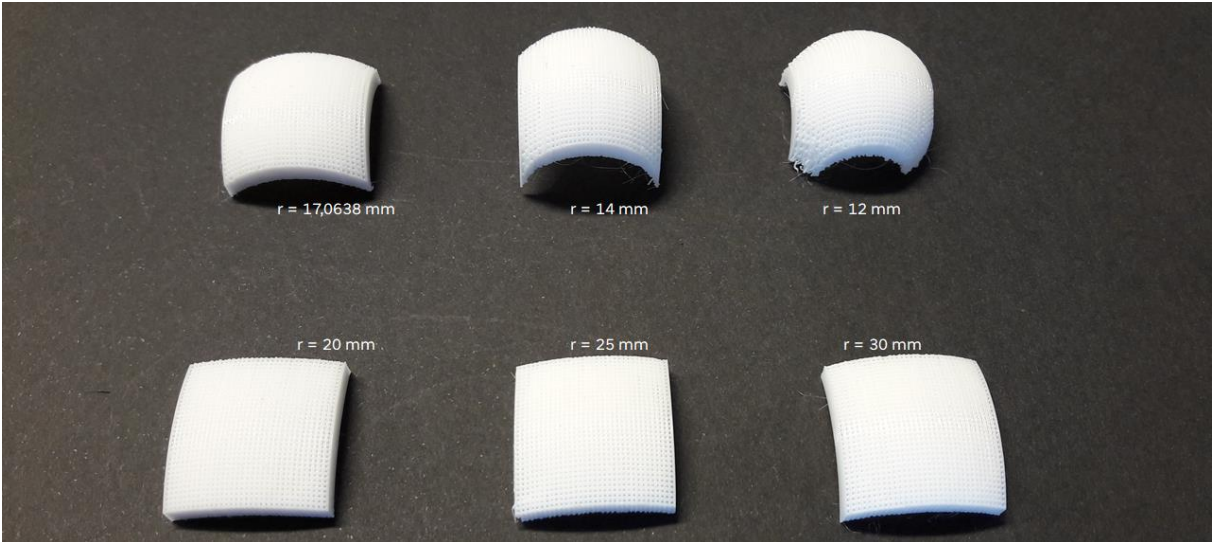


Figure A.4 – Top of FDM manufactured curved scaffolds with constant radius surfaces.

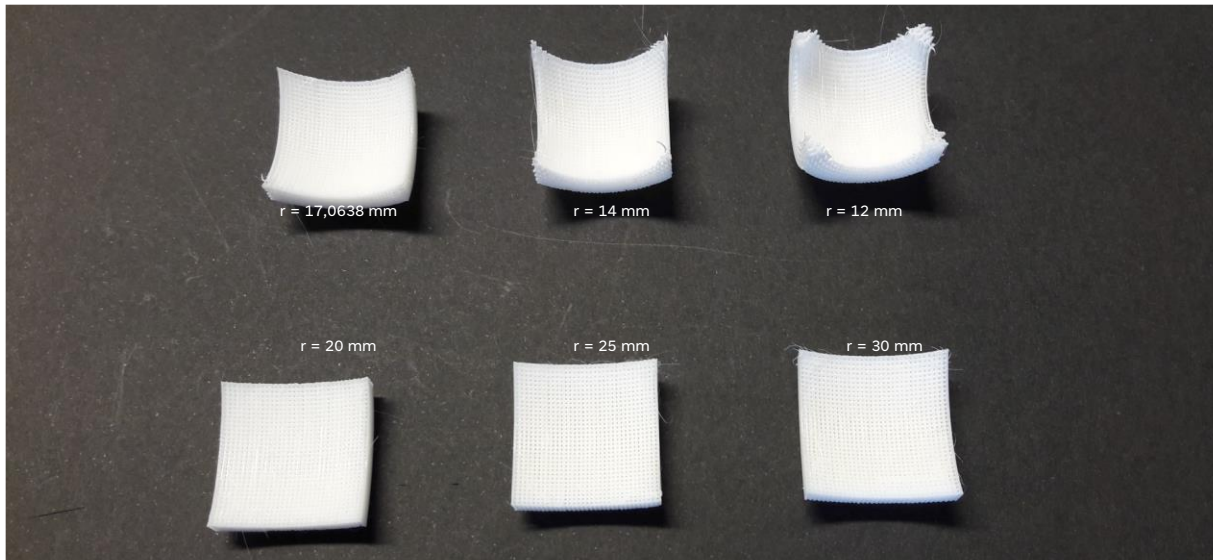


Figure A.5 – Bottom of FDM manufactured curved scaffolds with concentric radius surfaces.

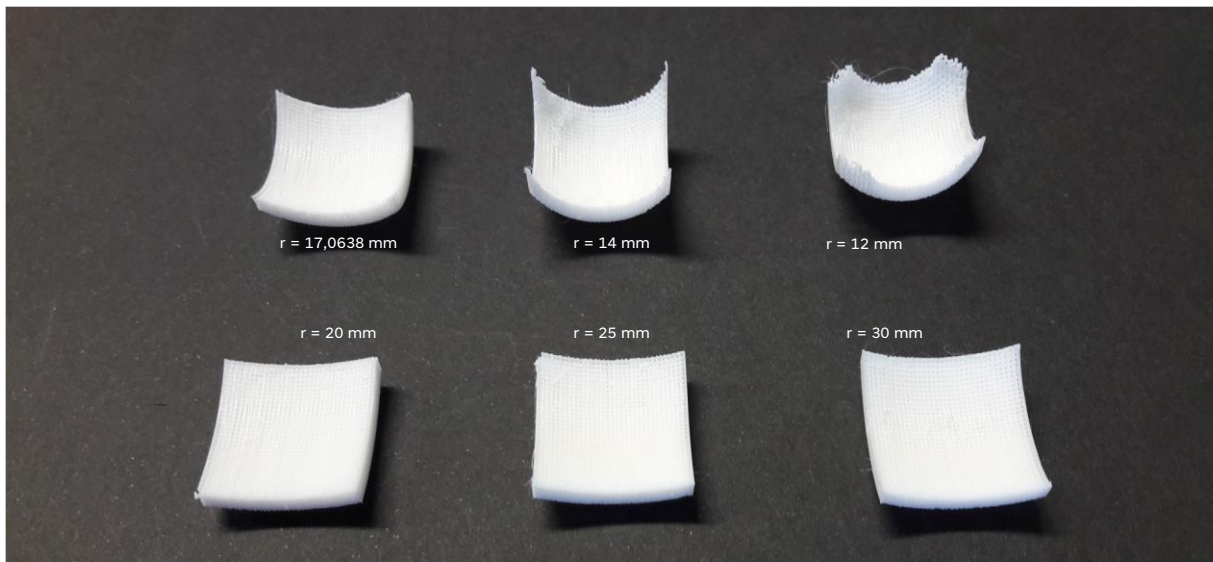


Figure A.6 – Bottom of FDM manufactured curved scaffolds with constant radius surfaces.

### A.3. Pore variation script for Fusion 360

```
import adsk.core, adsk.fusion, adsk.cam, traceback, math

#Dimensions in this script are in centimeters

#Author functions-----
def seq_pore_dim (edgePore, centrePore, nPores):
    "Returns a list with a sequence of pore dimensions in one axis"
    poreDimList = []
    variation = (edgePore - centrePore) / (nPores//2)
    currentPore = edgePore
    for i in range(nPores//2 + 1):
        poreDimList.append(currentPore)
        currentPore -= variation
    return poreDimList

def tube_centres (tubewidth, edgePore, centrePore, nPores):
    "Returns a list with the position of the center of scaffold fibers in one axis"
    tubeCentresList = []
    poreDims = seq_pore_dim(edgePore, centrePore, nPores)
    poreDims.reverse()
    position = -(tubewidth/2 + poreDims[0]/2)
    for i in range(len(poreDims)):
        position += tubewidth + poreDims[i]
        tubeCentresList.append(position)
    negtubeCentresList = [-x for x in tubeCentresList]
    negtubeCentresList.reverse()
    tubeCentresList = negtubeCentresList + tubeCentresList
    return tubeCentresList

#-----

#Definition of scaffold dimensions-----
#Only edit values in lines marked with #edit this line
#x_nPores and y_nPores must be odd numbers
tubewidth = 0.3/10

x_edgePore = 0.150/10; x_centrePore = 0.600/10; x_nPores = 15 #edit this line
x_tubes = tube_centres (tubewidth, x_edgePore, x_centrePore, x_nPores)

y_edgePore = 0.150/10; y_centrePore = 0.600/10; y_nPores = 15 #edit this line
y_tubes = tube_centres (tubewidth, y_edgePore, y_centrePore, y_nPores)

x_dim = ((x_nPores*(x_edgePore+x_centrePore)/2)+(x_edgePore-
(x_edgePore+x_centrePore)/2)+(x_nPores+1)*tubewidth)
y_dim = ((y_nPores*(y_edgePore+y_centrePore)/2)+(y_edgePore-
(y_edgePore+y_centrePore)/2)+(y_nPores+1)*tubewidth)

layerHeight = 0.3/10 #edit this line
#-----

#Fusion 360 code to draw the two first layers of the scaffold-----
def run(context):
    ui = None
    try:
        app = adsk.core.Application.get()
        ui = app.userInterface

        #doc = app.documents.add(adsk.core.DocumentTypes.FusionDesignDocumentType)
        design = app.activeProduct

        # Get the root component of the active design.
        rootComp = design.rootComponent

        # Create a new sketch on the xy plane.
```

```

sketches = rootComp.sketches;
xyPlane = rootComp.xYConstructionPlane
sketch = sketches.add(xyPlane)

# Get construction planes
planes = rootComp.constructionPlanes

# Create construction plane input
planeInput = planes.createInput()

# Add construction plane by offset
offsetValue = adsk.core.ValueInput.createByReal(layerHeight)
planeInput.setByOffset(xyPlane, offsetValue)
planeOne = planes.add(planeInput)

# Draw the first layer of connected lines.
lines = sketch.sketchCurves.sketchLines;

yy = y_dim/2 - tubeWidth/2
line2 = lines.addByTwoPoints(adsk.core.Point3D.create(x_tubes[0], -yy, 0),
adsk.core.Point3D.create(x_tubes[0], yy, 0))

    for i in range(1, len(x_tubes)):
        line1 = lines.addByTwoPoints(line2.endSketchPoint,
adsk.core.Point3D.create(x_tubes[i],yy,0))
        yy = -yy
        line2 = lines.addByTwoPoints(line1.endSketchPoint,
adsk.core.Point3D.create(x_tubes[i],yy,0))

# Draw the second layer of connected lines.
sketch2 = sketches.add(planeOne)

lines = sketch2.sketchCurves.sketchLines;

xx = x_dim/2 - tubeWidth/2
line2 = lines.addByTwoPoints(adsk.core.Point3D.create(-xx, y_tubes[0], 0),
adsk.core.Point3D.create(xx, y_tubes[0], 0))

    for i in range(1, len(y_tubes)):
        line1 = lines.addByTwoPoints(line2.endSketchPoint,
adsk.core.Point3D.create(xx,y_tubes[i],0))
        xx = -xx
        line2 = lines.addByTwoPoints(line1.endSketchPoint,
adsk.core.Point3D.create(xx,y_tubes[i],0))

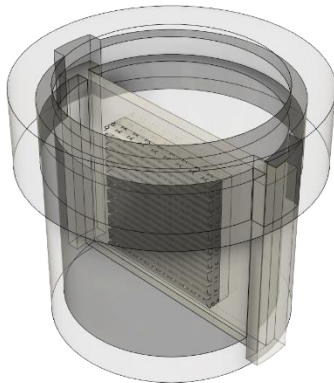
except:
    if ui:
        ui.messageBox('Failed:\n{}'.format(traceback.format_exc()))

```



#### A.4. Double chamber design

a)



b)

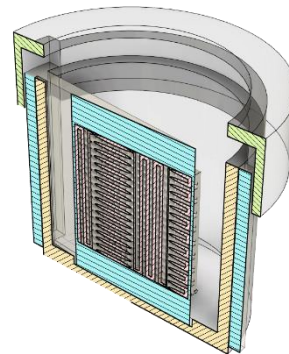
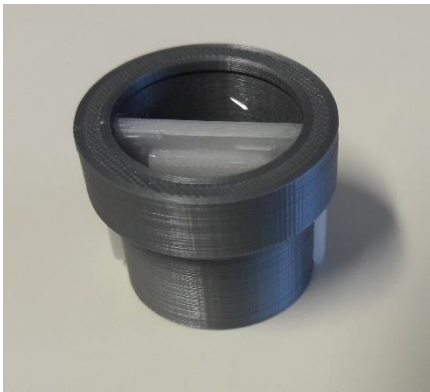


Figure A.7 – Two chamber vessel for promotion of chondrogenic and osteogenic differentiation on the opposing sides of a scaffold: a) See-through view; b) Slanted cross-section.

a)



b)

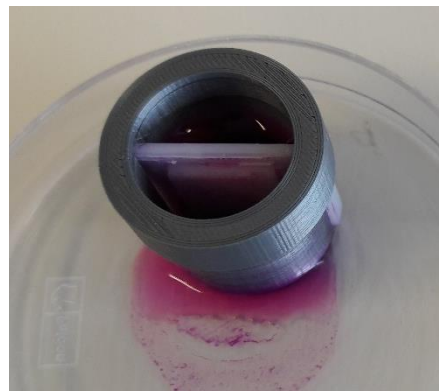
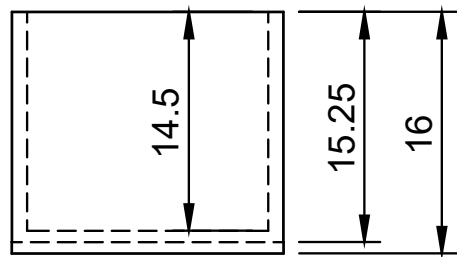
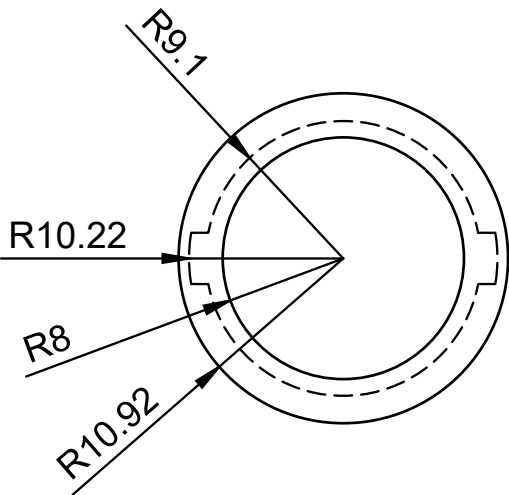
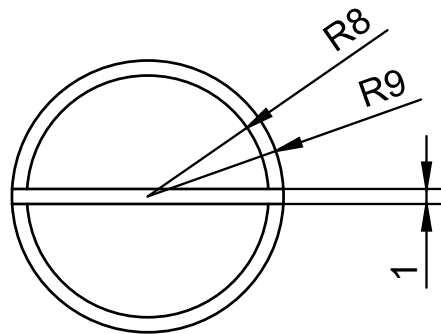
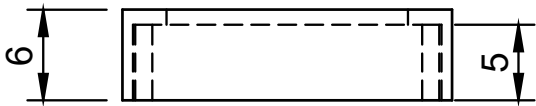
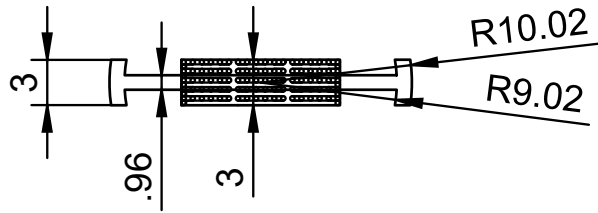
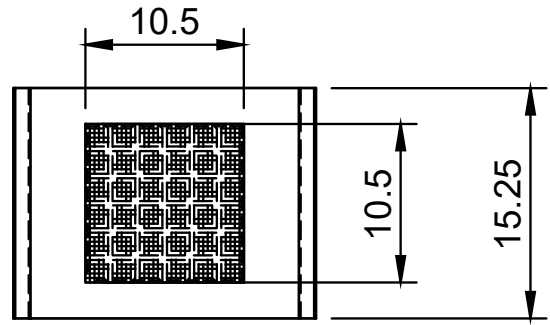
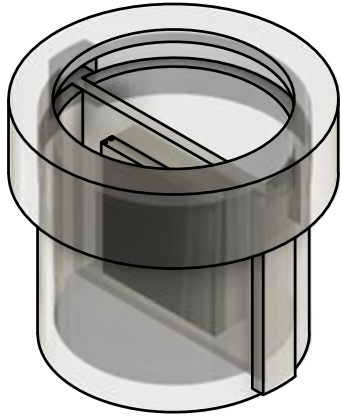


Figure A.8 – Evaluation of performance of the two chamber vessel: a) With water in only one chamber at room temperature, no leaks were observed until all water evaporated; b) With DMEM in only one chamber in an incubator at 37°, the fluid leaked and started permeating through the printed material layers.

Technical drawing





Dept.	Technical reference	Created by <b>Pedro Marcelino</b>	Approved by		
		Document type	Document status		
		Title <b>Double chamber</b>	DWG No.		
		Rev.	Date of issue	Sheet <b>1/1</b>	